A Numerical Study of Energy Balances and Flow Planforms in Earth's Mantle with Radioactive Heating, the 660 km-depth Phase Boundary and Continents

A Thesis Submitted to the
College of Graduate Studies and Research
in Partial Fulfillment of the Requirements
for the degree of Doctor of Philosophy
in the Department of Geological Sciences
University of Saskatchewan
Saskatoon

By
Gunjan Sinha

Permission to Use

In presenting this thesis in partial fulfilment of the requirements for a Postgraduate degree from the University of Saskatchewan, I agree that the Libraries of this University may make it freely available for inspection. I further agree that permission for copying of this thesis in any manner, in whole or in part, for scholarly purposes may be granted by the professor or professors who supervised my thesis work or, in their absence, by the Head of the Department or the Dean of the College in which my thesis work was done. It is understood that any copying or publication or use of this thesis or parts thereof for financial gain shall not be allowed without my written permission. It is also understood that due recognition shall be given to me and to the University of Saskatchewan in any scholarly use which may be made of any material in my thesis.

Requests for permission to copy or to make other use of material in this thesis in whole or part should be addressed to:

Head of the Department of Geological Sciences
114 Science Place
University of Saskatchewan
Saskatoon, Saskatchewan
Canada
S7N 5E2

Abstract

It is well established that the temperature gradients in the interiors of internally-heated mantle convection models are subadiabatic (e.g. Parmentier et al., 1994; Bunge et al., 1997, 2001). The subadiabatic gradients have been explained to arise due to a balance between vertical advection and internal heating, however, a detailed analysis of the energy balance in the subadiabatic regions has not been undertaken. In this research, I examine in detail the energy balance in a suite of two-dimensional convection calculations with mixed internal and basal heating, depth-dependent viscosity and continents. I find that there are three causes of subadiabatic gradients. One is the above-mentioned balance, which becomes significant when the ratio of internal heating to surface heat flux is large. The second mechanism involves the growth of the overshoot (maximum and minimum temperatures along a geotherm) of the geotherm near the lower boundary where the dominant balance is between vertical and horizontal advection. The latter mechanism is significant even in relatively weakly internally heated calculations. For time-dependent calculations, I find that local secular cooling can be a dominant term in the energy equation and can lead to subadiabaticity. However, it does not show its signature on the shape of the time-averaged geotherm. I also compare the basal heat flux with parameterized calculations based on the temperature drop at the core-mantle boundary, calculated both with and without taking the subadiabatic gradient into account and I find a significantly improved fit with its inclusion.

I also explore a wide range of parameter space to investigate the dynamical interaction between effects due to surface boundary conditions representing continental and oceanic lithosphere and the endothermic phase boundary at 660 km-depth in two-dimensional Cartesian coordinate convection calculations. I find that phase boundary induced mantle layering is strongly affected by the wavelength of convective flows and mixed surface boundary conditions strongly increase the horizontal wavelength of convection. My study shows that for mixed cases the effects of the surface boundary conditions dominate the effects of the phase boundary. I show that the calculations with complete continental coverage have the most significantly decoupled lower and upper mantle flows and substantial thermal and mechanical layering. Unlike the free-slip case where the surface heat flux decreases substantially with increasing magnitude of the Clapeyron slope, surface heat flux is shown to be almost independent of the Clapeyron slope for mixed boundary condition cases. Although very different when not layered, models with free and mixed surfaces have very similar planforms with very large aspect ratio flows when run with large magnitudes of the Clapeyron slope. I also calculate the critical boundary layer Rayleigh number as a measure of the thermal resistance of the surface boundary layer. My results show that the thermal resistance in the oceanic and the continental regions of the mixed cases are similar to fully free and no-slip cases, respectively. I find

that, even for purely basally heated models, the mantle becomes significantly subadiabatic in the presence of partial continental coverage. This is due to the significant horizontal advection of heat that occurs with very large aspect ratio convection cells.

Acknowledgements

I would like to express my gratitude to my supervisor, Prof. Samuel Butler for his encouragement and guidance throughout my Ph.D. I would like to thank the Department of Geological Sciences at the University of Saskatchewan and the Natural Sciences and Engineering Research Council of Canada for financially supporting this study.

I would also like to thank all my colleagues and friends in the Department of Geological Sciences with whom I spent a pleasant time, especially Dr. Sean Shaw, Chad Glemser, Rogan Hennie, Sandor Süle, Mike Hartley, Nadine Pearson and Simona Costin.

My special gratitude also goes to the secretaries Brenda Britton and Jane Ritz for helping me with all the administrative paper work and also to Brian Reilkoff and Jennifer Hadley for solving the serious computer troubles that I have faced during my work.

I would like to thank the members of my committee for their participation in my thesis, Drs. Kevin Ansdell, Jim Merriam, Igor Morozov and the external examiner Dr. Julian Lowman.

I express my gratitude to my parents Dr. Sekhar Sinha and Manimala Sinha and my sister Kathakali Sinha who gave me the inspiration and the moral support to pursue my objectives.

Contents

List of Tables

List of Figures

Chapter 1

Introduction

The mantle is the 2890 km thick layer of rock below the crust of the Earth and it makes up nearly 80% of our planet's total volume. It is not quite molten, but it is less viscous (softer) than the crust, and over very large time scales (millions of years), it behaves almost like a very high viscosity fluid, with the tectonic plates "floating" on top. The mantle is heated from within due to the presence of radioactive elements and from below along the CMB (core-mantle boundary). Cooling occurs along the surface and also with time the average temperature of the interior decreases, which is known as secular cooling. In chapter 3, I discuss the difference between the secular cooling and the radiogenic heat generation effects. Fig. 1.1 shows the location of the mantle in a cross-sectional diagram of the Earth. The mantle, as shown in the figure, can be divided into two regions, upper and lower. These will be described in detail later in this section.

The idea that flow in the Earth's interior is a form of thermal convection, developed slowly. Around 1797, Count Rumford became the first person to recognize the phenomenon of thermal convection, but the term "convection" was given by Prout (1834). Subcrustal convection in the Earth was first suggested by W. Hopkins in 1839 and the use of geological observations to interpret mantle convection was undertaken for the first time by Osmond Fisher in 1881. J. Thompson, in 1882, conducted the first set of experiments on convection in a fluid heated from below and cooled from above, but the earliest quantitative experiments on the onset of convection were done by Henri Bénard (1900,1901). Arthur Holmes (1931,1933) was the first to show quantitatively that thermal convection is the primary reason for the flow in the "solid" mantle and it also drives continental drift, however, these ideas were not widely accepted at that time.

After the concept of mantle convection became accepted in late 1960's, it provided a natural explanation for the high thermal gradients near the Earth's surface, which are interpreted to be the thermal boundary layers associated with mantle convection. Within these layers conduction dominates and elsewhere in the mantle the primary mechanism of heat transport is advection. Thermal convection within the mantle is the driving mechanism for plate tectonics, which is the process ultimately responsible for producing earthquakes, mountain ranges, and volcanoes. So, it is very important to have a good understanding about mantle processes. A powerful way to achieve this goal is by modeling convection within the mantle numerically. The results that are presented

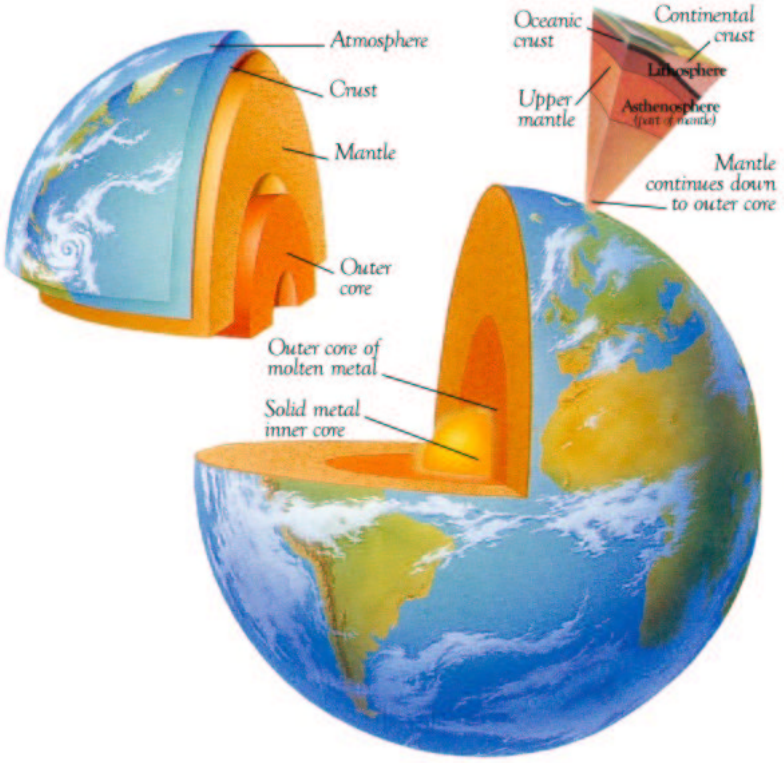

Figure 1.1: Cross-section of the Earth showing the location of the mantle from "The visual dictionary of the earth" by Colin Rose and John Temperton (Dorling Kindersley, 1994).

in this thesis are all derived from numerical modeling.

McKenzie et al. (1973) developed one of the earliest numerical models of mantle convection in a unit aspect ratio (square shaped) box. Since then, many scientists (Hewitt et al., 1980; Jarvis, 1984; Schubert and Anderson, 1985; Olson, 1987; Christensen, 1989) became involved in this field of research and built various models. Three dimensional numerical models of mantle convection in rectangular (Cserepes et al., 1988; Houseman, 1988; Travis et al., 1990a,b; Cserepes and Christensen, 1990; Christensen and Harder, 1991; Ogawa et al., 1991) and spherical geometry (Baumgardner, 1985, 1988; Machetel et al., 1986; Glatzmaier, 1988; Glatzmaier et al., 1990; Bercovici et al., 1989a, b, c, 1991, 1992; Schubert et al., 1990) began to appear in the late 1980s and provided a more realistic picture of the form of convection in the mantle. At present, three dimensional numerical models of mantle convection are widely carried out and ever-increasing computational power permits inclusion of increasingly realistic material properties and behavior into the models. However, two-dimensional models are still very common due to the high efficiency that they afford and the very good approximation of mantle processes that they provide. Some previous studies have been carried out using various 2D and 3D models and have compared their behavior. Yuen et al. (1994) studied the effect of the endothermic spinel to perovskite and magnesiowüstite phase transition induced layering in 2D and 3D Cartesian geometry calculations. This study demonstrated that greater mass flux occurs in 3D cases for smaller boxes ($5 \times 5 \times 1$), however, for wider aspect ratio models ($8 \times 8 \times 1$) the degree of mechanical layering was somewhat stronger for 3D calculations. Tackley (1993) showed that 3D spherical models with the endothermic phase transition are less time-dependent than 2D models. I carried out many calculations in two-dimensional Cartesian coordinates and these are presented in the chapters 2, 3 and 4. The heat fluxes and the the average temperatures from my calculations without continents and the endothermic phase boundary were also compared with the 3D results of Sotin and Labrosse (1999) and they were very similar.

Temperature gradients in a convecting mantle, interior to the thermal boundary layers, are usually assumed to be adiabatic. An adiabatic expansion is when a volume of material is expanded suddenly inside a perfectly sealed and insulated container, with no exchange of mass or heat beyond the walls of the container. Because pressure decreases rapidly with height and heat advection is much faster than thermal diffusion, mantle upwellings behave as if they were being expanded adiabatically. However, numerical models incorporating the effects of internal heating (e.g. Matyska and Yuen, 2000; Bunge et al., 2001) have shown the presence of positive potential temperature gradients in the mantle or in other words, subadiabatic geotherms (horizontally averaged vertical temperature profiles). A potential temperature in this case is defined as the acquired temperature of a parcel of mantle material that is brought up adiabatically to the surface. In an incompressible system (see chapter 2) the modeled mantle temperature can be considered to be an approximation for the potential temperature in a compressible system (Jarvis and McKenzie,

1980). As an example, fig. 1.2 shows the shapes of an adiabatic and a subadiabatic geotherm in models with an incompressible fluid. The solid geotherm in this case is adiabatic and has no internal heating, whereas the dashed geotherm from an internally heated model is an example of subadiabaticity shown by the positive slope interior to the boundaries. Previously Jeanloz and Morris (1987) argued that the balance between internal heating and vertical advection combined with the asymmetry between upwellings and downwellings causes subadiabatic geotherms in internally heated models. In chapter 2, I present a detailed energy balance study to investigate the reasons for subadiabatic temperature gradients from both internally and basally heated models considering an incompressible system and demonstrate that the energy balance between vertical advection and internal heating is not the only possible energy balance in regions where temperature increases with height. The presence of a subadiabatic temperature gradient results in an increased estimated CMB heat flux affecting the energy budget for the Earth and hence, can be of significant importance.

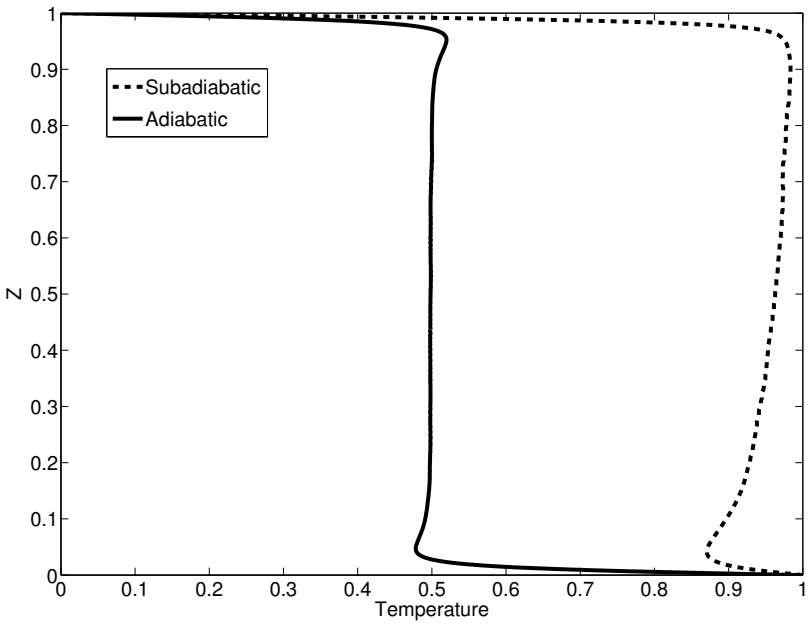

Figure 1.2: Shape of adiabatic and subadiabatic temperature gradients in a model of the mantle.

Elastic propagation of seismic waves indicates that the mantle is solid, however, the presence of plate-tectonics indicates that the underlying mantle deforms in a viscoelastic manner. This combination of rheological behavior can be compared with the ice in glaciers. Using a simple model for materials that can act as elastic solids on short timescales but fluids on long time-scale, Schubert et al. (2001) showed that the viscoelastic relaxation time for Earth's mantle is 450 yr indicating that on time-scales longer than this, the mantle behaves like a fluid. In my calculations I consider Newtonian fluid everywhere, where the stress is proportional to the strain rate, however, the mantle may be non-Newtonian in regions of high stress as in subduction zones (e.g. Hall et al., 2003, Gurnis et al., 2004, Billen and Hirth, 2005) or in areas with reduced grain size (e.g. Hirth and Kohlstedt, 2003).

The temperature in the mantle is close to its melting temperatures and hence, the crystalline solids exhibit fluid-like deformation over a long time period. Gordon (1967) proposed the two principle deformation mechanisms associated with mantle convection, viz. 1) diffusion creep, where atoms migrate by the movement of adjacent vacancies and 2) dislocation creep, which is the result of the movements due to the imperfections in the crystalline lattice. Diffusion creep results in a Newtonian flow and is strongly dependent on the grain size, however, dislocation creep is considered to follow a nonlinear viscous rheology and is insensitive to grain size changes.

The viscosity structure of the mantle is an important material property, which strongly affects the convective flow pattern, further affecting plate velocities (e.g. Gait et al., 2008; Gait and Lowman, 2007), deep-earthquake source mechanisms (e.g. Katagi et al., 2008), the stress distribution in subduction zones (e.g. Čížková et al., 2007) and estimates of geochemical mixing time-scales (e.g. Forte and Mitrovica, 2000). There are various approaches to estimate the radial viscosity structure of the Earth's mantle. The most common procedures include: 1) the inversion of post-glacial rebound data (e.g. Haskel, 1935, 1936; Daly, 1934; O'Connell, 1971; Mitrovica and Peltier, 1991a, b), 2) modeling the geoid and dynamic topography (I derive an expression for dynamic topography in appendix B) of the surface and CMB using the pattern of density anomalies inferred from seismic tomography (e.g. Forte and Peltier, 1991; Hager and Richards, 1989; Hager and Clayton, 1985; King and Masters, 1992; Ricard and Wuming, 1991; Ricard et al., 1984; Ricard et al., 1989) and 3) studying the physical deformation properties of mantle minerals in the laboratory (e.g. Ashby and Verrall, 1978; Kirby, 1983; Ranalli, 1991; Stocker and Ashby, 1973; Weertman, 1970). The laboratory experiments show that the rheology of mantle minerals is significantly affected by temperature and deviatoric stress. Poirier (1993) demonstrated the dependence of mantle viscosity on temperature and pressure. Karato (1989) showed that due to the effect of pressure, the viscosity within the mantle should increase with depth. Some of my models that are presented in chapter 2 were run with depth-dependent viscosity.

Based on seismological evidence, the mantle is divided into different sections viz., the upper

mantle (30 to 410 km depth), the transition zone (410 to 660 km depth) and the lower mantle (660 to 2890 km depth). The seismic discontinuity near 660 km contains the sharpest changes in seismic properties within the mantle. The results of Ito and Takahashi (1989), Richards and Wicks (1990), Niu and Kawakatsu (1995) Vidale and Benz (1992) and Castle and Creager (1997) offer compelling evidence that the 660 km boundary marks the transformation of γ-spinel to magnesium-perovskite and magnesiowüstite in the olivine system, where the reaction is endothermic and has a negative Clapeyron slope $\mathrm{dP/dT} \simeq -2.6 \pm 0.2\,\mathrm{MPaK}^{-1}$ (Akaogi et al., 2007). Fig. 1.3 gives an example of the evidence of the transition zone in three different tomographic sections of the Tonga-Kermadec trench as demonstrated by Mussett and Khan (2000).

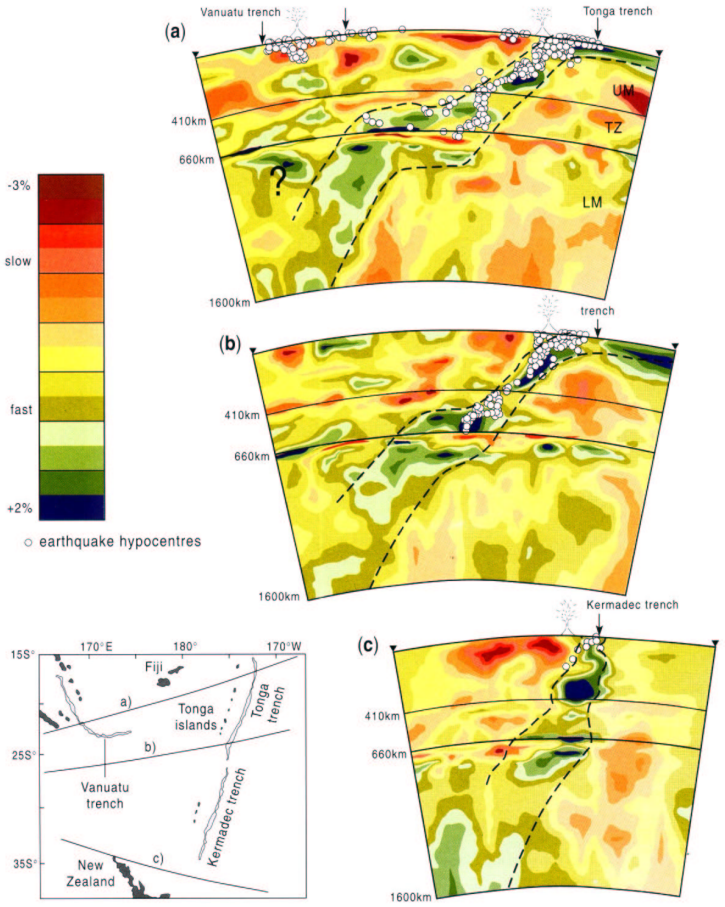

Figure 1.3: Seismic tomographic sections of the Tonga-Kermadec trench showing the transition zone in the mantle (Mussett and Khan, 2000). The subducting plate is revealed as a zone of higher velocity (in dark green) caused by a lower temperature than the surrounding mantle. In these three sections, the dashed lines indicate the boundaries of the subducting slab. Section (a) and (b) clearly show slab deflection just above the 660 km discontinuity.

It has long been recognized that the transition zone in the mantle holds the key to understanding the dynamical behavior of the mantle and its thermal evolution (Verhoogen, 1965), yet the issue of the degree of convective layering at 660 km-depth remains unresolved. The seismicity distribution in subduction zones and the shapes of subducting slabs at that depth, observed from seismic tomography, give evidence about the mantle transport dynamics at 660 km-depth (e.g. van der Hilst, 1991, 1995; Fukao et al., 1992; Kennett and Gorbatov, 2004; Ritsema et al., 2004; Zhao, 2004). The images from seismic tomography show (e.g. fig. 1.3a and 1.3b) distinct slab flattening along the boundary in some locations (Fukao et. al., 2001) and penetration (Kito et. al., 2008) across the endothermic phase boundary in others, which means that the mantle is probably incompletely layered.

In a review paper, Christensen (1995) commented on the possible incomplete layering of the Earth's mantle based on different numerical and seismic tomographic studies. The 660 km endothermic phase transition boundary deflection impedes and the latent heat induced thermal buoyancy drives convection. Christensen (1995) determined that the value of the current Clapeyron slope for the post-spinel transition is marginal to cause a complete layering of the mantle. Similar effects in the layering can be observed in the models that are shown in chapter 4. Various studies using numerical models (Christensen and Yuen, 1985; Zhao et al., 1992; Honda and Yuen, 1994; Solheim and Peltier, 1994a, b; Yuen et al., 1994; Butler and Peltier, 2000), which looked at the effects of the phase boundary on mantle flow and parameterized models (McKenzie and Richter, 1981; Honda, 1995; Butler and Peltier, 2002), which looked at the effects of layering on thermal evolution, have been done in order to understand the problem. I constructed a parameterized model and compared it with some of my numerical model results in appendix C.

An early study by Christensen and Yuen (1985) demonstrated that the endothermic phase transition could produce layering in the mantle, provided the Clapeyron slope of the reaction is sufficiently steep. They also showed a significant increase in the degree of layering with increasing Rayleigh number. In their 1×1 aspect ratio calculations they observed a sudden increase in the degree of layering between Clapeyron slope values of $-5\,\mathrm{MPaK}^{-1}$ and $-6\,\mathrm{MPaK}^{-1}$. In chapter 4, I will show a similar jump in the results of unit aspect ratio calculations and also that the degree of layering is strongly affected by the aspect ratio of convection. Models of isoviscous convection at higher Rayleigh numbers (Machetel and Weber, 1991; Peltier and Solheim, 1992; Zhao et al., 1992; Solheim and Peltier, 1993, 1994a, b; Tackley et al., 1993; Weinstein, 1993) show basically the same tendency toward layering in the presence of the endothermic phase change as the Rayleigh number of the convection increases, but the magnitude of the Clapeyron slope is smaller and convection is less layered.

The distinct heterogeneity in the surface boundary condition produced by the presence of the continental lithosphere affects mantle convection. Continental rocks, which are less dense and

therefore more buoyant than mantle rocks, do not subduct. Previously numerical studies have shown a number of ways to model tectonic plates. Some of the methods are listed here. Imposing a temperature-dependent viscosity (e.g. Christensen, 1984; Jaupart and Parsons, 1985) or surface velocity (e.g. Lux et al., 1979; Jarvis and Peltier, 1981; Houseman, 1983; Davies, 1984) have been popular in modeling plates. Davies (1988) has used both temperature-dependent viscosity and imposed horizontal surface velocity together in order to mimic the effects of tectonic plates, whereas, Grigné et al. (2007a, b) have incorporated continents in their model by placing a lid of finite thickness and conductivity at the surface together with a shear-stress free mechanical boundary condition. A combination of high viscosity (almost 1000 times greater) contrast and the force balance method to compute the plate velocity has also been used to model cold lithosphere (e.g. Gable et al., 1991; King et al., 1992; Lowman et al., 2003; Lowman et al., 2004; Gait and Lowman, 2007b; Lowman et al., 2008; Monnereau and Quéré, 2001).

Various studies have been done numerically and experimentally in order to investigate the effects of continents on mantle convection. Numerical and laboratory models of the Wilson cycle explain this phenomenon in terms of floating continental crust and lithosphere interacting dynamically with mantle convection (Gurnis, 1988; Zhong and Gurnis, 1993; Guillou and Jaupart, 1995; Lowman and Jarvis, 1995, 1996). Numerical calculations (e.g. Grigné et al., 2007a) have demonstrated that hot upwellings tend to form underneath the continents producing extensional stress, further resulting in continental break-up. This phenomenon is also observed in models with continents in chapter 4. Two-dimensional Cartesian and cylindrical mantle convection models (Lowman and Jarvis, 1993; Ghias and Jarvis, 2007) have shown that upon the break-up of the supercontinent, the continental blocks disperse. At this point separate upwellings form beneath the continental blocks leading them back together once again as a supercontinent and this whole process repeats itself. They have defined this as a flow reversal, which also resembles a Wilson cycle. The presence of hot upwellings under the continents and flow reversal phenomenon were also observed in some other studies (Gurnis, 1988; Bobrov and Trubitsyn, 1995; Trubitsyn and Rykov, 1995). Accumulations of continental crust material can affect mantle convection in a number of other ways as brought out in a series of papers by Lenardic and Kaula (1995, 1996), Lenardic (1997, 1998) and Moresi and Lenardic (1997).

Lenardic (1998), using a model where the viscosity within the mantle is considered to be a function of temperature, showed that heat loss through the oceans increases relative to the heat loss through the continents as the convection becomes more vigorous, i.e. as the effective Rayleigh number, which indicates the presence and strength of convection within a fluid body, increases. This provides an explanation of the so-called Archean paradox, which comes about because of the fact that the continental geotherm in the Archean period were similar to those at present (e.g. Boyd et al., 1985) even though the Earth must have been hotter and the overall heat flow must have been

larger. Both of these suppositions are reconcilable if the heat flow through the oceans was a larger fraction of the Earth's total heat flow in the Archean compared to the present days. Lenardic and Moresi (2001,2003) investigated the variation of surface heat flow as a function of the thickness and the lateral extent of the thermally coupled continents. Their numerical and parameterized models show a good agreement at higher Rayleigh numbers. They also showed that the surface heat flow varies only weakly with the thickness of a continent provided that the continental thickness is much less than the depth of the mantle (Lenardic et al., 2005). The effects of continental crustal material on mantle convection have been explored by Moresi and Lenardic (1997) in a three dimensional Cartesian model similar to the two dimensional models discussed before.

Doin et al. (1997) used a two-dimensional numerical model to study how convective processes control the thickness of the continental and oceanic lithosphere and suggested that long-term preservation of a thick continental root requires both chemical buoyancy and enhanced viscosity of the root material. The increased viscosity of the continental lithosphere must have a non-thermal origin. Continents suppress the intensity of mantle convection (Trubitsyn and Fradkov, 1985). Studies were also done to see the effects of an overriding moving or stationary continent on downwelling flows (Trubitsyn et al., 1998). They reveal that moving continents produce an inclined subduction zone along its boundary and if it is not moving then the downwelling becomes vertical. Trubitsyn et al. (1991) also studied the effects of continents on mantle convection using a model in which a constant temperature gradient was applied at the upper boundary and showed that convection cells get stretched in the presence of continents.

Christensen (1983) investigated mantle heat flow beneath continents, dynamic topography and the free air anomaly at the surface, using a model consisting of two boxes, which were thermally and mechanically coupled at their interface. Similar studies of how continent-ocean differences influence mantle convection have been carried out by Rabinowicz et al. (1980), Mimouni and Rabinowicz (1988) and Walzer and Hendel (1997). All of these studies indicate that convection cells beneath continents can transfer heat laterally from the subcontinental mantle to adjacent oceanic regions, which is in agreement with Lenardic et al. (2005). I show in chapter 4 that the average oceanic heat flux increases when the continental coverage is 90% for isoviscous models. To understand these effects using laboratory experiments, Guillou and Jaupart (1995) placed thermo-conductive plates at the top of an experimental tank and showed that large-scale convection cells exist in conditions which, in the absence of continents, would lead to a chaotic convection pattern dominated by plumes.

Lowman and Jarvis (1993, 1995) carried out an investigation related to the influences of continental width, diffusivity, thickness and internal heating on continental collision and breakup. They used a two-layer model setup where the top layer represents continent, which is mechanically coupled by a mutual boundary condition with the lower layer representing mantle. The rigid upper

layer attained the velocity based on the viscous lower layer. They showed that the flow reversal phenomenon occurs even when the continental diffusivity is 4 times more than the mantle diffusivity.

My project involves two-dimensional numerical modeling of mantle convection in unit and wider aspect ratio boxes with the main objectives being 1) the study of the origin and significance of subadiabatic mantle temperature gradients, 2) observing any obvious difference between secular cooling and the effects of internal heating and 3) the study of the combined effects of continents and the 660 km-depth endothermic phase boundary on the thermal regime in the mantle. In chapter 2, I present a set of calculations demonstrating the different energy balance mechanisms in the mantle responsible for positive vertical temperature gradients. Some of the models include depth-dependent viscosity and different surface boundary conditions in order to observe their effect on the shape of the geotherm. This chapter was published in the Journal of Geophysical Research (Sinha and Butler, 2007). Chapter 3 contains a short study that was carried out to determine whether differences exist between the effects of secular cooling and radioactive heat generation in numerical models of the mantle. Another set of calculations are presented in chapter 4 showing the combined thermal effects of the endothermic phase boundary across 660 km-depth and different surface boundary conditions representing continental and oceanic lithosphere on the convection planform and subadiabaticity in the mantle. This chapter was published in the Physics of the Earth and Planetary Interiors (Sinha and Butler, 2009). I ran simulations in different aspect ratio boxes in order to investigate these effects as well. Chapter 5 summarizes all of the observed interesting results from the previous three chapters. In this chapter, I also discuss the significance of my new findings. In the appendices I include some useful mathematical derivations and unpublished studies.

Chapter 2

On the Origin and Significance of Subadiabatic Temperature Gradients in the Mantle

2.1 Introduction

It is often assumed that the temperature profile in the Earth's mantle outside of thermal boundary layers is close to adiabatic due to the dominance of advective heat transfer (e.g. Schubert et al., 2001). However, numerical simulations of convection scaled to the Earth's mantle have shown that in the presence of internal heating, which models the effects of radioactive decay, the temperature increases with depth more slowly than would be predicted assuming adiabaticity (e.g. McKenzie et al., 1974; Sotin and Labrosse, 1999; Matyska and Yuen, 2000; Bunge et al., 2001). Sleep (2003) and Bunge (2005) have estimated that the temperature increase from the base of the surface thermal boundary layer to the top of the basal thermal boundary layer is less, by roughly 400 K, than would be predicted if the mantle temperature profile were purely adiabatic. However, Zhong (2006) argues for only 180 K. This has significant consequences for estimates of the composition of the mantle (Mattern et al., 2005) as well as for mantle transport properties (Monnereau and Yuen, 2002). The presence of a subadiabatic thermal gradient in the mantle would also lead to a greater temperature drop across the core-mantle boundary, that would increase estimates of the heat flow in this region (Bunge, 2005). An increase in the estimated heat flow at the core-mantle boundary would, in turn, be of significance in determining the energy budgets for the mantle and core and would imply a young inner core (e.g. Butler et al., 2005; Davies, 2007).

Jeanloz and Morris (1987) presented a physical argument for the existence of a subadiabatic gradient in the interior of purely internally heated convecting systems. They assumed that subadiabatic gradients arise due to the balance between internal heating and vertical advection, and because of the asymmetry between upwellings and downwellings in internally heated flows. This argument, and similar ones (Sleep, 2003; Bunge, 2005) have been used to explain the existence of the subadiabatic gradient observed in internally heated convection models. It is also well known that an overshoot is often seen above the lower and below the upper thermal boundary layers in the horizontally-averaged internal temperature in convection models (e.g. McKenzie et al., 1974;

Blackenbach et al., 1989), which occurs because vertical flows are forced to turn horizontally at the top and bottom boundaries. The regions interior to these overshoots also correspond to regions of subadiabatic gradients. I will show that the basal overshoot becomes more pronounced as internal heating is increased, making a significant contribution to the total subadiabatic gradient.

Another mechanism causing regions of subadiabaticity is only present when convection is time-dependent. Every transient plume has super and subadiabatic regions (Matyska and Yuen, 2002). Although this mechanism is significant, its effects on a time-averaged geotherm are very similar to those of the other two mechanisms. In section 2.2 I present in greater detail how these mechanisms can result in subadiabatic temperature gradients and in section 2.6 I examine in detail the energy balance in regions of subadiabaticity in order to determine the relative importance of each mechanism.

Depth-dependent viscosity (e.g. Gurnis and Davies, 1986; Cserepes, 1993; Bunge et. al., 1996) and the thermal effects of continents (e.g. Guillou et. al., 1995; Lenardic et. al., 2005) are significant factors affecting convective heat transport in the mantle. In sections 2.6.1 and 2.6.2, I analyze the effects of depth-dependent viscosity and different surface boundary conditions, representing the effects of continents, on mantle subadiabaticity.

Sotin and Labrosse (1999) presented a series of calculations with mixed basal and internal heating and were able to achieve excellent agreement with a parameterized model for the average temperature and surface heat flux. The core-mantle boundary heat flux could not be calculated in their parameterized model based on the interior temperature, however, and these authors argued that the subadiabatic gradient in the lower mantle would need to be taken into account in order to achieve such an agreement. In section 2.6.4, I demonstrate that an improved fit is achieved when the subadiabatic gradient is considered.

2.2 Mechanisms Resulting in Subadiabatic Gradients

In order to achieve the greatest possible simplicity, I consider an incompressible Boussinesq system. The temperature, T, in the energy equation can then be considered as an approximation for the potential temperature in a compressible system (Jarvis and McKenzie, 1980), where I have neglected the terms due to thermal conduction along the adiabat as well as viscous dissipation, which are generally small. Using this approximation, when the temperature is constant with height, I will consider the system to be adiabatic. When temperature increases or decreases with height, the system is then said to be subadiabatic or superadiabatic, respectively. The non-dimensional equation governing the temperature, T, is then

$$-\frac{\partial T}{\partial t} - \mathrm{u}\frac{\partial T}{\partial x} - \mathrm{v}\frac{\partial T}{\partial z} + \nabla^2 T + H = 0 \tag{2.1}$$

where t, u, v and H are time, horizontal and vertical velocity and internal heating parameter, respectively. The terms in the equation (from left to right) represent the addition of heat to an infinitesimal volume by local secular cooling, horizontal advection, vertical advection, diffusion and internal heating, respectively. The equation has been non-dimensionalized using scales for distance, d, time, d^2/κ, and temperature change, ΔT, where d, κ and ΔT are the depth, thermal diffusivity and the total temperature drop across the mantle, respectively. The resulting non-dimensional internal heating parameter, H, is then $(\chi d^2 \rho)/(\Delta T k)$ where χ, ρ and k are the internal heating rate per unit mass, density and thermal conductivity of mantle material, respectively. In all of my calculations, I have run the models to a steady state, or statistically steady state, so that the volume-averaged local secular cooling term is small. A statistical steady state is achieved when the mean value within a moving-window of the spatially-averaged temperature or the heat flux is constant. In most calculations, this was done visually and was found to be adequate. This term could also be combined with H to give an effective internal heating rate. However, I will show that in time-dependent calculations, the local secular cooling term is often locally a dominant term in the energy balance even when its volume-average is minimal.

Jeanloz and Morris (1987) presented a physical argument for the existence of a subadiabatic temperature gradient in purely internally heated convective systems. They assumed that the diffusion and the horizontal contributions to advection are negligible everywhere except within the boundary layers. This leaves a balance between vertical advection and internal heating,

$$\mathrm{v}\frac{\partial T}{\partial z} = H. \tag{2.2}$$

Since H is always positive in regions of upwelling ($\mathrm{v} > 0$) the temperature gradient will be subadiabatic ($\partial T/\partial z > 0$), while in regions of downwelling the temperature gradient will be superadiabatic. Physically, heat is added by internal heating to both hot-rising and cold-sinking parcels of fluid, leading to sub and superadiabatic temperature variations. Note that the deviation from a state where $\partial T/\partial z = 0$ decreases with the magnitude of the vertical velocity for a given value of H. For this reason, in fast moving slabs and plumes, the temperature gradient predicted by this model is close to adiabatic. In internally heated convection, the effects of subadiabatic upwellings and superadiabatic downwellings will not cancel out when the temperature is averaged horizontally due to the asymmetry between upwellings and downwellings in internally heated convection. In the presence of strong internal heating, downwelling occurs in narrow, high-velocity regions while upwellings travel at a much lower speed and occur over a much wider horizontal distance (e.g. Jarvis and Peltier, 1982 in their basally heated models). As a result of the greater area that the upwellings cover and because they are strongly subadiabatic, while the downwellings are only weakly superadiabatic, the mean temperature variation with depth will be subadiabatic.

In order to quantify the magnitude of this effect for the Earth, I can consider the potential temperature in a rising parcel of fluid where the energy balance is given by equation 2.2. For the

Earth, the total surface heat flow is roughly 44 TW (Pollack et al., 1993), of which roughly 8 TW comes from radioactivity in the continental crust (Hart and Zindler, 1986) resulting in roughly 36 TW of energy coming from convection in the mantle. If all of this is attributed to the combined effects of internal heating and secular cooling within the mantle (i.e. there is no flux of heat from the core), I can calculate an upper bound for $H_{eff} = (\chi_{tot} d^2 \rho)/(M \Delta T k) = 30.5$. Here I have combined secular cooling and internal heating to give an effective internal heating, H_{eff}, and $\chi_{tot} = 36\,\mathrm{TW}$ and M are the total internal heating rate and total mass of the mantle ($4 \times 10^{24}\,\mathrm{kg}$) and I have used typical mantle values for $\rho = 4500\,\mathrm{kg/m^3}$, $\Delta T = 3700\,\mathrm{K}$ and $k = 3\,\mathrm{W/mK}$ (Schubert et al., 2001). Using equation 2.2 I can derive an expression for the total subadiabatic temperature drop for a fluid parcel rising at a constant speed, v_0, with an energy addition given at a rate controlled by H and inverting this for v_0 gives, $\mathrm{v}_0 = H/\Delta T_{sub}$. In order to have a subadiabatic temperature drop that is at least 10% of the total temperature drop across the mantle, I require a non-dimensional mean vertical velocity of no more than $\mathrm{v}_0 = 305$ or $0.18\,\mathrm{cm/yr}$ after dimensionalizing. This value is roughly less by a factor of 20 than the mean plate velocity of $4\,\mathrm{cm/yr}$. As a result, the slow upward return flow must be significantly slower than the flows in mantle plumes or descending slabs for this mechanism to be significant. I will show it is only large in calculations with large values of H and I will refer to this mechanism hereafter as VA-H. Also, using my numerical results, I will demonstrate that the balance given in equation 2.2 is not the only mechanism that causes mantle subadiabaticity.

Another situation where regions of subadiabatic temperature gradients are observed, occur even in purely basally heated convection. Temperature overshoots often occur just inside the top and bottom thermal boundary layers where subadiabatic gradients occur on the interior of these overshoots. They occur because vertical flows are forced to turn due to the presence of the top and bottom boundaries. In the subadiabatic portions of the overshoot the dominant energy balance is between the vertical and horizontal contributions to advection (Jarvis and Peltier, 1982). McKenzie et al. (1974) showed examples of increased overshoot at the bottom boundary and decreased overshoot at the top boundary when internal heating was increased. In their study of convection with mixed internal and basal heating, Sotin and Labrosse (1999) observed that a small degree of internal heating resulted in the disappearance of the overshoot at the upper thermal boundary layer. I further investigate the increasing asymmetry between the top and bottom overshoots and their cause in section 2.6. This overshoot-forming mechanism will be referred to hereafter as VA-HA.

When the calculation is time-dependent, the balance between local secular cooling and the other terms in the energy equation, becomes significant. This mechanism remains significant in the energy balance at a given location, even after the model is run to a statistical steady state. However, it does not make large changes to the time-averaged geotherm. This mechanism only replaces VA-H and VA-HA and as a result the geotherm is not significantly affected by it. As an example, if the

subadiabatic gradient due to the overshoot is displaced up or down by transient flow, the local secular cooling will be one of the dominant terms in the energy equation. From now on I will refer to this mechanism as SC. In fig. 2.1, I show the terms in the energy equation that have been used to calculate the different energy balances discussed above.

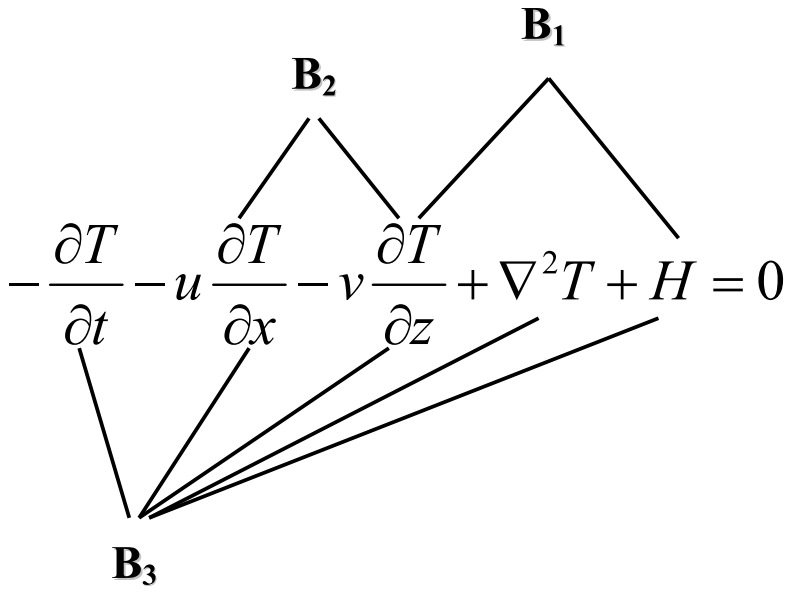

Figure 2.1: The different terms in the energy equation used to calculate the dominant energy balances.

2.3 Derivations of the Governing Equations in 2D for Isoviscous and Variable Viscosity Calculations

The classical hydrodynamic field equations (Chandrasekhar, 1961) in tensor notation for the conservation of mass, momentum and energy can be written as

$$\frac{\partial \rho}{\partial t} + \frac{\partial}{\partial x_j}(\rho u_j) = 0, \tag{2.3}$$

$$\rho\left(\frac{\partial u_i}{\partial t} + u_j \frac{\partial u_i}{\partial x_j}\right) = -g\rho\delta_{i3} + \frac{\partial \tau_{ij}}{\partial x_j} \tag{2.4}$$

and

$$\rho\left(\frac{\partial E}{\partial t} + u_j \frac{\partial E}{\partial x_j}\right) = \frac{\partial}{\partial x_j}\left(k\frac{\partial T}{\partial x_j}\right) + H - p\frac{\partial u_k}{\partial x_k} + \Phi \tag{2.5}$$

where the stress term is

$$\tau_{ij} = -p\delta_{ij} + \eta\left(\frac{\partial u_i}{\partial x_j} + \frac{\partial u_j}{\partial x_i} - \frac{2}{3}\frac{\partial u_k}{\partial x_k}\delta ij\right) \tag{2.6}$$

and the viscous dissipation term is

$$\Phi = \frac{\eta}{2}\left(\frac{\partial u_i}{\partial x_j} + \frac{\partial u_j}{\partial x_i}\right)^2 - \frac{2}{3}\eta\left(\frac{\partial u_k}{\partial x_k}\right)^2. \tag{2.7}$$

These equations can be used as the generalized forms for both 2D and 3D systems. Here, ρ is the density, u_i are the velocities, δ_{ij} is the Kronecker delta, E is the internal energy per unit mass ($=c_pT$, where c_p is the specific heat), T, t and k are the temperature, time and the thermal conductivity, respectively, H is the internal heating rate within the mantle per unit mass, η and p are the dynamic viscosity and the pressure term.

In the mantle, an adequate equation of state assumes a linear dependence of density on temperature

$$\rho = \rho_r[1 - \alpha(T - T_r)] \tag{2.8}$$

where T_r is a reference temperature, ρ_r is the density at that temperature and α is the thermal expansion coefficient.

My model is Boussinesq-incompressible (both spatial and temporal derivatives of density are zero except in the buoyancy term) and I consider a Newtonian fluid (stress is proportional to strain rate) with infinite Prandtl number (fluid loses momentum much faster than heat). Now, after taking into account all three assumptions, equations (2.3), (2.4) and (2.5) can be written in vector notation as, respectively,

$$\nabla \cdot \mathbf{u}' = 0 \tag{2.9}$$

$$T'\hat{k} - \nabla \cdot \tau = 0 \tag{2.10}$$

$$\frac{\partial T'}{\partial t'} + \mathbf{u}' \cdot \nabla T' = \frac{1}{Ra}\nabla^2 T' + H \tag{2.11}$$

where all the parameters are non-dimensional and they have been non-dimensionalized using the following relations,

$$(x, z) = d(x', z');\ t = \frac{d^2}{\kappa Ra}t';\ \mathbf{u} = \frac{\kappa Ra}{d}\mathbf{u}';\ T = \Delta T T'. \tag{2.12}$$

Here, κ, d and Ra are the thermal diffusivity, the depth of the mantle and the Rayleigh number, respectively. The expression for the Rayleigh number is

$$Ra = \frac{\rho\, g\alpha\, \Delta T d^3}{\eta\kappa}. \tag{2.13}$$

From now on all the equations are non-dimensional unless stated otherwise. If η is considered as a constant within the system, then the momentum equation can be written as

$$T\hat{k} - \nabla p + \nabla^2 \mathbf{u} = 0. \tag{2.14}$$

Because I use a stream-function-vorticity (ψ-ω) formulation, the momentum equation needs to be converted to a pair of Poisson's equations for two-dimensional calculations. Vorticity can be mathematically written as

$$\omega = \hat{j} \cdot \nabla \times \mathbf{u}. \tag{2.15}$$

Now if I take $\nabla\times$ of (2.14) and use (2.15)

$$-\frac{\partial T}{\partial x} + \nabla^2 \omega = 0. \tag{2.16}$$

or

$$\nabla^2 \omega = \frac{\partial T}{\partial x}. \tag{2.17}$$

If u_x and u_z are the velocities along $\mathbf{x}$ (horizontal) and $\mathbf{z}$ (vertical) directions and ψ is the stream function, the velocities can be written as

$$u_x = \frac{\partial \psi}{\partial z},\ u_z = -\frac{\partial \psi}{\partial x}. \tag{2.18}$$

Substituting this into (2.15)

$$\omega = \frac{\partial u_x}{\partial z} - \frac{\partial u_z}{\partial x} = \frac{\partial^2 \psi}{\partial^2 z} + \frac{\partial^2 \psi}{\partial^2 x} = \nabla^2 \psi. \tag{2.19}$$

At the end the two governing Poisson's Equations for my isoviscous 2D calculations can be written as

$$\nabla^2 \psi = \omega \tag{2.20}$$

and

$$\nabla^2 \omega = \frac{\partial T}{\partial x}. \tag{2.21}$$

Next I will derive a similar expression for calculations where η is variable in space. The horizontal ($\mathbf{x}$) and the vertical ($\mathbf{z}$) components of the momentum equation in (2.10) can separately be written as

$$\frac{\partial \tau_{xx}}{\partial x} + \frac{\partial \tau_{xz}}{\partial z} = 0 \tag{2.22}$$

and

$$T + \frac{\partial \tau_{zx}}{\partial x} + \frac{\partial \tau_{zz}}{\partial z} = 0. \tag{2.23}$$

The normal stress terms are expressed as

$$\tau_{xx} = -p + 2\eta \frac{\partial u_x}{\partial x} \tag{2.24}$$

and

$$\tau_{zz} = -p + 2\eta \frac{\partial u_z}{\partial z}. \tag{2.25}$$

Using the variable ω, the tangential stress terms can be written as

$$\tau_{xz} = \eta \left(2\frac{\partial u_z}{\partial x} + \omega \right) \tag{2.26}$$

and

$$\tau_{zx} = \eta \left(2\frac{\partial u_x}{\partial z} - \omega \right). \tag{2.27}$$

Substituting the expressions for the normal and the tangential stress terms in equations (2.22) and (2.23) I get

$$\frac{\partial}{\partial x}\left(-p + 2\eta \frac{\partial u_x}{\partial x} \right) + \frac{\partial}{\partial z}\left[\eta \left(2\frac{\partial u_z}{\partial x} + \omega \right) \right] = 0 \tag{2.28}$$

and

$$T + \frac{\partial}{\partial x}\left[\eta \left(2\frac{\partial u_x}{\partial z} - \omega \right) \right] + \frac{\partial}{\partial z}\left(-p + 2\eta \frac{\partial u_z}{\partial z} \right) = 0. \tag{2.29}$$

After differentiating (2.28) w.r.t. $\mathbf{z}$ and (2.29) w.r.t. $\mathbf{x}$, subtracting one from the other and simplifying using the continuity equation $\nabla \cdot \mathbf{u} = 0$, the equation to solve for ω can be written as

$$\nabla^2(\Omega) = \frac{\partial T}{\partial x} + 2\frac{\partial^2 \eta}{\partial x^2}\frac{\partial u_x}{\partial z} - 2\frac{\partial^2 \eta}{\partial z^2}\frac{\partial u_z}{\partial x} - 4\frac{\partial^2 \eta}{\partial x \partial z}\frac{\partial u_x}{\partial x} \tag{2.30}$$

where $\Omega = \eta\omega$.

The equation to solve for ψ can be written as

$$\nabla^2 \psi = \frac{\Omega}{\eta}. \tag{2.31}$$

The equations for the generalized 3D problem can be found in appendix A.

2.4 Numerical Model Description

I solve equation 2.1 (or 2.11) and the infinite Prandtl number Navier-Stokes equations converted to stream-function-vorticity formulation as shown in the previous section using finite-difference method on 289×289, 1153×289 and 2305×289 grids in 1×1, 4×1 and 8×1 boxes, respectively. The calculations for $Ra = 10^8$ were carried out with a resolution of 1153×1153.

Some of my models included the effect of a jump in viscosity at a non-dimensional height of 0.77, which is appropriate to 660 km depth in the mantle. I have plotted the vertical viscosity profile with depth in fig. 2.2. I use the following equation to describe the vertical variation in viscosity, μ,

$$\mu(z) = \left(\frac{\mu_j - 1}{2}\right) \tanh(\lambda(z_{660} - z)) + \left(\frac{\mu_j + 1}{2}\right) \tag{2.32}$$

where μ_j is the total jump in the viscosity and λ is a dimensionless width parameter which controls the smoothness in the viscosity jump and I take it to have a value of 50. In stratified viscosity calculations the Rayleigh number is based on the viscosity in the upper mantle. The stream-function-vorticity pair of Poisson's equations both for isoviscous (2.20 and 2.21) and variable viscosity (2.30 and 2.31) calculations were solved using MUDPACK (Adams, 1991).

In models that include the effects of continental lithosphere, an insulating layer of thickness h_c is placed on the top of the solution domain. Emplacement of the conducting lid changes both the thermal and mechanical boundary conditions. Throughout this thesis the terms "conducting lid" and "continental lithosphere" have equivalent meaning and are used interchangeably. The thermal condition is achieved by assuming the heat flux at the base of the continental lithosphere is the same as the heat flux at the surface and the mechanism of heat transport in the continent is purely conductive. If I take the mantle and the continental thermal conductivities to be equal,

$$k_e \frac{T_s - T_b}{h_c} = \frac{\partial T}{\partial z}|_{z=1} \tag{2.33}$$

where T_s and T_b are the temperatures at the surface and the base of the continental lithosphere and I evaluate $\partial T/\partial z$ at the base of the continent. The parameter k_e is the effective conductivity, which is defined as the ratio between the conductivities of the continent and the underlying mantle. I assume $k_e = 1$ in all calculations. I solve for T_b(x) at each time-step and at each horizontal position beneath the continent as it serves as the top boundary temperature for that part of the mantle that is covered by a continent. Oceanic and continental regions are modeled as free-slip and no-slip mechanical boundary conditions, respectively. In order to implement mixed surface dynamical boundary conditions, I iterate the solution using the following expression for the surface vorticity,

$$\omega_{n+1} = \{0.5(\tanh(a(x - x_1)) + \tanh(a(x_2 - x)))\}(\omega_n - b\,\mathrm{u}_n), \tag{2.34}$$

where n is an iteration index, a describes the thickness of the transition between the free-slip and the no-slip region, x_1 and x_2 define the horizontal extent of the continent, b is empirically chosen

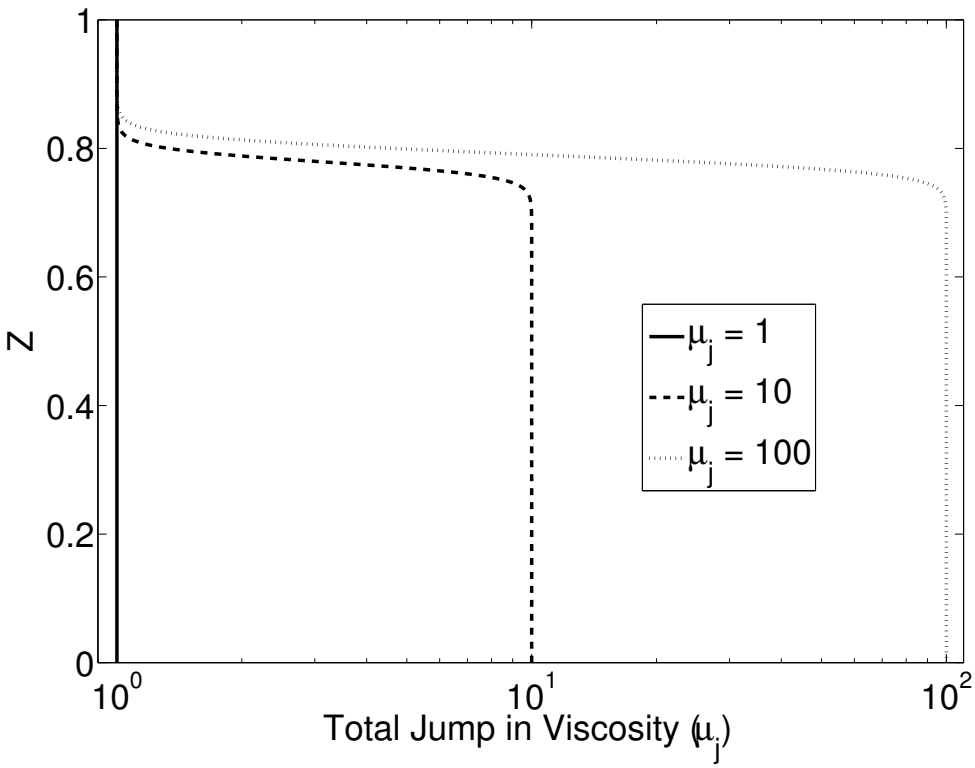

Figure 2.2: Average viscosity as a function of depth for a total viscosity jump $\mu_j = 1$, 10 and 100.

so as to give rapid convergence and u_n is the surface velocity as of the n^{th} iteration step. I use a similar method to incorporate the effects of continent also in chapter 4. Fig. 2.3 shows a plot of the surface velocity that was calculated using the expression.

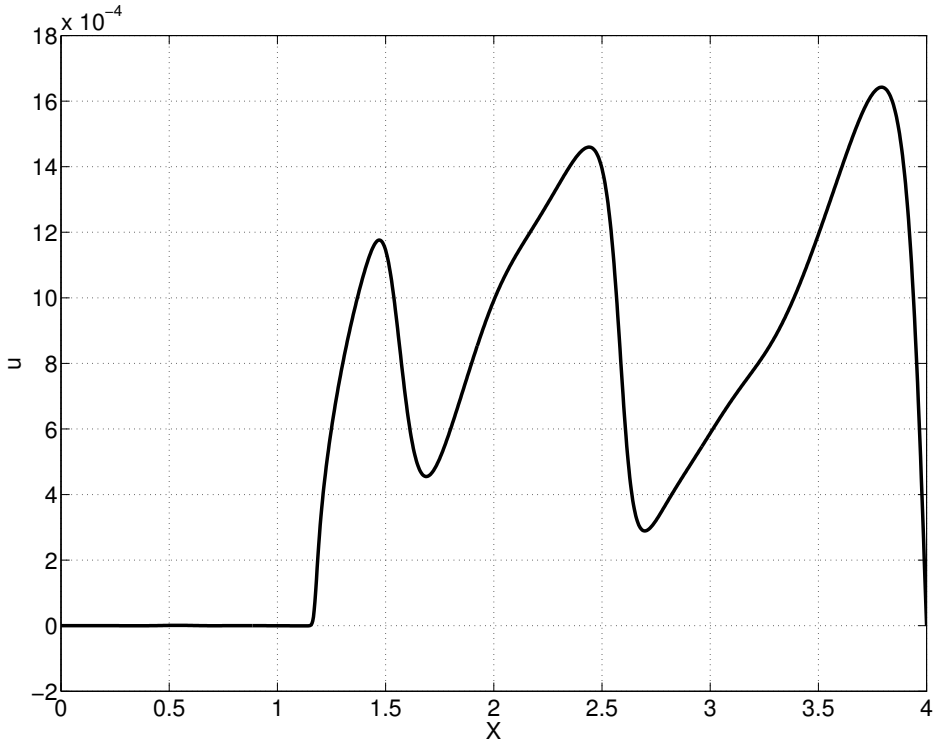

Figure 2.3: A snapshot of the surface velocity from a 4×1 calculation with $Ra = 10^6$, $H = 10$, $L = 1.2$ and $h_c = 0.04$ or model Ra6H10v1L1.2a4 $*$ (see table 2.1).

All of the boundaries have zero mass flux, while the side walls are reflecting and free-slip. The bottom boundary (core-mantle boundary) is also free slip and kept isothermal with a constant non-dimensional temperature $T = 1$ and except for the models with a conducting lid, the isothermal top surface is kept at a non-dimensional temperature of $T = 0$. Fig. 2.4 shows a diagram of my numerical model setup for the calculations that were carried out in this chapter. In this figure L is continental length.

For Ra $= 10^5$ calculations, I used a conduction profile of temperature as an initial condition. However, final temperature profiles from previous low Ra calculations were used to initialize models with higher Ra ($\geq 10^6$).

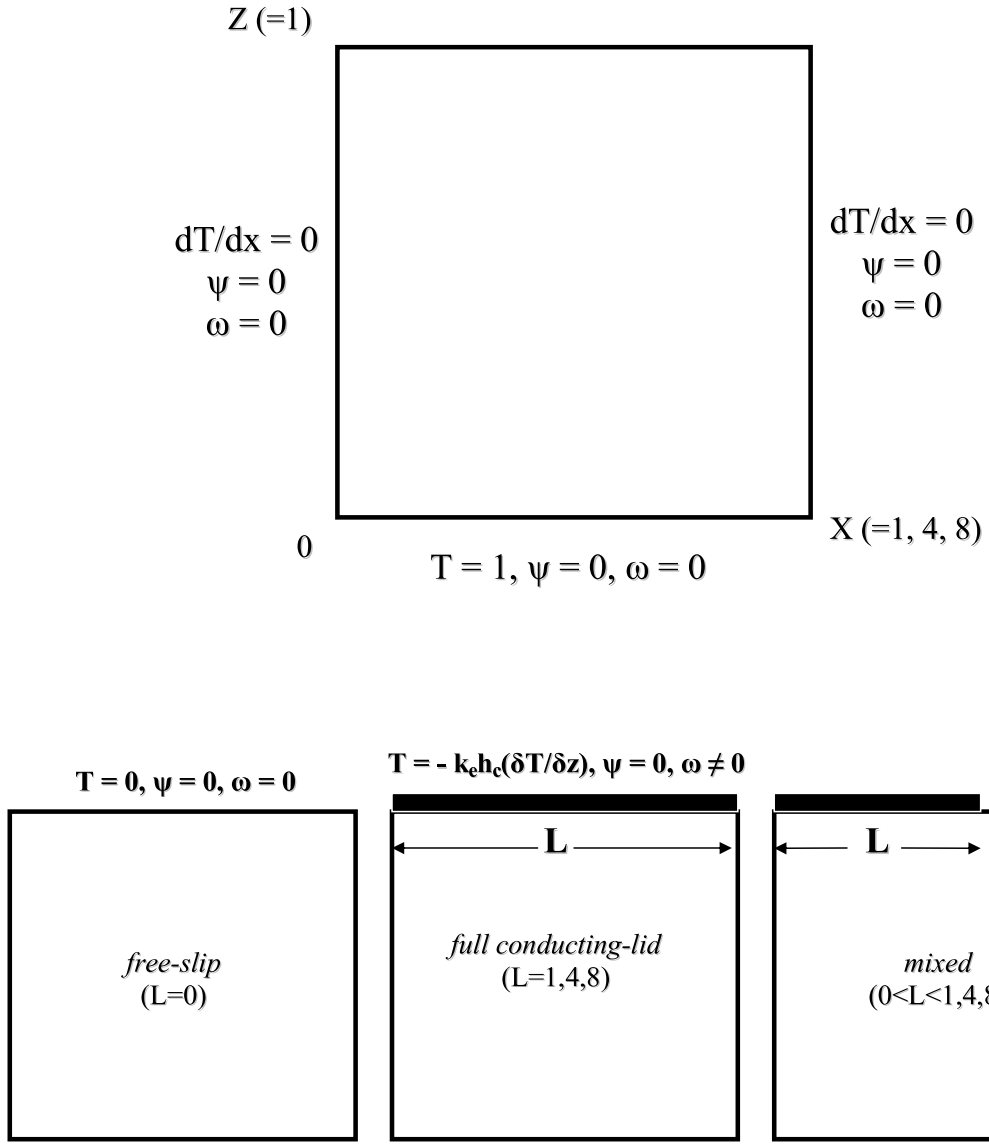

Figure 2.4: Numerical model setup showing the boundary conditions for vertical and horizontal boundaries.

2.5 Diagnostics

For each calculation I list the minimum and maximum temperatures along the geotherm outside the thermal boundary layers, T_{min} and T_{max}, average temperature, $< T >$, and the surface and core-mantle boundary heat fluxes, Q_s and Q_{CMB} (table 2.1). The difference between T_{max} and T_{min} gives the magnitude of the subadiabatic temperature drop, T_{sub} (table 2.1). I look for the terms in the energy equation (see fig. 2.1) with the highest positive and lowest negative values in order to determine the dominant balance at a point (table 2.2). I only consider the points where the vertical temperature gradient is positive. The value of SC indicates the percentage of the total subadiabatic temperature variation arising from volumes where local secular cooling is one of the dominant terms in the energy balance. The remaining columns VA-H, VA-HA and C-H indicate the percentage of the total subadiabatic temperature change arising from volumes where there is a dominant balance between vertical advection and internal heating, vertical and horizontal advection, and conduction and internal heating, respectively. I only list the most important energy balances in table 2.2, so the numbers do not sum to 100%. The quantity A_{sub} indicates the area of the domain with a positive temperature gradient. These terms are time-averaged when the solutions are time-dependent.

In the following section I analyze a number of simple calculations to determine where subadiabatic temperature gradients occur and the exact balance in the energy equation where they do. In subsequent sections I look at the effects of depth-dependent viscosity, surface boundary conditions and aspect ratio on subadiabatic temperature gradients. I then consider the effects of subadiabaticity on the core-mantle boundary heat flux and in the final section I discuss my results in the context of thermal convection in the Earth's mantle.

2.6 Numerical Model Results

M	A_r	Ra	H	μ_j	L	h_c	T_{min}	$< T >$	T_{max}	T_{sub}	Q_s	Q_{CMB}
Ra6H0v100a1	1	10^6	0	100	0	0	0.26	0.32	0.31	0.05	7.6	7.5
Raeff6H0v100a1	1	2.5×10^7	0	100	0	0	0.26	0.30	0.33	0.07	21.6	20.9
Ra6H0v10a1	1	10^6	0	10	0	0	0.34	0.38	0.41	0.07	14.3	14.2
Raeff6H0v10a1	1	3.5×10^6	0	10	0	0	0.34	0.38	0.41	0.07	21.2	21.3
Ra5H0v1a1	1	10^5	0	1	0	0	0.46	0.50	0.54	0.08	10.6	10.6
Ra5H0v1a4	4	10^5	0	1	0	0	0.45	0.50	0.55	0.1	8.06	8.06
Ra5H2.5v1a1	1	10^5	2.5	1	0	0	0.55	0.60	0.63	0.08	11.3	8.8
Ra5H2.5v1a4	4	10^5	2.5	1	0	0	0.55	0.60	0.65	0.1	9.5	7.0
Ra5H5v1a1	1	10^5	5	1	0	0	0.64	0.69	0.75	0.11	11.8	6.7
Ra5H5v1a4	4	10^5	5	1	0	0	0.65	0.67	0.75	0.1	9.9	4.7
Ra5H7.5v1a1	1	10^5	7.5	1	0	0	0.73	0.79	0.87	0.14	12.3	4.8
Ra5H7.5v1a4	4	10^5	7.5	1	0	0	0.75	0.77	0.87	0.12	10.9	3.4
Ra5H10v1a1	1	10^5	10	1	0	0	0.83	0.90	0.99	0.16	13	2.9
Ra5H10v1a4	4	10^5	10	1	0	0	0.84	0.89	0.99	0.15	13	2.9
Ra6H0v1a1	1	10^6	0	1	0	0	0.46	0.50	0.54	0.08	22.1	22.1
Ra6H0v1a4	4	10^6	0	1	0	0	0.46	0.50	0.54	0.08	15.8	16.0
Ra6H3v1a1	1	10^6	3	1	0	0	0.51	0.57	0.59	0.08	19.5	16.6
Ra6H3v1a4	4	10^6	3	1	0	0	0.51	0.57	0.6	0.09	19.3	16.2
Ra6H3v1a8	8	10^6	3	1	0	0	0.52	0.57	0.6	0.08	19.2	16.2
Ra6H4.5v1a1	1	10^6	4.5	1	0	0	0.53	0.59	0.62	0.09	20.0	15.4
Ra6H4.5v1a4	4	10^6	4.5	1	0	0	0.55	0.6	0.63	0.13	19.7	15.0
Ra6H10v1a1	1	10^6	10	1	0	0	0.61	0.65	0.67	0.06	23.6	13.6
Ra6H10v1a4	4	10^6	10	1	0	0	0.63	0.68	0.72	0.09	21.8	11.7
Ra6H10v1a8	8	10^6	10	1	0	0	0.63	0.68	0.71	0.08	21.7	11.8
Ra6H10v100a1	1	10^6	10	100	0	0	0.57	0.66	0.74	0.17	14.8	4.6
Raeff6H10v100a1	1	2×10^7	10	100	0	0	0.38	0.42	0.45	0.07	26.6	15.1
Ra6H10v10a1	1	10^6	10	10	0	0	0.63	0.73	0.8	0.17	16.9	6.8
Raeff6H10v10a1	1	6.2×10^6	10	10	0	0	0.47	0.54	0.55	0.08	26.6	17.6
Ra6H10v1L0.3a1∗	1	10^6	10	1	0.3	0.04	0.71	0.74	0.76	0.05	19.4	8.2
Ra6H10v1L1.2a4∗	4	10^6	10	1	1.2	0.04	0.72	0.76	0.82	0.1	17.8	7.9
Ra6H10v1L2.4a8∗	8	10^6	10	1	2.4	0.04	0.72	0.77	0.83	0.11	17.4	7.5
Ra6H10v1L0.4a1∗	1	10^6	10	1	0.4	0.04	0.68	0.75	0.78	0.1	20.8	10.6
Ra6H10v1L1.6a4∗	4	10^6	10	1	1.6	0.04	0.72	0.77	0.82	0.1	17.8	7.8
Ra6H10v1L3.2a8∗	8	10^6	10	1	3.2	0.04	0.72	0.76	0.82	0.1	17.8	7.8
Ra6H10v1L1a1	1	10^6	10	1	1	0	0.88	0.89	0.94	0.06	13.7	3.7
Ra6H10v1L4a4	4	10^6	10	1	4	0	0.84	0.84	0.88	0.04	14.4	4.4
Ra6H10v1L8a8	8	10^6	10	1	8	0	0.83	0.83	0.88	0.05	14.4	4.4
Ra6H10v1L1a1∗	1	10^6	10	1	1	0.04	1	1.02	1.05	0.05	11.2	-1.0
Ra6H10v1L4a4∗	4	10^6	10	1	4	0.04	0.99	0.99	1.02	0.03	10.1	0.1
Ra6H10v1L8a8∗	8	10^6	10	1	8	0.04	0.99	0.99	1.02	0.03	10.0	0.0
Ra6H18v1a1	1	10^6	18	1	0	0	0.78	0.85	0.9	0.12	25.3	7.3

Ra6H18v1a4	4	10^6	18	1	0	0	0.75	0.8	0.84	0.09	25.7	7.8
Ra6H18v1a8	8	10^6	18	1	0	0	0.75	0.8	0.84	0.09	25.7	7.7
Ra6H27v1a1	1	10^6	27	1	0	0	0.82	0.84	0.88	0.06	31.9	4.9
Ra6H27v1a4	4	10^6	27	1	0	0	0.87	0.92	0.98	0.11	30.8	3.5
Ra6H36v1a1	1	10^6	36	1	0	0	0.95	0.99	1.06	0.11	37.4	1.0
Ra6H36v1a4	4	10^6	36	1	0	0	0.98	1.05	1.13	0.15	36.2	0.1
Ra6H36v1a8	8	10^6	36	1	0	0	0.98	1.05	1.12	0.14	36.3	0.2
Ra7H0v1a1	1	10^7	0	1	0	0	0.48	0.50	0.52	0.04	38.0	38.0
Ra7H10v1a1	1	10^7	10	1	0	0	0.58	0.61	0.64	0.06	40.4	29.1
Ra7H20v1a1	1	10^7	20	1	0	0	0.62	0.67	0.68	0.06	45.0	25.0
Ra7H30v1a1	1	10^7	30	1	0	0	0.68	0.73	0.76	0.08	50.0	20.0
Ra7H40v1a1	1	10^7	40	1	0	0	0.75	0.80	0.83	0.08	55.0	15.0
Ra7H50v1a1	1	10^7	50	1	0	0	0.80	0.87	0.90	0.1	60.0	10.0
Ra7H60v1a1	1	10^7	60	1	0	0	0.87	0.94	0.98	0.11	67.0	7.0
Ra8H0v1a1	1	10^8	0	1	0	0	0.49	0.50	0.52	0.03	68.0	68.0
Ra8H10v1a1	1	10^8	10	1	0	0	0.52	0.56	0.57	0.05	76.0	66.0

Table 2.1: models, M; aspect ratio, A_r; Rayleigh number, Ra; non-dimensional internal heating, H; total jump in viscosity, μ_j; non-dimensional length and thickness of the continental lithosphere, L and h_c, respectively; T_{min} and T_{max} are the minimum and maximum internal horizontally-averaged temperatures, respectively; average temperature, $< T >$; temperature drop due to subadiabaticity, T_{sub} and Q_{CMB} and Q_s are the core-mantle boundary and surface heat fluxes, respectively.

† continent is located in the middle

$*$ models with partial or full conducting lid coverage

M	A_r	Ra	H	μ_j	L	h_c	VA-H(%)	VA-HA(%)	SC(%)	C-H(%)	A_{sub}(%)
Ra6H0v100a1	1	10^6	0	100	0	0	0	58.26	0.4	0	48.57
Raeff6H0v100a1	1	2.5×10^7	0	100	0	0	0.04	41.48	43.96	0.03	54.62
Ra6H0v10a1	1	10^6	0	10	0	0	0	76.75	0.02	0	47.75
Raeff6H0v10a1	1	3.5×10^6	0	10	0	0	0	78.37	0.06	0	51.51
Ra5H0v1a1	1	10^5	0	1	0	0	0	71.34	0.02	0	47.41
Ra5H0v1a4	4	10^5	0	1	0	0	0	70.63	0.18	0	53.34
Ra5H2.5v1a1	1	10^5	2.5	1	0	0	0.41	77.03	0	1.4	48.22
Ra5H2.5v1a4	4	10^5	2.5	1	0	0	0.82	25.59	64.18	0.91	51.49
Ra5H5v1a1	1	10^5	5	1	0	0	4.88	74.55	0	2.68	48.59
Ra5H5v1a4	4	10^5	5	1	0	0	2.29	17.24	71.03	1.27	46.55
Ra5H7.5v1a1	1	10^5	7.5	1	0	0	25.03	58.16	0	3.83	51.55
Ra5H7.5v1a4	4	10^5	7.5	1	0	0	7.24	15.84	67.13	1.75	47.98
Ra5H10v1a1	1	10^5	10	1	0	0	40.6	44.41	0	4.65	55.08
Ra5H10v1a4	4	10^5	10	1	0	0	17.07	15.31	58.22	2.26	52.43
Ra6H0v1a1	1	10^6	0	1	0	0	0	72	0.41	0	50.56
Ra6H0v1a4	4	10^6	0	1	0	0	0	43.03	49.24	0	49.11
Ra6H3v1a1	1	10^6	3	1	0	0	0.07	29.85	65.54	0.08	54.33
Ra6H3v1a4	4	10^6	3	1	0	0	0.16	35.15	60.16	0.09	52.88
Ra6H3v1a8	8	10^6	3	1	0	0	0.09	27.05	69.37	0.04	51.80
Ra6H4.5v1a1	1	10^6	4.5	1	0	0	0.4	31.68	63.03	0.2	54.46
Ra6H4.5v1a4	4	10^6	4.5	1	0	0	0.21	27.08	69.07	0.08	52.53
Ra6H10v1a1	1	10^6	10	1	0	0	3.93	62.48	0	5.32	60.80
Ra6H10v1a4	4	10^6	10	1	0	0	1.7	29.50	63.39	0.52	55.20
Ra6H10v1a8	8	10^6	10	1	0	0	0.95	26.73	67.70	0.38	53.96
Ra6H10v100a1	1	10^6	10	100	0	0	3.93	62.48	0	5.32	60.8
Raeff6H10v100a1	1	2×10^7	10	100	0	0	0.93	24.72	64.16	0.29	52.55
Ra6H10v10a1	1	10^6	10	10	0	0	21.29	48.68	9.34	6.73	49.36
Raeff6H10v10a1	1	6.2×10^6	10	10	0	0	1.04	31.12	61.88	0.19	54.05
Ra6H10v1L0.3a1∗	1	10^6	10	1	0.3	0.04	6.54	47.98	31.69	2.18	58.48
Ra6H10v1L1.2a4∗	4	10^6	10	1	1.2	0.04	1.52	21.19	73.43	0.33	55.38
Ra6H10v1L2.4a8∗	8	10^6	10	1	2.4	0.04	2.00	19.93	74.23	0.34	57.14
†Ra6H10v1L0.4a1∗	1	10^6	10	1	0.4	0.04	5.95	71.55	0	3.76	60.98
†Ra6H10v1L1.6a4∗	4	10^6	10	1	1.6	0.04	2.22	28.83	63.90	0.51	55.07
†Ra6H10v1L3.2a8∗	8	10^6	10	1	3.2	0.04	1.43	21.44	73.29	0.32	55.08
Ra6H10v1L1a1	1	10^6	10	1	1	0	38.04	42.51	0.5	6.16	58.63
Ra6H10v1L4a4	4	10^6	10	1	4	0	5.88	23.02	62.47	1.60	52.71
Ra6H10v1L8a8	8	10^6	10	1	8	0	4.56	20.73	67.43	1.34	52.06
Ra6H10v1L1a1∗	1	10^6	10	1	1	0.04	36.04	1.86	0.9	38.79	62.51
Ra6H10v1L4a4∗	4	10^6	10	1	4	0.04	17.48	13.21	54.72	6.70	61.44
Ra6H10v1L8a8∗	8	10^6	10	1	8	0.04	16.93	13.22	55.44	6.90	61.57
Ra6H18v1a1	1	10^6	18	1	0	0	18.32	31.64	37.94	3.20	63.72
Ra6H18v1a4	4	10^6	18	1	0	0	4.46	28.34	61.14	1.08	55.93
Ra6H18v1a8	8	10^6	18	1	0	0	4.29	28.72	61.21	1.02	55.59
Ra6H27v1a1	1	10^6	27	1	0	0	34.27	24.46	0.48	11.91	62.15

Ra6H27v1a4	4	10^6	27	1	0	0	10.69	24.29	58.40	1.65	59.33
Ra6H36v1a1	1	10^6	36	1	0	0	25.93	20.21	35.53	6.52	65.53
Ra6H36v1a4	4	10^6	36	1	0	0	16.17	19.88	54.64	4.19	68.65
Ra6H36v1a8	8	10^6	36	1	0	0	14.54	20.89	56.37	3.62	68.09
Ra7H0v1a1	1	10^7	0	1	0	0	0.45	36.68	61.54	0.01	49.37
Ra7H10v1a1	1	10^7	10	1	0	0	0.16	22.31	75.02	0.05	55.45
Ra7H20v1a1	1	10^7	20	1	0	0	0.07	28.96	68.4	0.01	52.14
Ra7H30v1a1	1	10^7	30	1	0	0	0.12	18.2	76.81	0.08	50.52
Ra7H40v1a1	1	10^7	40	1	0	0	0.31	22.16	72.44	0.15	56.28
Ra7H50v1a1	1	10^7	50	1	0	0	1.38	29.46	62.35	0.11	58.94
Ra7H60v1a1	1	10^7	60	1	0	0	0.77	15.35	78.92	0.07	68.31
Ra8H0v1a1	1	10^8	0	1	0	0	1.1	4.9	93.71	0.01	50.6
Ra8H10v1a1	1	10^8	10	1	0	0	1.28	4.44	85.04	2.26	70.1

Table 2.2: Models, M; aspect ratio, A_r; Rayleigh number, Ra; non-dimensional internal heating, H; total jump in viscosity, μ_j; non-dimensional length and thickness of the continental lithosphere, L and h_c, respectively; energy balance between local secular cooling and the other terms, SC; VA-H, VA-HA and C-H are the energy balances between vertical advection-internal heating, vertical-horizontal advection and conduction-internal heating, respectively; percentage of the points with positive vertical temperature gradient, A_{sub}.

† continent is located in the middle

$*$ models with partial or full conducting lid coverage

In fig. 2.5 I show results of calculation Ra5H10v1a1, run with $Ra = 10^5$ and $H = 10$, where the ratio of internal heating to total heat flux (Urey ratio) is 0.77 . I first consider this calculation with a relatively low Rayleigh number and unit aspect ratio because of the clarity afforded by displaying results that consist of only one convective roll in the absence of boundary layer instabilities. Fig. 2.5a displays the steady-state temperature field, while in fig. 2.5b I display a filled color contour plot indicating the dominant balance between different terms of the energy equation at each point within the box. The method of calculating the dominant balance at a point has previously been discussed in section 2.5. The filled contours are overlain by a vertical temperature gradient line contour plot where only the positive contours (places where $\partial T/\partial z > 0$) have been shown. I only plot the positive part of the vertical temperature gradient since the large superadiabatic temperature variation in the boundary layers overwhelms the small signal from the positive temperature gradient. Every integer value in the balance plot indicates a particular dominant balance between two different terms in the energy equation (described in the figure caption). In order to maintain a consistent color scheme I use the same colorbar for all plots of this type. As can be seen, and as is characteristic of strongly internally heated convection, the flow field is strongly asymmetric with a narrow region of rapid downwelling on the left-hand side of the box and slow upward flow (shown by the overlaying arrow plot) occurring over the rest of the domain. The geotherm for this calculation can be seen in fig. 2.7a. The broad bottom overshoot in the geotherm is caused by the large area of positive vertical temperature gradient associated with the dominant balance between vertical and horizontal advection, VA-HA (shown as green in fig. 2.5b). In models without internal heating, symmetric overshoots are seen adjacent to the top and bottom thermal boundary layers.

Matyska and Yuen (2002) reported similar subadiabaticity above regions where cold, avalanche material had ponded at the base of a simulation with phase transitions and temperature-dependent viscosity. In calculation Ra5H10v1a1 the upwelling at the top boundary is very broad and the ambient temperature is essentially the same as the temperature in the upwelling, resulting in very little horizontal advection of heat and hence no overshoot.

The cross-like pattern (shown in brown) in fig. 2.5b, that can be seen in the regions where conduction and internal heating are balancing one another, occurs at the center of the convection roll, where vertical and horizontal velocities are 0. Within much of the slow upward return flow the dominant balance in the energy equation is between internal heating and vertical advection (VA-H), that leads to the broad area of low amplitude positive thermal gradient (shown as orange in fig. 2.5b). Although the positive gradient associated with the overshoot at the base of this calculations appears to make a larger contribution to the subadiabatic gradient, the data in table 2.2 indicate that mechanisms VA-H and VA-HA make similar contributions to the total subadiabatic temperature variation.

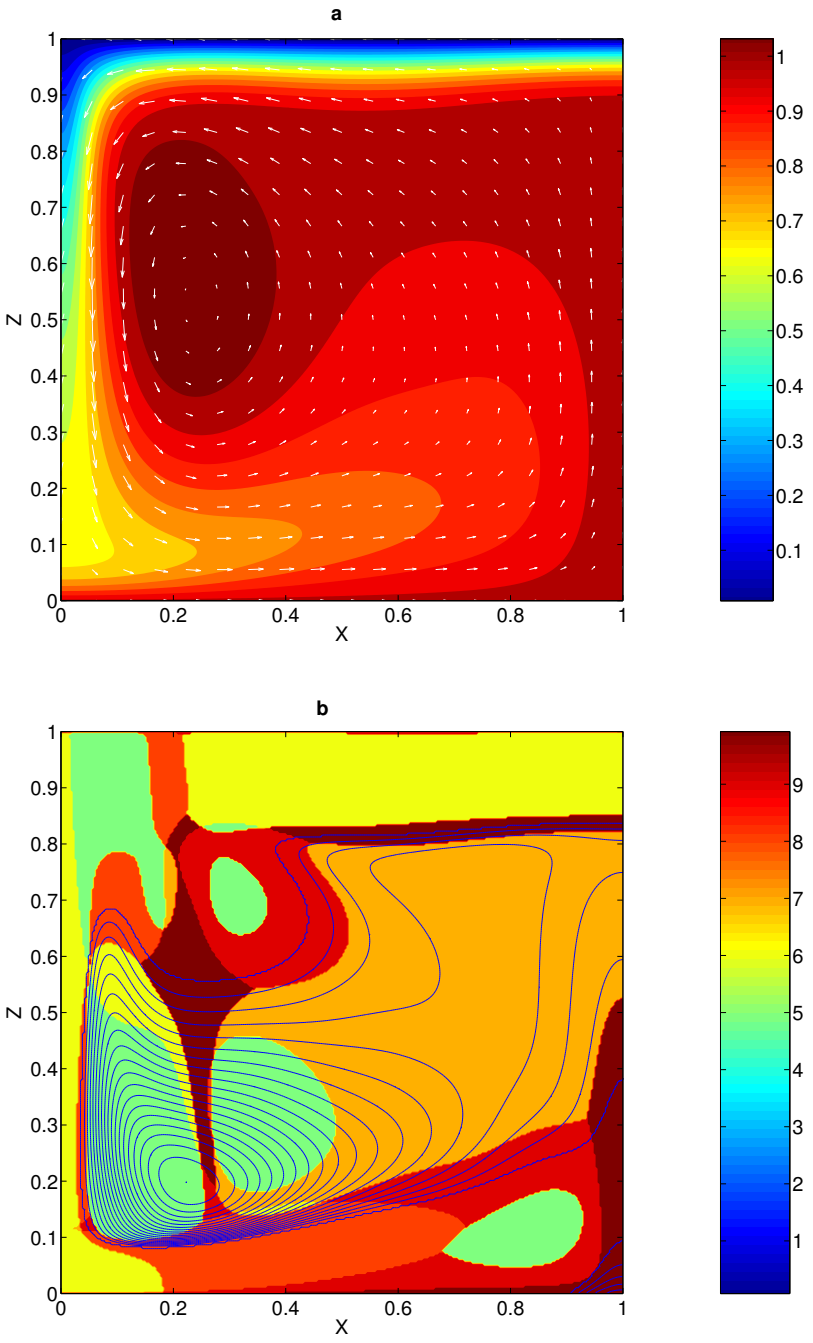

Figure 2.5: Results from calculation Ra5H10v1a1 with $Ra = 10^5$ and $H = 10$: The temperature field together with velocity vector arrows a) and balance in the different terms of the energy equation together with the positive part of the vertical temperature gradient b) (Colorbar: 1 - local secular cooling and vertical advection, 2 - local secular cooling and horizontal advection, 3 - local secular cooling and conduction, 4 - local secular cooling and internal heating, 5 - vertical and horizontal advection or VA-HA, 6 - vertical advection and conduction, 7 - vertical advection and internal heating or VA-H, 8 - horizontal advection and conduction, 9 - horizontal advection and internal heating, 10 - conduction and internal heating). Here 1, 2, 3 and 4 all together in the colorbar is the balance mechanism SC and due to the steady state of the model, SC is not present in this plot.

In order to elucidate the origin of the symmetric temperature overshoots in a purely basally heated model, I examine fig. 2.6, where fig. 2.6a and 2.6b are the temperature field and the geotherm for a calculation with $Ra = 10^6$ and $H = 0$ (model Ra6H0v1a1 in table 2.1). The filled contour plot in fig. 2.6c shows the area with positive vertical temperature gradient (similar to fig. 2.5b) with an overlain arrow plot of the velocity field. The overshoots in the geotherm (fig. 2.5b) are associated with the regions of strong positive vertical temperature gradient that occur in long thin, almost horizontal strips (fig. 2.5c) just above the lower and below the upper thermal boundary layers and adjacent to the rising and sinking plumes (fig. 2.5a). In fig. 2.6d, I plot the terms in the energy equation for vertical advection, $-\mathrm{v}\partial\mathrm{T}/\partial\mathrm{z}$, horizontal advection, $-\mathrm{u}\partial\mathrm{T}/\partial\mathrm{x}$, and diffusion, $\nabla^2\mathrm{T}$ along a line, which is shown in purple in fig. 2.6c. It can be seen that in the overshoot regions the dominant balance in the energy equation is between vertical and horizontal advection as was previously explained by Jarvis and Peltier (1982). The data in table 2.2 also show that regions where the two different advection terms are balancing each other (VA-HA), account for 72% of the subadiabatic gradient.

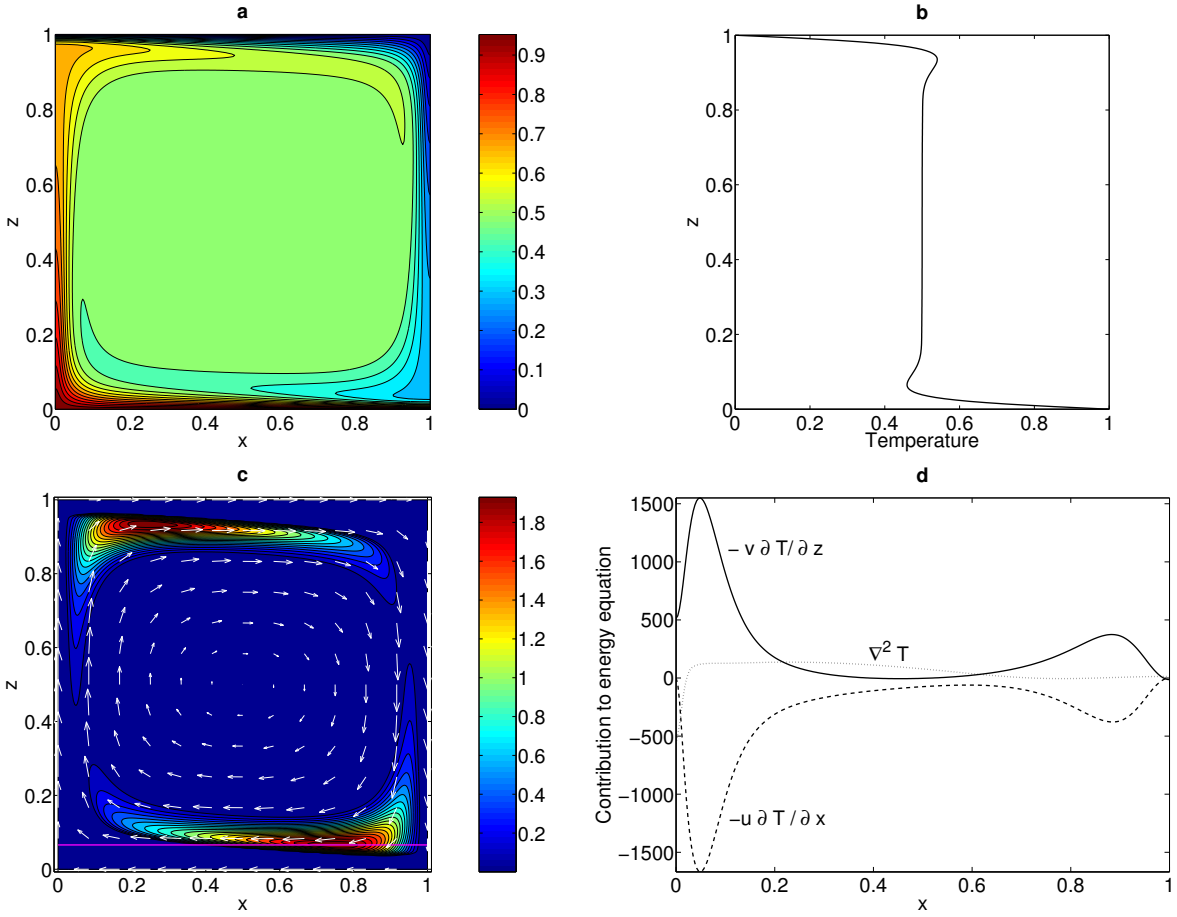

Figure 2.6: Results from the calculation Ra6H0v1a1 with $Ra = 10^6$ and $H = 0$: a) The temperature field, b) the horizontally-averaged vertical temperature profile, c) the positive part of the vertical temperature gradient and d) the vertical advection (solid line), horizontal advection (dashed line) and diffusion term (dotted line) along the purple line shown in c.

In fig. 2.7a, 2.7b and 2.7c, I show time-averaged geotherms calculated from simulations with $Ra = 10^5$ (Ra5H0v1a1, Ra5H2.5v1a1, Ra5H5v1a1, Ra5H7.5v1a1 and Ra5H10v1a1) and 10^7 (Ra7H0v1a1, Ra7H10v1a1, Ra7H20v1a1, Ra7H30v1a1, Ra7H40v1a1, Ra7H50v1a1 and Ra7H60v1a1) in 1×1 boxes and $Ra = 10^6$ (Ra6H0v1a4, Ra6H3v1a4, Ra6H10v1a4, Ra6H18v1a4, Ra6H27v1a4 and Ra6H36v1a4) in 4×1 boxes, respectively, with different degrees of internal heating. The time-averaged geotherms for $Ra = 10^5$ with different H in 4×1 boxes looked very similar to the ones in 1×1 boxes. Due to the mechanism described in the previous paragraph, as the degree of internal heating is increased, the surface overshoot decreases in magnitude and then disappears as the lower overshoot increases. It can also be seen that at $Ra = 10^7$ the geotherm, interior to the overshoot and top thermal boundary, is close to adiabatic for values of H up to roughly 20 whereupon VA-H and SC mechanisms start to cause significantly subadiabatic interior gradients. This phenomenon can be observed for calculations with values of $H = 10$ and higher when $Ra = 10^6$. VA-HA makes up a decreasing fraction of the subadiabatic gradient in the models as internal heating is increased. This phenomenon can be seen in table 2.2 for the set of calculations with $Ra = 10^5$ and increasing H (Ra5H0v1a1, Ra5H2.5v1a1, Ra5H5v1a1, Ra5H7.5v1a1 and Ra5H10v1a1), where the value for VA-HA decreases from 71% to 44% and VA-H increases from 0 to 40% as the amount of internal heating is increased. Also, the scaled value of T_{sub} increases from 296 K to 592 K, assuming a temperature drop $\Delta T = 3700$ K (Boehler, 2000). The models with $Ra = 10^6$ show time-dependence, indicated by the higher values of SC, but overall, the percentage of the total subadiabatic gradient due to mechanism VA-HA decreases with increasing H while VA-H increases. All of the models for $Ra = 10^7$ (Ra7H0v1a1, Ra7H10v1a1, Ra7H20v1a1, Ra7H30v1a1, Ra7H40v1a1, Ra7H50v1a1 and Ra7H60v1a1) are strongly time-dependent and as a result, the most significant energy balance is due to mechanism SC. Mechanisms VA-H and VA-HA show similar trends as those seen for lower Rayleigh number calculations, but these are not as clear due to the dominance of SC. For higher Rayleigh numbers or when the calculation is time-dependent, SC acts very much like VA-H and VA-HA, concealing their effects.

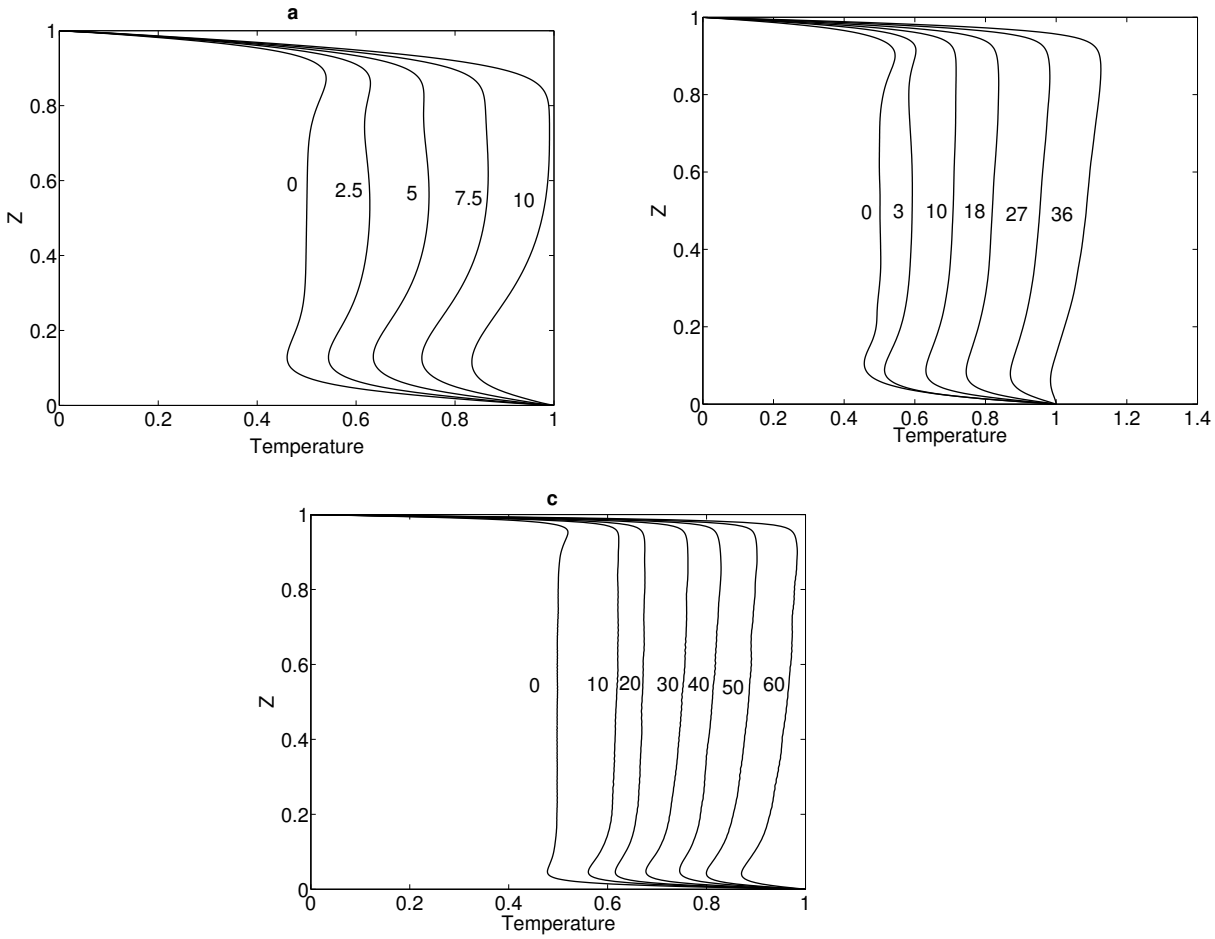

Figure 2.7: Time-averaged geotherms from the calculations a) Ra5H0v1a1, Ra5H2.5v1a1, Ra5H5v1a1, Ra5H7.5v1a1, and Ra5H10v1a1 with $Ra = 10^5$ and $H = 0$, 2.5, 5, 7.5 and 10, respectively, in 1×1 boxes; b) Ra6H0v1a4, Ra6H3v1a4, Ra6H10v1a4, Ra6H18v1a4, Ra6H27v1a4 and Ra6H36v1a4 with $Ra = 10^6$ and $H = 0$, 3, 10, 18, 27 and 36, respectively, in 4×1 boxes; c) Ra7H0v1a1, Ra7H10v1a1, Ra7H20v1a1, Ra7H30v1a1, Ra7H40v1a1, Ra7H50v1a1 and Ra7H60v1a1 with $Ra = 10^7$ and $H = 0$, 10, 20, 30, 40, 50 and 60, respectively, in 1×1 boxes.

Fig. 2.8a and 2.8b show the temperature snapshot and the energy balance plot corresponding to the same time instant, for a Rayleigh number of 10^6 and $H = 3$ (Ra6H3v1a4). Similar plots can be seen in fig. 2.8c and d for $H = 36$ (Ra6H36v1a4). The blue color in the balance plots indicates time dependence (SC). In table 2.2, the time-averaged value for mechanism SC shows that it is responsible for 60% and 55% of the subadiabatic gradient for calculations Ra6H3v1a4 and Ra6H36v1a4, while VA-HA accounts for 35% and 20%, and corresponds to the green color near the core-mantle boundary, in the regions of high subadiabaticity. Mechanism VA-HA can also be seen just below the top thermal boundary layer, but as the effective internal heating rate is reasonably high, it is much weaker than that at the bottom and does not produce a top overshoot in the geotherm (see fig. 2.7b). VA-H (shown as orange in the balance plots) is almost insignificant in Ra6H3v1a4 because of the low internal heating, but it accounts for 16% of the subadiabatic gradient in model Ra6H36v1a4, which is almost entirely internally heated. As can be seen in the figure, VA-H is most prevalent in the regions of broad upwelling. I have not shown similar plots for calculations with $Ra = 10^7$ or 10^8 because the complex, short wavelength patterns make these plots very difficult to interpret visually.

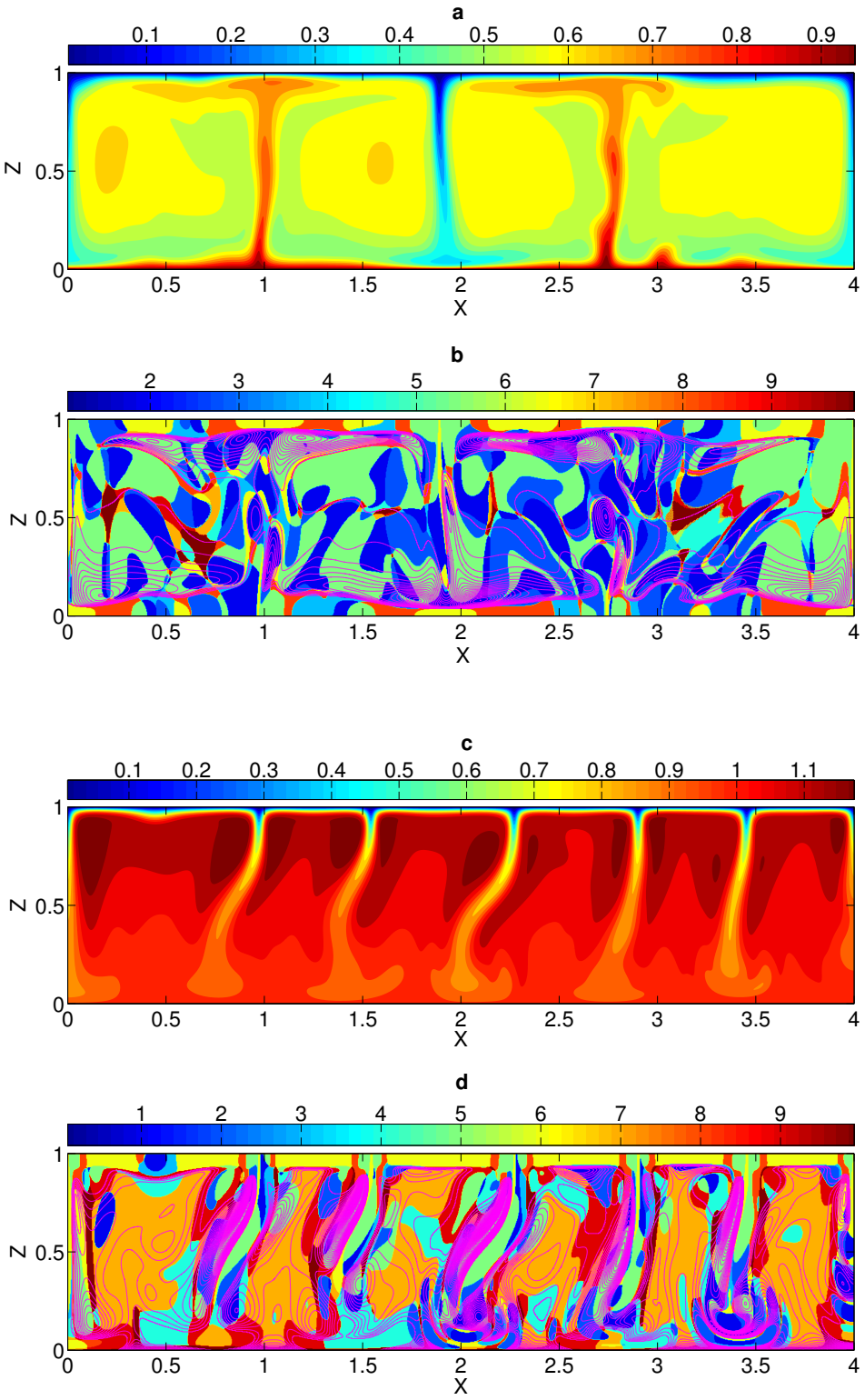

Figure 2.8: Temperature field a) and corresponding energy balance plot overlain by the contour lines of the positive part of the vertical temperature gradient b) for calculation with $Ra = 10^6$ and $H = 3$ (Ra6H3v1a4); c) and d) are similar plots for $H = 36$ (Ra6H36v1a4).

Fig. 2.9a and 2.9b show the magnitude of the subadiabatic temperature drop, T_{sub}, and the area of the domain with positive temperature gradient, A_{sub}, with increasing Urey ratio (ratio of the internal heating to the surface heat flux) for calculations with $Ra = 10^5$ (Ra5H0v1a4, Ra5H2.5v1a4, Ra5H5v1a4, Ra5H7.5v1a4 and Ra5H10v1a4) and 10^6 (Ra6H0v1a4, Ra6H3v1a4, Ra6H4.5v1a4, Ra6H10v1a4, Ra6H18v1a4, Ra6H27v1a4 and Ra6H36v1a4) in 4×1 boxes, and 10^7 (Ra7H0v1a1, Ra7H10v1a1, Ra7H20v1a1, Ra7H30v1a1, Ra7H40v1a1, Ra7H50v1a1 and Ra7H60v1a1) in 1×1 boxes. T_{sub} clearly increases with increasing Urey ratio and decreases as the Rayleigh number is increased, however, no scaling could be found. As can be seen in fig. 2.9, models with $Ra = 10^5$, 10^6 and 10^7 have values of A_{sub} close to 50% up to a Urey ratio of roughly 60% whereupon A_{sub} increases suddenly.

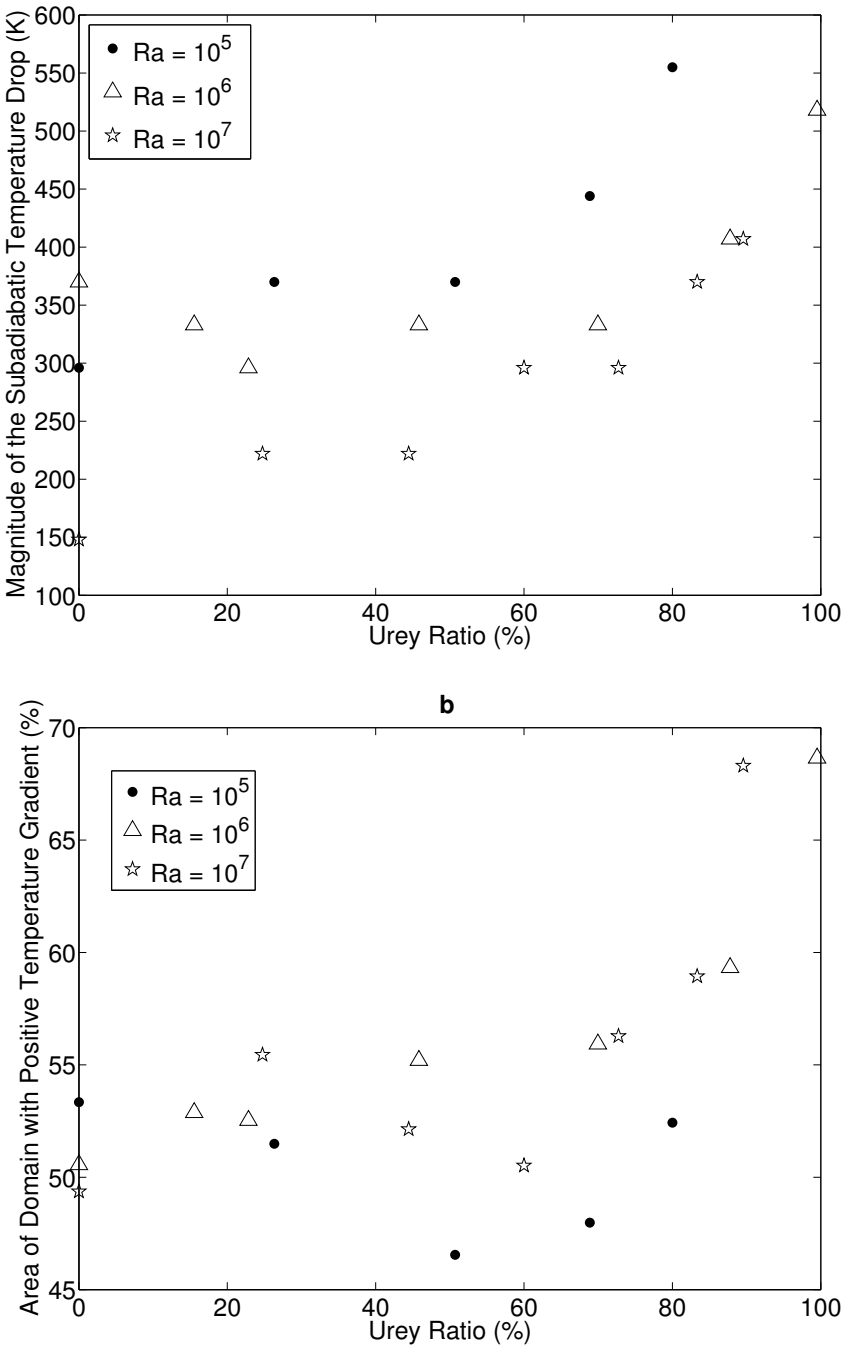

Figure 2.9: Magnitude of the total subadiabatic temperature drop a) and area of domain with a positive temperature gradient b) as a function of the Urey Ratio for $Ra = 10^5$ and 10^6 in a 4×1 box and $Ra = 10^7$ in a 1×1 box.

2.6.1 The Effects of Depth-dependent Viscosity

I ran simulations with a surface Rayleigh number of $Ra = 10^6$ with $H = 0$ and 10 and specified total increases of $\mu_j = 10$ and 100 in viscosity (Ra6H0v100a1, Ra6H0v10a1, Ra6H10v100a1 and Ra6H10v10a1). Due to the very low convective vigor when I use $\mu_j = 100$ and $H = 0$ (Ra6H0v100a1) the interior of the geotherm was subadiabatic (not shown). Jarvis and Peltier (1982) showed in their basally-heated constant-viscosity calculations that the geotherm is subadiabatic for Rayleigh numbers between 5 to almost 100 times the critical value. My analysis shows that the subadiabaticity in these cases is caused by mechanism VA-HA. I ran another set of models with increased surface Rayleigh numbers such that the surface heat flux was close to the same for the models with depth-dependent and constant viscosity in order to be able to compare models with the same effective Rayleigh number.

Fig. 2.10 shows the time-averaged geotherms from models with different viscosity jumps and the same effective Rayleigh numbers for $H = 0$ (Raeff6H0v100a1, Raeff6H0v10a1 and Ra6H0v1a1). The average temperature decreases as I increase the total viscosity jump, because a larger temperature drop is required at the core-mantle boundary to balance the surface heat flux when the basal thermal boundary layer becomes thicker due to the increased viscosity (Butler and Peltier, 2000). The magnitudes of the top and bottom overshoots do not change, however, the surface overshoot becomes narrower while the bottom overshoot becomes broader because of the difference in mobility of the mantle material as the total jump in viscosity is increased. The interior of the geotherms is adiabatic in all cases.

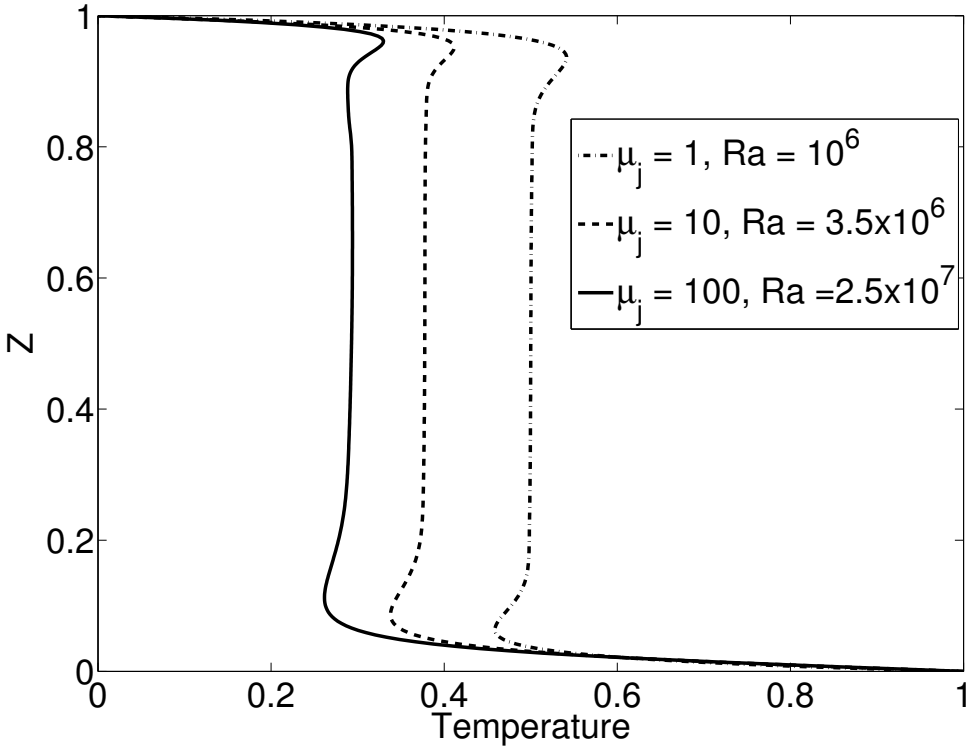

Figure 2.10: Geotherms from calculations Raeff6H0v100a1, Raeff6H0v10a1 and Ra6H0v1a1 with no internal heating and viscosity jumps of $\mu_j = 1$, 10 and 100, respectively, using the same effective Rayleigh number, which was determined by matching the heat flux of the layered viscosity model with the heat flux of a similar isoviscous calculation.

In fig. 2.11, I plot the time-averaged geotherms from calculations with almost identical effective Rayleigh numbers, $H = 10$ and viscosity increases of $\mu_j = 1$, 10 and 100 (Ra6H10v1a1, Raeff6H10v100a1 and Raeff6H10v10a1). Note that as the viscosity jump increases, the surface overshoot reappears and becomes more pronounced while the lower overshoot becomes broader. The reappearance of the surface overshoot in the presence of internal heating is caused by the lower average temperature in the case of depth-dependent viscosity and the greater mobility near the surface. Both of these factors enhance the horizontal advection of heat leading to a surface overshoot due to the mechanism VA-HA. However, if the effective Rayleigh number is kept the same, depth-dependent viscosity does not lead to a significant change in the total subadiabaticity.

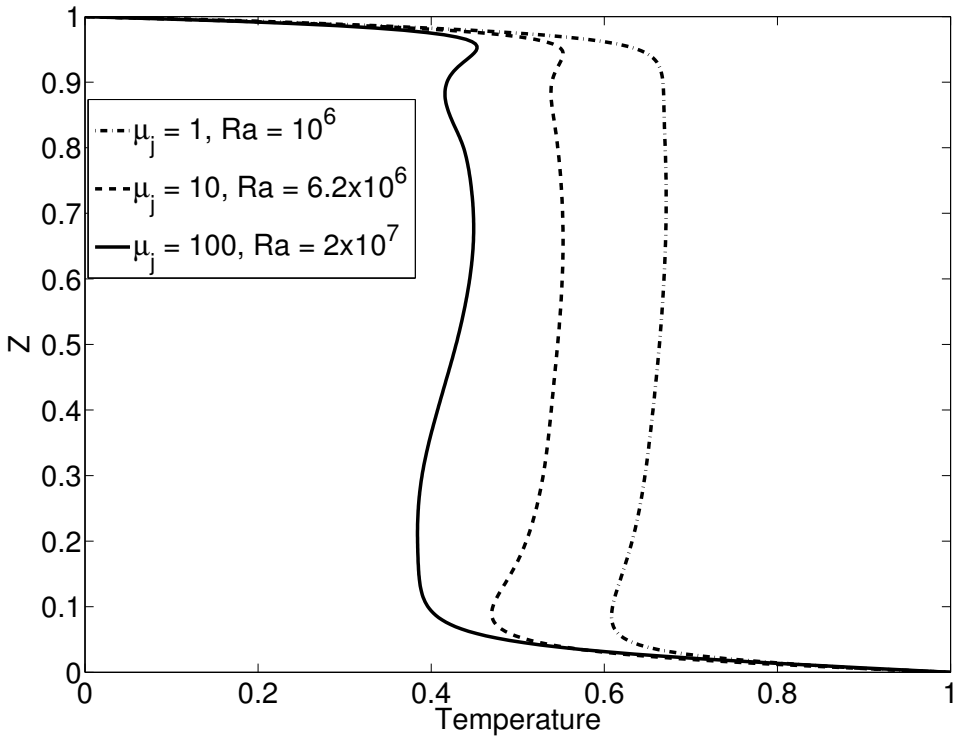

Figure 2.11: Geotherms from calculations Ra6H10v1a1, Raeff6H10v100a1 and Raeff6H10v10a1 with $H = 10$ and viscosity jumps of $\mu_j = 1$, 10 and 100 with depth, respectively, using the same effective Rayleigh number, which was determined by matching the heat flux of the layered viscosity model with the heat flux of a similar isoviscous calculation.

2.6.2 The Effects of Surface Boundary Conditions

Fig. 2.12 shows the geotherms from models with a Rayleigh number of 10^6 and $H = 10$ calculated with different surface boundary conditions including free-slip, no-slip, no-slip with a conducting lid of thickness 0.04 (dimensionally 116 km), as well as models with mixed surface boundary conditions in 1×1 boxes (Ra6H10v1a1, Ra6H10v1L0.3a1$*$, Ra6H10v1L0.4a1$*$, Ra6H10v1L1a1 and Ra6H10v1L1a1$*$). I also conducted similar calculations with the same absolute continent sizes where continents cover the same percentage of the surface area in higher aspect ratio (4 and 8) boxes and the time-averaged geotherms looked almost identical (discussed in the next section). The model with a stagnant-lid on top (e.g. no-slip or no-slip with a conducting lid) may be especially applicable to Venus and Mars (e.g. Reese et al., 1998; Solomatov and Moresi, 1996; Stevenson, 2003). In models where the continental length is 0.4 (Ra6H10v1L0.4a1$*$), the continent is in the middle and for models with continental length 0.3 (Ra6H10v1L0.3a1$*$), it is at the left of the box for unit aspect ratio calculations. In the case when the surface is entirely covered by a conducting lid the mantle transports heat into the core because of its very high internal temperature in a square box, otherwise, all the geotherms show subadiabaticity with an overshoot at the bottom. Note that putting the conducting lid on the left or in the middle of the box does not make much difference as shown by the geotherm plots in fig. 2.12. The values in table 2.2 show that when the surface is changed to no-slip from free-slip in unit aspect ratio models, the subadiabatic contribution due to VA-HA decreases from 62% to 42% and further decreases to only 2% when the entire surface is covered by a conducting lid. On the other hand the total contribution due to the mechanism VA-H increases from 4% to 36% indicating that mechanism VA-H becomes more important when a stagnant lid is in place. Similar trends can also be seen in higher aspect ratio calculations. Although the mechanism causing the subadiabaticity changes, the data in table 2.1 shows that the total magnitude of the subadiabatic temperature drop, T_{sub}, is not significantly affected by the surface boundary condition. In the following section, I discuss the effects due to larger aspect ratio boxes.

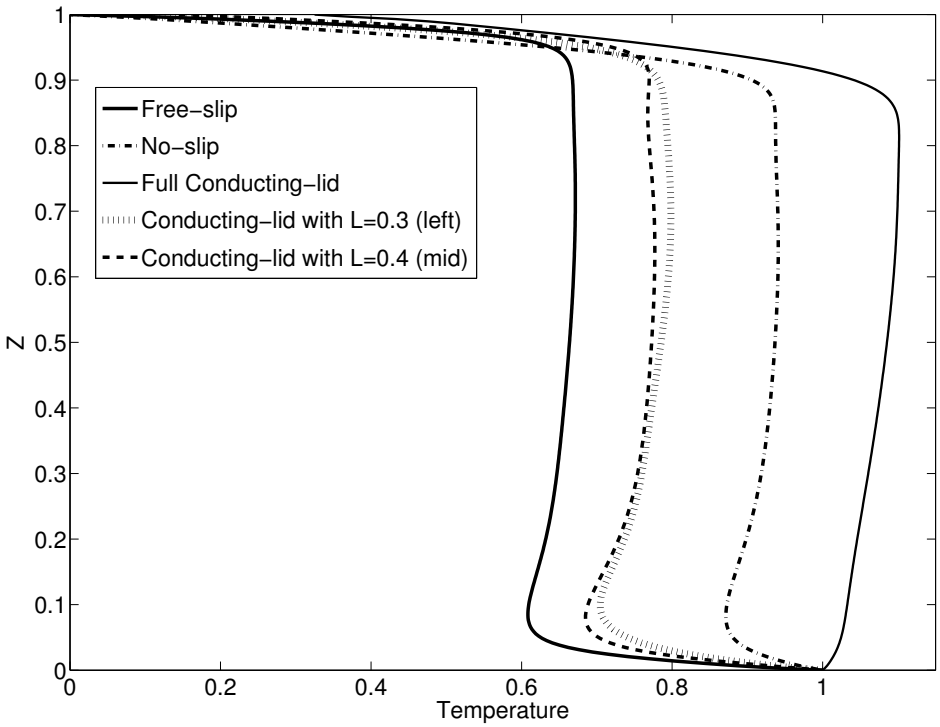

Figure 2.12: Geotherms from the calculations Ra6H10v1a1, Ra6H10v1L0.3a1∗, Ra6H10v1L0.4a1∗, Ra6H10v1L1a1 and Ra6H10v1L1a1∗ with $H = 10$ and different surface boundary conditions for $Ra = 10^6$ in square boxes.

2.6.3 The Effects of Aspect Ratio

In larger aspect ratio boxes, solutions become more time-dependent and as a result, SC becomes increasingly important as a mechanism causing subadiabaticity as can be seen in the results listed in table 2.2. The data in table 2.1 show that in almost all of the models with a free or mixed surface boundary, T_{sub} stays the same or increases slightly as the aspect ratio of the box is increased. When complete or partial free-slip surface boundary conditions are used, wider boxes result in longer wavelength convection cells and enhanced horizontal advection of heat near the lower boundary. Consequently, VA-HA becomes more important causing a greater bottom overshoot and hence, increased subadiabaticity. As an example, I have plotted the geotherms from aspect ratio 8 calculations in fig. 2.13 for different surface boundary conditions. Having a continent in the middle (Ra6H10v1L1.6a4$*$ and Ra6H10v1L3.2a8$*$) made absolutely no difference in the geotherm and hence, I have shown only the geotherm from model where the continent is located on the left side of the box.

If the surface is no-slip or is completely covered by continental lithosphere, the wavelength of the convection cells decreases when the aspect ratio of the box is increased. With this boundary condition, more downwellings occur and they are caused by closely-spaced surface thermal boundary layer instabilities. Because of the shorter wavelength, VA-HA is less significant and hence the total subadiabaticity is decreased. The results from 4×1 and 8×1 boxes were essentially identical, indicating that an aspect ratio of 4 is sufficient to analyze the energy balances causing the subadiabaticity.

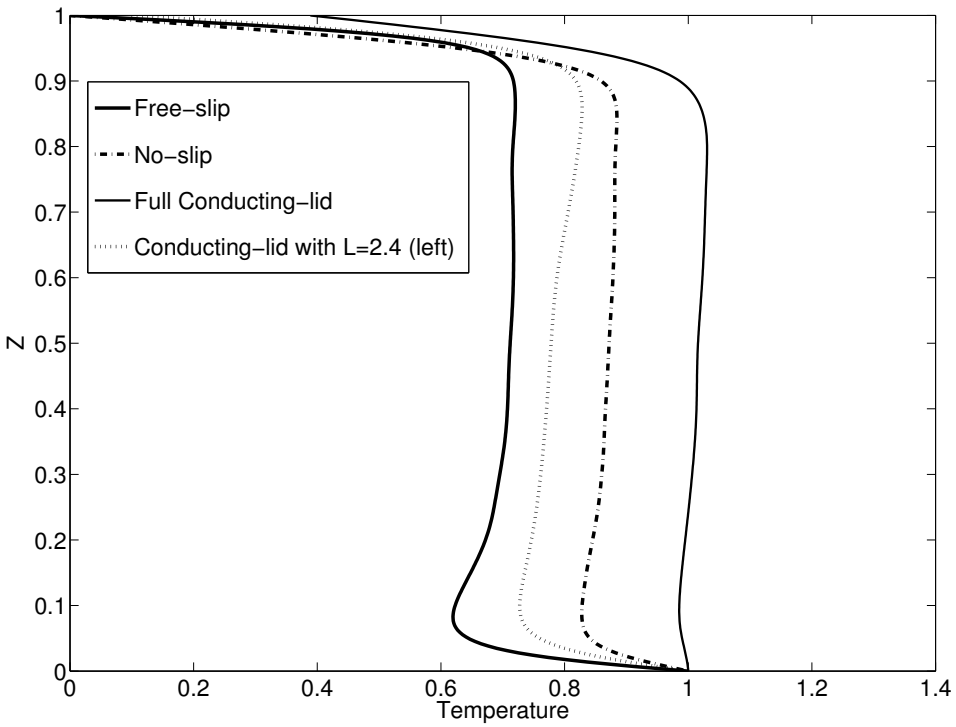

Figure 2.13: Geotherms from the calculations Ra6H10v1a8, Ra6H10v1L2.4a8∗, Ra6H10v1L8a8 and Ra6H10v1L8a8∗ with $H = 10$ and different surface boundary conditions for $Ra = 10^6$ in 8×1 boxes.

2.6.4 The Effects of Subadiabatic Temperature Gradients on Heat Flux at the Core-Mantle Boundary

In fig. 2.14, I present the time-averaged geotherms for calculations carried out with the Rayleigh numbers indicated on the figure and with an internal heating rate of $H = 10$ (Ra5H10v1a1, Ra6H10v1a1, Ra7H10v1a1 and Ra8H10v1a1). As has been pointed out by Sotin and Labrosse (1999) and Butler and Peltier (2000) in calculations with mixed basal and internal heating, the mean internal temperature is a decreasing function of the thermal Rayleigh number for a fixed internal heating rate. Sotin and Labrosse (1999) presented scaling results for the average temperature and for the surface heat flow based on their three-dimensional numerical results and my two-dimensional results are in excellent agreement with their scaling. Of interest is that as the thermal Rayleigh number increases, the surface boundary layer thickness, δ_s, decreases as roughly $Ra^{-1/3}$ while the internal temperature and hence the temperature drop across the surface thermal boundary layer, ΔT_s, decreases. The surface heat flow can be calculated from $Q = \Delta T_s/\delta_s$. As a result, the effects offset one another, but the boundary layer thickness decreases more rapidly leading to an increase in the surface heat flow with increasing thermal Rayleigh number, but the increase is much slower than in the purely basally heated case. At the base of the convecting system, however, the decrease in the average internal temperature increases the temperature drop, ΔT_c, and the basal boundary layer thickness, δ_c, decreases as roughly $Ra^{-1/3}$ so that both effects should lead to an increase in the basal heat flow. In an equilibrium state, however, the heat flow at the base is linked to the heat flow at the surface by $Q_c = Q_s - H$ where Q_c and Q_s represent the total heat flows at the core-mantle boundary and surface, respectively. The effect of the subadiabatic gradient is to increase the temperature drop at the core-mantle boundary and it decreases with increasing thermal Rayleigh number for fixed H as can be seen from the results in table 2.1. As I will show, the decrease in the subadiabaticity allows for the energy balance at the core-mantle boundary.

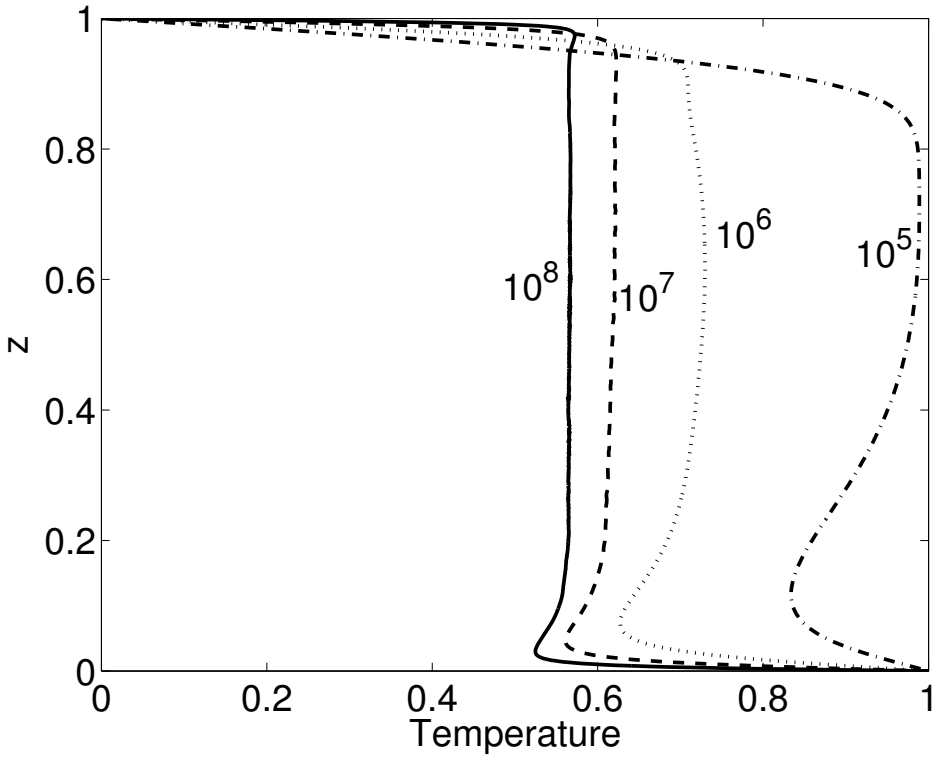

Figure 2.14: Geotherms calculated for simple Boussinesq calculations Ra5H10v1a1, Ra6H10v1a1, Ra7H10v1a1 and Ra8H10v1a1 in 1×1 boxes with $H = 10$ and different thermal Rayleigh numbers.

That the subadiabatic gradient is important can be easily verified by considering the run with $Ra = 10^5$ and $H = 10$ (Ra5H10v1a1) for which there would be practically no temperature drop at the core-mantle boundary in the absence of a subadiabatic gradient while in this case the core-mantle boundary heat flux accounts for roughly 23% of the surface heat flux. The scaling results for the surface heat flux of Sotin and Labrosse (1999) used the average internal temperature, $< T >$, in order to calculate the temperature drop at the surface and this was related to the heat flux at the surface by a relationship roughly of the form $Q_s = (Ra/Ra_{crit})^{1/3} < T >^{4/3}$, as would be expected from boundary layer theory where Ra_{crit} is the critical boundary layer Rayleigh number and can be defined as a parameter which quantifies the heat transport efficiency across the boundary layer (e.g. Butler and Peltier, 2000). In fig. 2.15, I present the surface heat flux $Q_{smeas} = (\partial T/\partial z)|_{z=1}$, calculated from numerical models run with $Ra \geq 10^6$, $H > 0$, constant viscosity and free-slip boundaries, plotted vs $Q_{spred} = (Ra/Ra_{crit})^{1/3}\, T^{4/3}$ for $T = T_{max}$ ('+' signs) and $T =< T >$, (squares). For both $T = T_{max}$ and $T =< T >$, I have chosen Ra_{crit} in order to give the smallest least-squares misfit between the predicted and measured value of Q_s. The values obtained for Ra_{crit} in this way were 23.8 and 28.2, respectively. I have plotted a straight line with a slope of 1 so that the quality of the fit can be easily discerned. It can be seen from the graph that the fit is not qualitatively improved by using T_{max} rather than $< T >$ and quantitatively the average misfit between Q_{smeas} and Q_{spred} is 2.0 for both calculations, again indicating that the difference between $< T >$ and T_{max} is not important when parameterizing the heat flux at the surface.

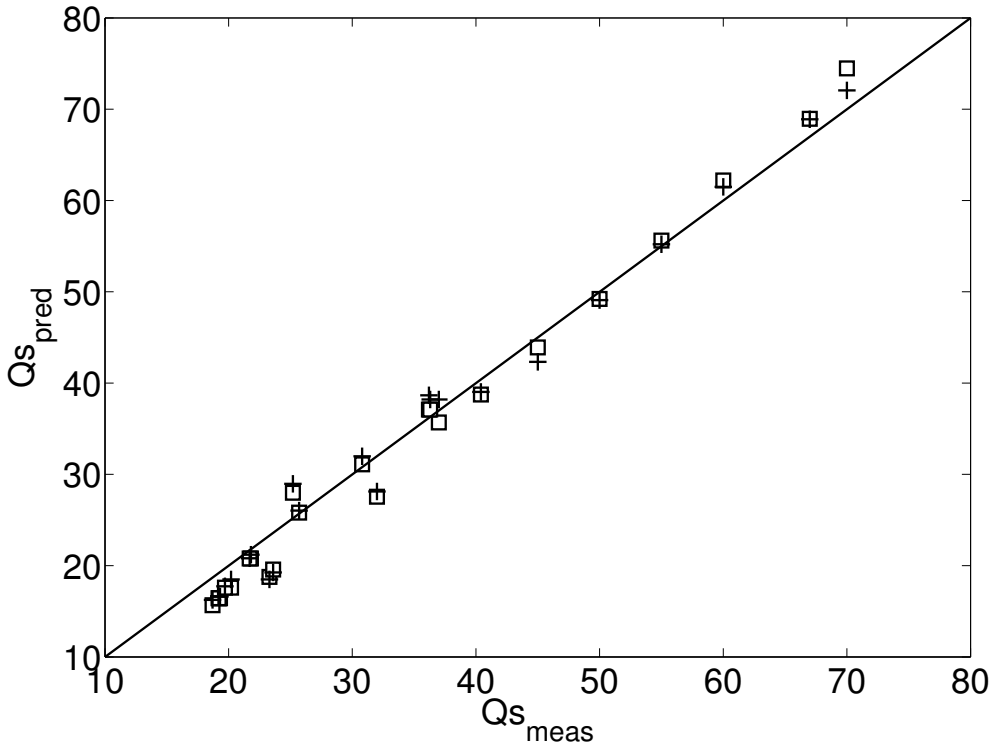

Figure 2.15: Measured surface heat flux vs predicted surface heat flux. '+' are calculated using T_{max} while the squares were calculated using $< T >$.

In fig. 2.16, I present a similar calculation for the basal heat flux, where Q_{cmeas} and Q_{cpred} are the basal heat fluxes calculated by the numerical model and from a parameterized model using temperature from the numerical model. In this case I have calculated the temperature drop at the base using $1 - T$ where T is calculated using $< T >$ (squares) and T_{min}, ('+'s). It can be seen that the fit is now qualitatively improved by using T_{min}, which is the minimum horizontally averaged internal temperature. The average misfits between Q_{cmeas} and Q_{cpred} are 1.1 and 2.1 when T_{min} and $< T >$ are used to calculate the temperature drop at the basal thermal boundary layer, respectively. This indicates that using T_{min} is important in parameterizing the basal heat flux and that the effects of the subadiabatic gradient are important and act to increase the heat flux at the base of a convecting system with mixed basal and internal heating.

Although the degree of subadiabaticity clearly increases with H and decreases with Ra, as shown in fig. 2.9, no simple scaling relationship for the subadiabatic gradient could be found based on the results of my study. As a result, the best way to calculate thermal evolution in parameterized models, taking the mantle subadiabatic gradient into account, might be to calculate the surface heat flux, internal temperature and secular cooling first and then calculate the core-mantle boundary heat flux based on the energy balance as proposed by Sotin and Labrosse (1999).

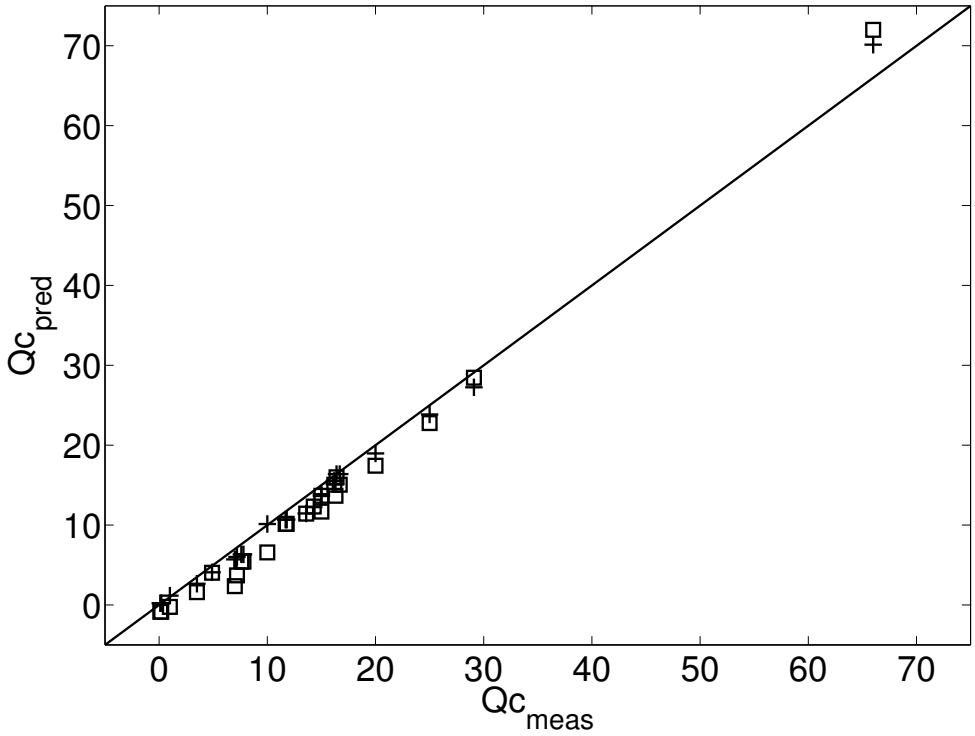

Figure 2.16: Measured basal heat flux vs predicted surface heat flux. '+'s, and squares are calculated using T_{min}, and $< T >$ respectively.

2.7 Conclusion

I have presented a detailed study of the energy balance in regions of subadiabatic gradient for calculations with mixed basal and internal heating. Until now the subadiabatic gradient in an internally heated calculation was thought to be caused by the balance between vertical advection and internal heating. However, my study shows that there are three different mechanisms responsible for the subadiabaticity. I find that VA-HA (balance between horizontal and vertical advection) is significant for calculations with lower degrees of internal heating, whereas VA-H (balance between vertical advection and internal heating) becomes increasingly important with increasing internal heating. Mechanism SC (balance between local secular cooling and the other terms in the energy equation) can play the role of either VA-H or VA-HA in a temporally averaged geotherm. When the model is not time-dependent, VA-H is mostly responsible for the subadiabaticity within the bulk of the mantle, whereas VA-HA mostly produces the bottom geotherm overshoot. My results suggest that the bottom overshoot makes the largest contribution to the subadiabaticity for values of H smaller than roughly Q_{s0}, where Q_{s0} is the surface heat flux from calculations using the same Rayleigh numbers in the absence of internal heating. The total subadiabaticity and the area with a subadiabatic gradient increase with increasing Urey ratio.

The present entirely basally heated models with depth-dependent viscosity show that when a constant effective Rayleigh number (determined by matching the heat flux of the layered viscosity model with the heat flux of a similar isoviscous calculation) is used, the surface overshoot becomes narrower while the bottom overshoot becomes broader with an increased jump in viscosity. In the case of mixed heating models, the surface overshoot reappears as I increase the total jump in viscosity. The surface overshoot may be responsible for the presence of the seismic low velocity zone (Dziewonski and Anderson, 1981).

In the case of mixed surface boundary conditions, the shape of the geotherm does not depend on the position of the continent, however, the presence of a rigid conducting lid increases the subadiabatic gradient in the bulk, implying that Mars and Venus may have significantly subadiabatic interiors.

If I consider an Earth-like surface heat flux, then calculations Ra6H18v1a1 to Ra6H27v1a4 are most comparable to our planet, and have Urey ratios of 72% to 87%. This suggests that the mantle subadiabaticity may be as large as 450 K and 55% to 60% of the volume of the mantle may have a subadiabatic temperature gradient. Here I am taking the effective internal heating rate for the Earth to be the sum of the secular cooling and actual internal heating. In these calculations all three balance mechanisms are active.

I have shown that the effects of subadiabaticity are important for parameterizing the core-mantle boundary heat flux. As an example, if I consider Ra6H10v1L2.4a8$*$, as Earth-like, this suggests a

mantle subadiabaticity of $T_{sub} = 407\,\mathrm{K}$. This would change the total core-mantle boundary heat flux by 3.8 TW, if I assume a core-mantle boundary layer thickness equal to the average thickness of the D" layer, which is 260 km (Kendall and Shearer, 1994) and a thermal conductivity of 16 W/mK (Brown, 1986).

I have identified and quantified the various effects by which subadiabaticity is produced in simple models of internally heated infinite Prandtl number convection. In future work, it will be interesting to explore the effects of compressibility, temperature-dependent viscosity, sphericity (e.g. Bunge et al., 1997) and a better representation of surface plates and how these affect the mechanisms, that I have identified here, responsible for the subadiabatic gradients. In chapter 6, I discuss the inadequacies of the model presented here.

Chapter 3

Is there a difference Between the Effect of Secular Cooling and Internal Heating Rate in Unit Aspect Ratio Calculations?

3.1 Introduction

The non-dimensional equation for the conservation of energy (similar to 2.11) can be written as

$$\frac{\partial T}{\partial t} + \mathbf{U} \cdot \nabla T = \frac{1}{Ra} \nabla^2 T + H, \tag{3.1}$$

where the temporal rate of change of temperature or the first term on the left hand side of the equation is called the secular cooling term and H is the internal heating rate. The other variables have been defined previously. The secular cooling term can also be stated as the decrease in temperature in the mantle with time. As a result, both $-\partial T/\partial t$ and H are often assumed to have similar effects (e.g. Krishnamurti, 1968a, b; DeLandro-Clarke and Jarvis, 1997). However, the secular cooling term varies in space but H is usually a prescribed constant. The large spatial variation of the secular cooling term, which is associated with the SC mechanism, has been shown and discussed widely in chapter 2. This fundamental difference in physical property combined with the assumption of their possible similar effects is interesting and I investigate it here. DeLandro-Clarke and Jarvis (1997) applied varying horizontal thermal boundary conditions in order to induce secular cooling as is commonly done in analogue experiments (e.g. Krishnamurti 1968b) and they found that the secular cooling and the internal heating have very similar effects. I use fixed surface and CMB temperatures but start with an average temperature that is significantly higher than the statistical equilibrium value.

3.2 Results

In order to perform the test, I ran two models, one with and one without internal heating. The calculations were performed in unit aspect ratio two-dimensional boxes with $Ra = 10^7$. The square box had reflecting vertical and free-slip horizontal boundaries. For the run without the internal

heating effect I chose a temperature profile, which was previously run with some amount of internal heating and was hotter than the equilibrium value of a model run with $H = 0$, as the initial condition. Due to this, when running the model without internal heating, the average temperature was decreasing with time and hence, the secular cooling effect was large and positive. In terms of dimensional time, I ran this model for almost 5 G.y.. The time-series for the average temperature and the surface and the CMB heat fluxes are shown in fig. 3.1 and 3.2. I picked a point (800 M.y. in this case) on the average temperature time-series where the model was cooling down relatively fast and calculated the total amount of secular cooling at that point.

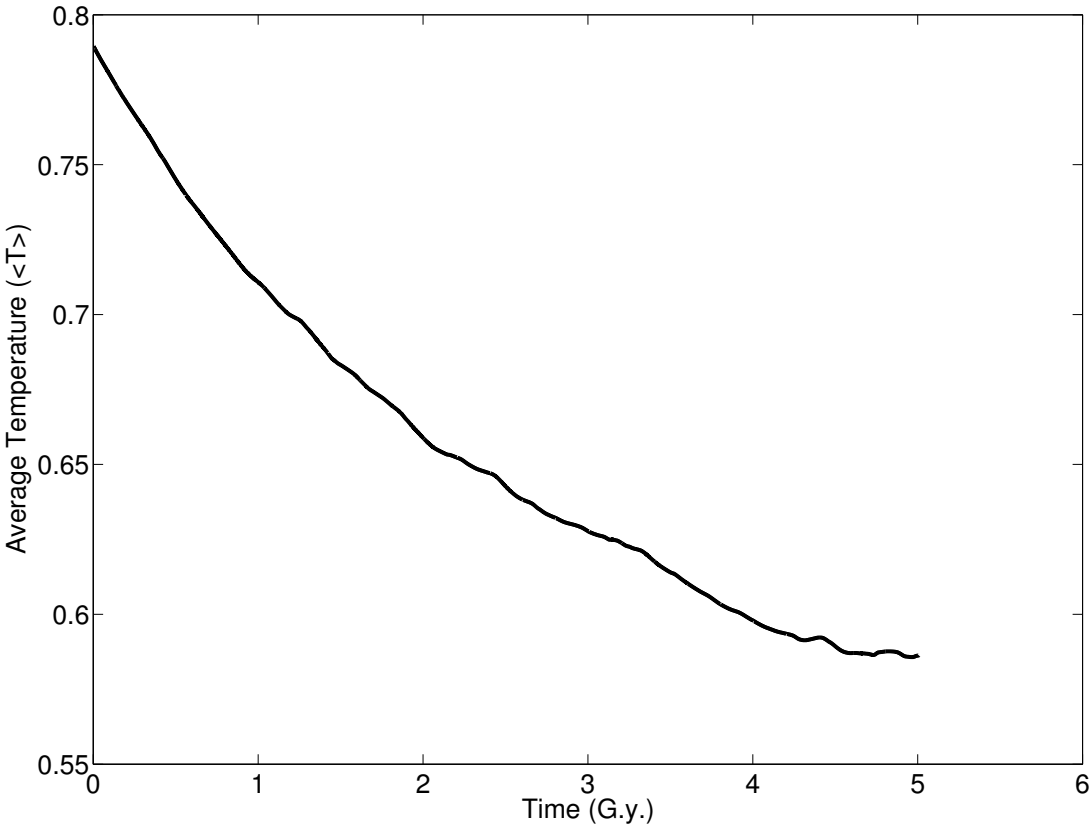

Figure 3.1: Average temperature as a function of time for calculation without internal heating for $Ra = 10^7$.

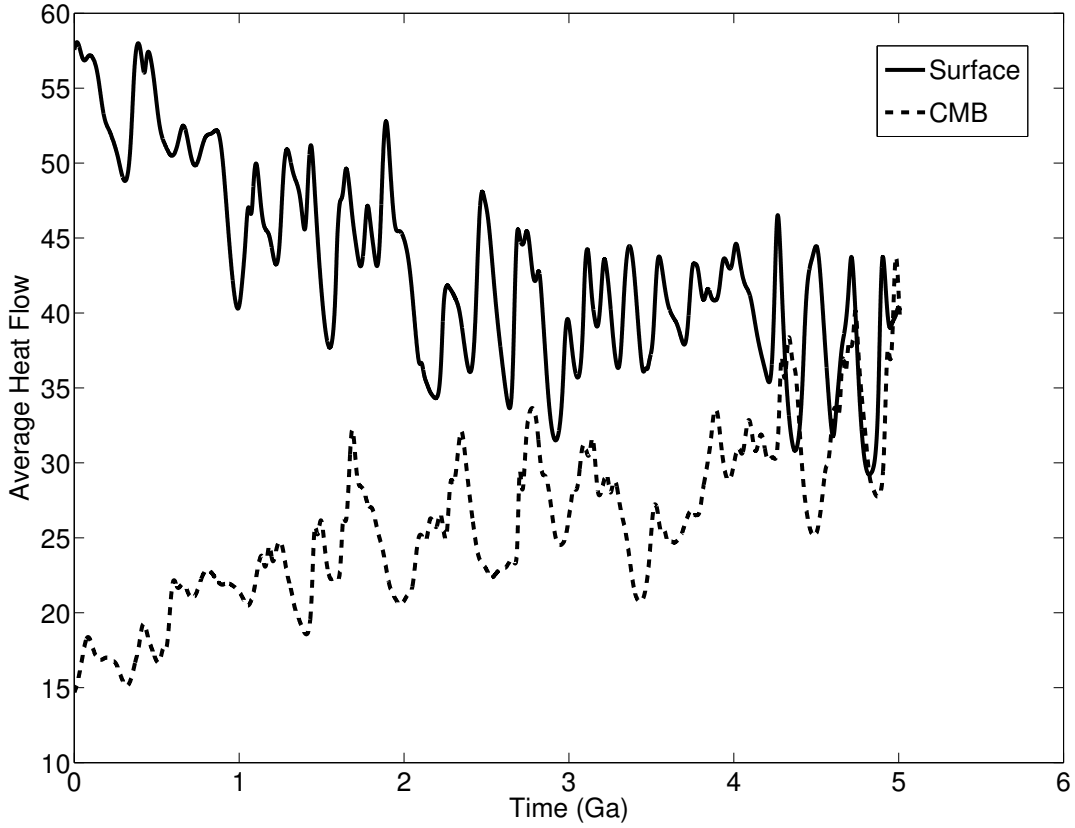

Figure 3.2: Surface and CMB heat fluxes as a function of time for calculation without internal heating for $Ra = 10^7$.

This calculated value of 29.24 for the secular cooling was used as H for the model which included the effect of internal heating. In this case, a convecting temperature profile was chosen from another calculation that was previously run with an amount of internal heating close to $H = 29$ in order to reach an equilibrium state quickly. The model was run for almost 32 G.y. of dimensional time. A set of similar plots for the average temperature and the heat fluxes for the calculation are shown in fig. 3.3 and 3.4.

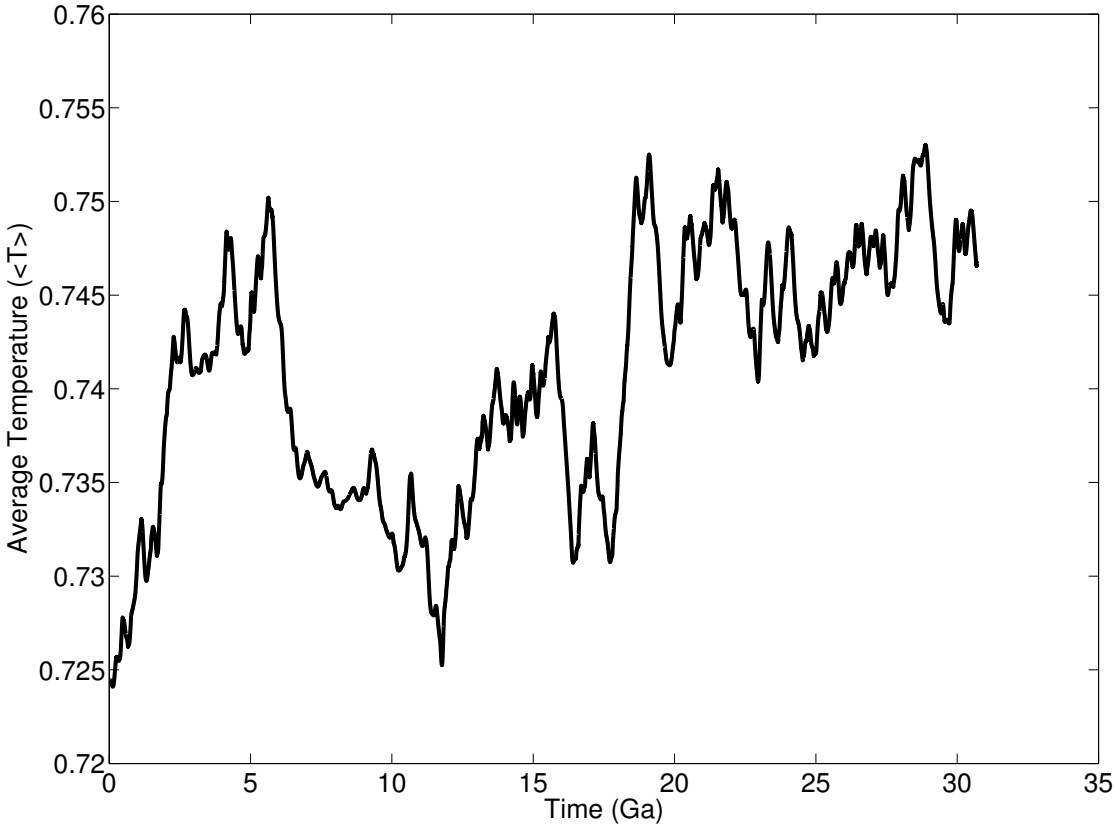

Figure 3.3: Average temperature as a function of time for calculation with internal heating $H = 29.24$ for $Ra = 10^7$.

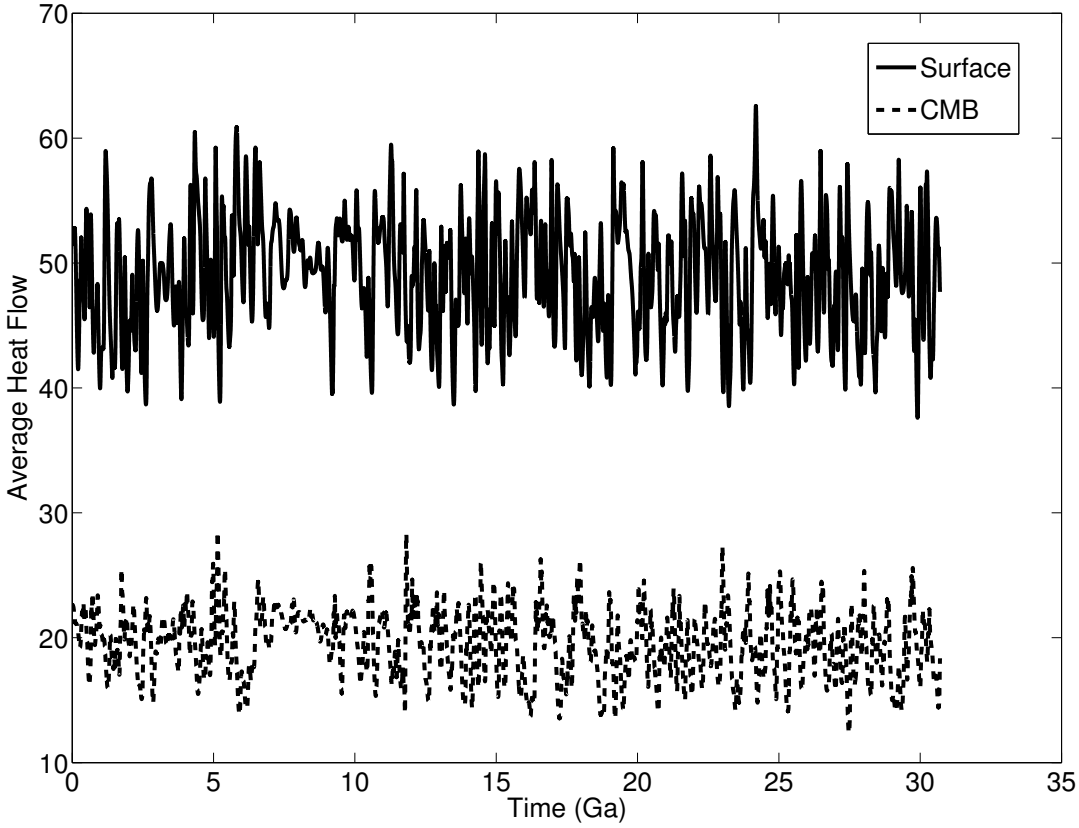

Figure 3.4: Surface and CMB heat fluxes as a function of time for calculation with internal heating $H = 29.24$ for $Ra = 10^7$.

For visual comparison of the results, I picked a time window of 800 M.y. between 800 M.y. and 1.6 G.y.. I chose that window because the average temperature as a function of time plot in fig. 3.1 shows a steep slope indicating a strong secular cooling effect in the model with $H = 0$. I have plotted the time-averaged temperatures and heat fluxes in fig. 3.5, 3.7 and 3.8 from the two calculations with the only difference from the previous figures being that they are focused in the areas within the chosen time window. All figures have been scaled to the same horizontal and vertical resolutions for easy visual comparison. If the overall decrease in temperature for the purely basally heated case in fig. 3.5 is ignored, the short temporal fluctuations are very similar to the result from mixed internally heated case, with periods of roughly 300 M.y. and an amplitude of approximately 0.03. In order to demonstrate this in a better visual representation, I have plotted the residuals from fig. 3.5 in fig. 3.6. The residuals were calculated by taking the difference between the actual curve and a linear fit of the curve for two calculations. This plot shows slightly larger period and amplitude in the presence of internal heating. However, it is not significantly different than the basally heated model. Similarity in the temporal variation is also seen in the heat fluxes, shown by the plots in fig. 3.7 and 3.8.

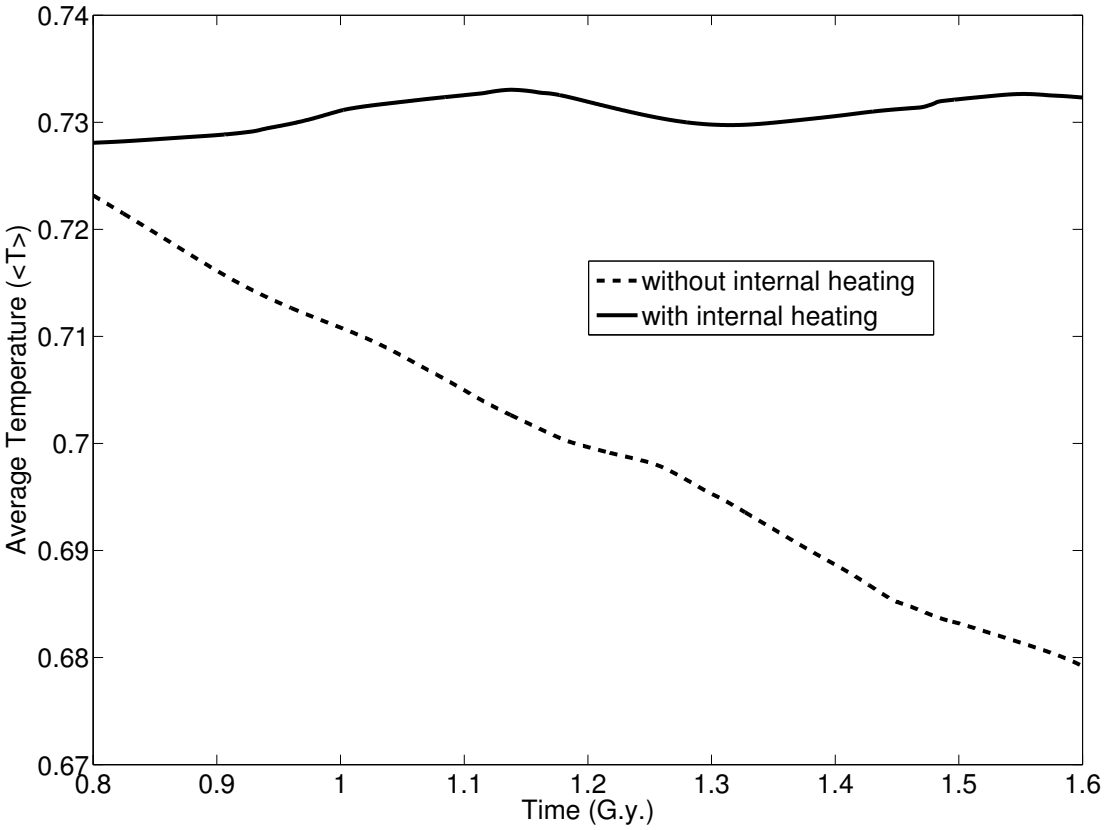

Figure 3.5: Average temperature within a particular time window as a function of time for calculations with and without internal heating for $Ra = 10^7$.

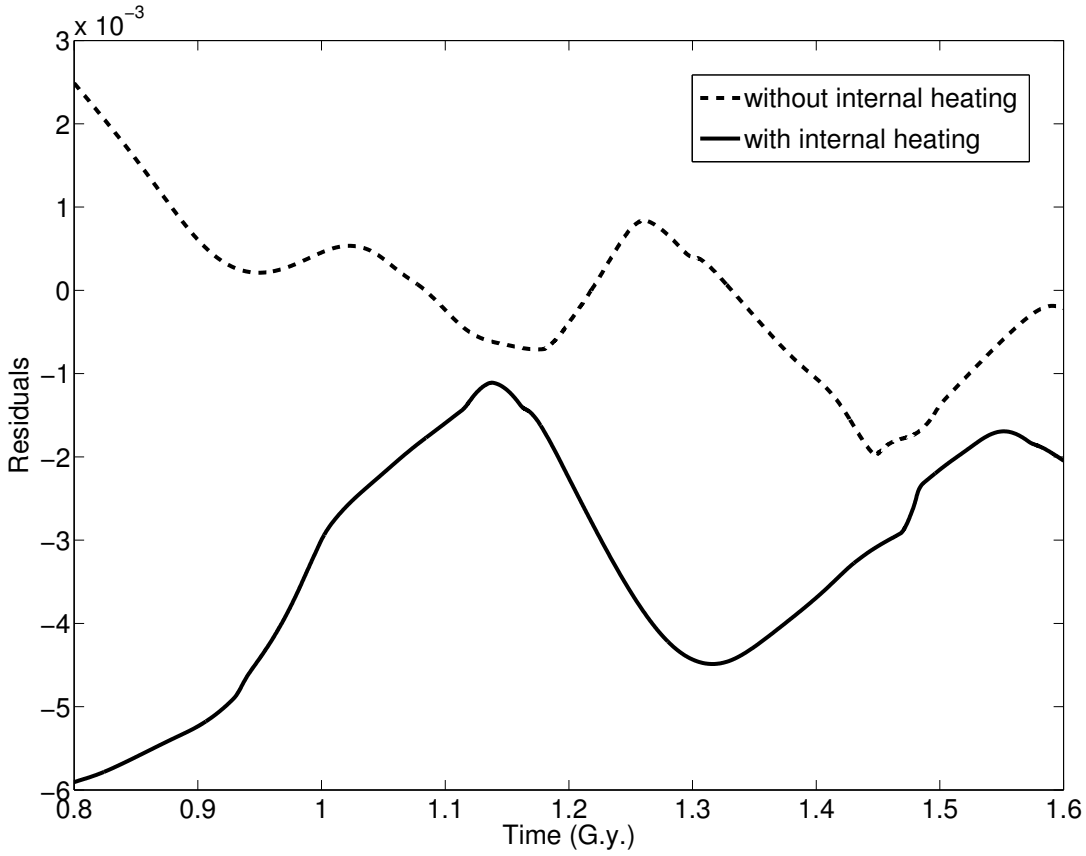

Figure 3.6: Residuals after de-trending the average temperature data within a particular time window as a function of time for calculation with and without internal heating for $Ra = 10^7$.

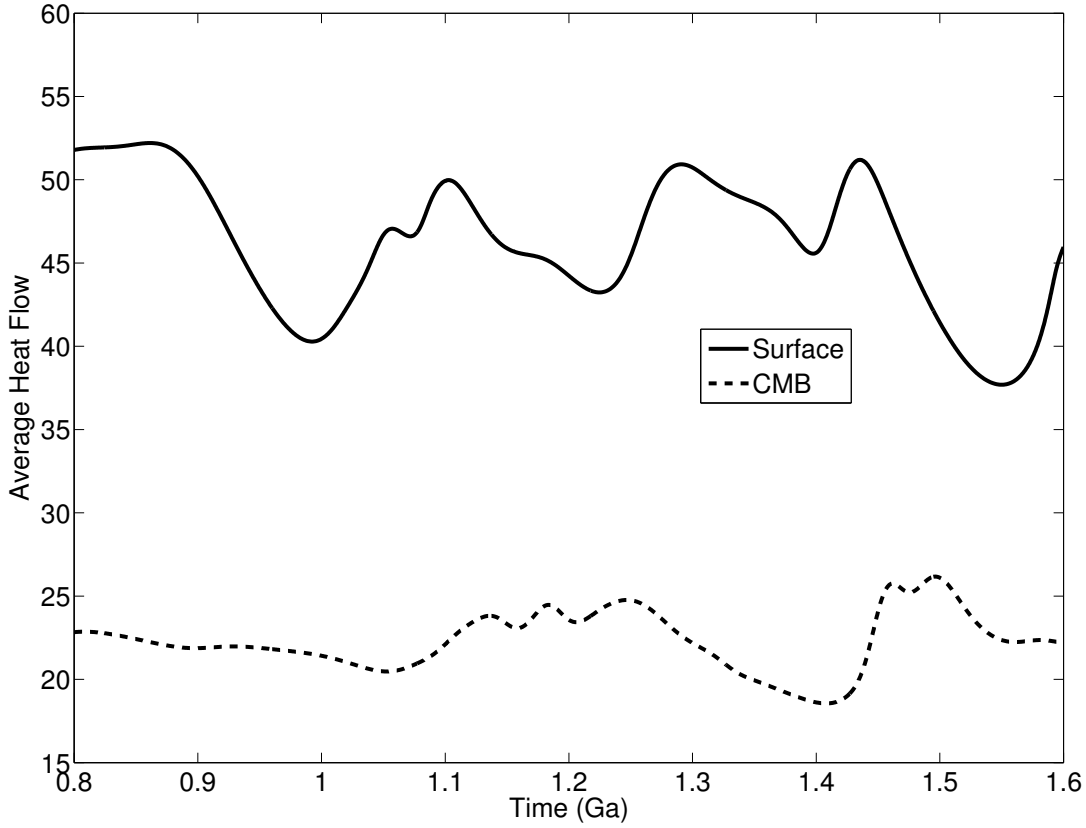

Figure 3.7: Surface and CMB heat fluxes within a particular time window as a function of time for calculation without internal heating for $Ra = 10^7$.

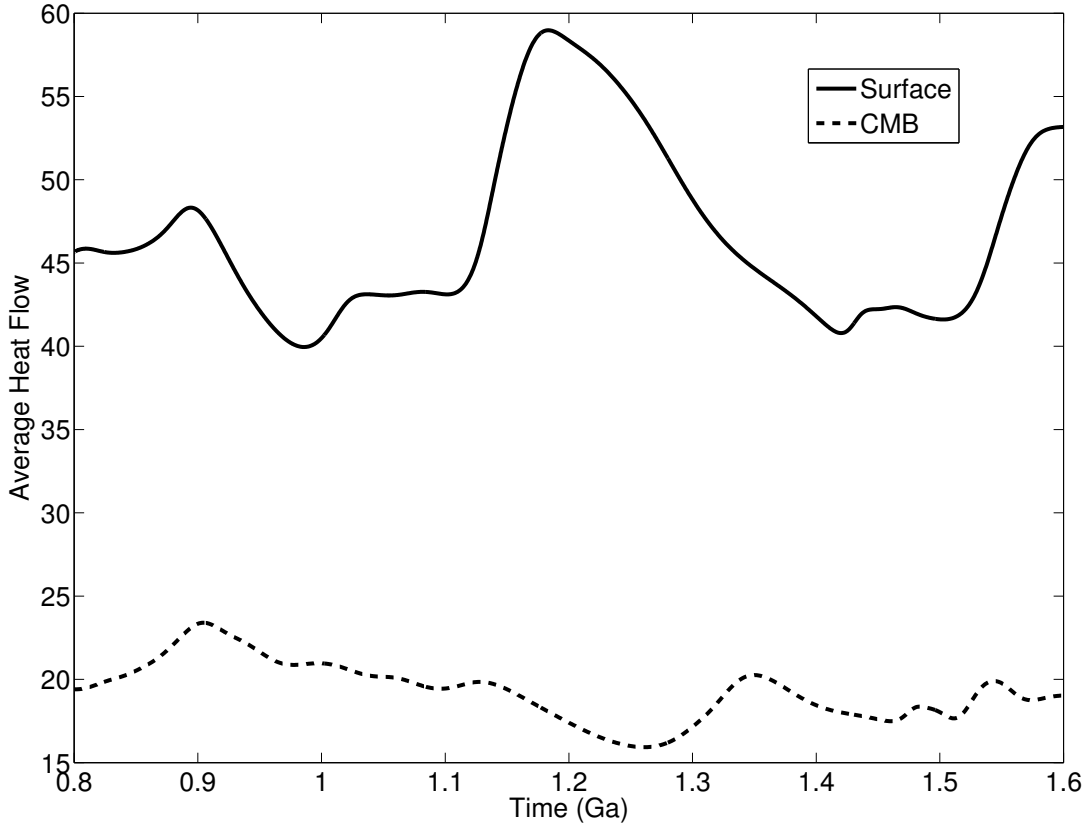

Figure 3.8: Surface and CMB heat fluxes within a particular time window as a function of time for calculation with internal heating for $Ra = 10^7$.

I have also plotted the temporal variation of the total secular cooling term for the two models in fig. 3.9 within the same time window and the observed pattern is again very similar. I multiply the the non-dimensional value of secular cooling by Ra in order to scale the equivalent non-dimensional internal heating rate. Note that the time-averaged secular cooling is close to zero in the case of internally heated model, whereas, it is not zero for the calculation without internal heating since the model is cooling.

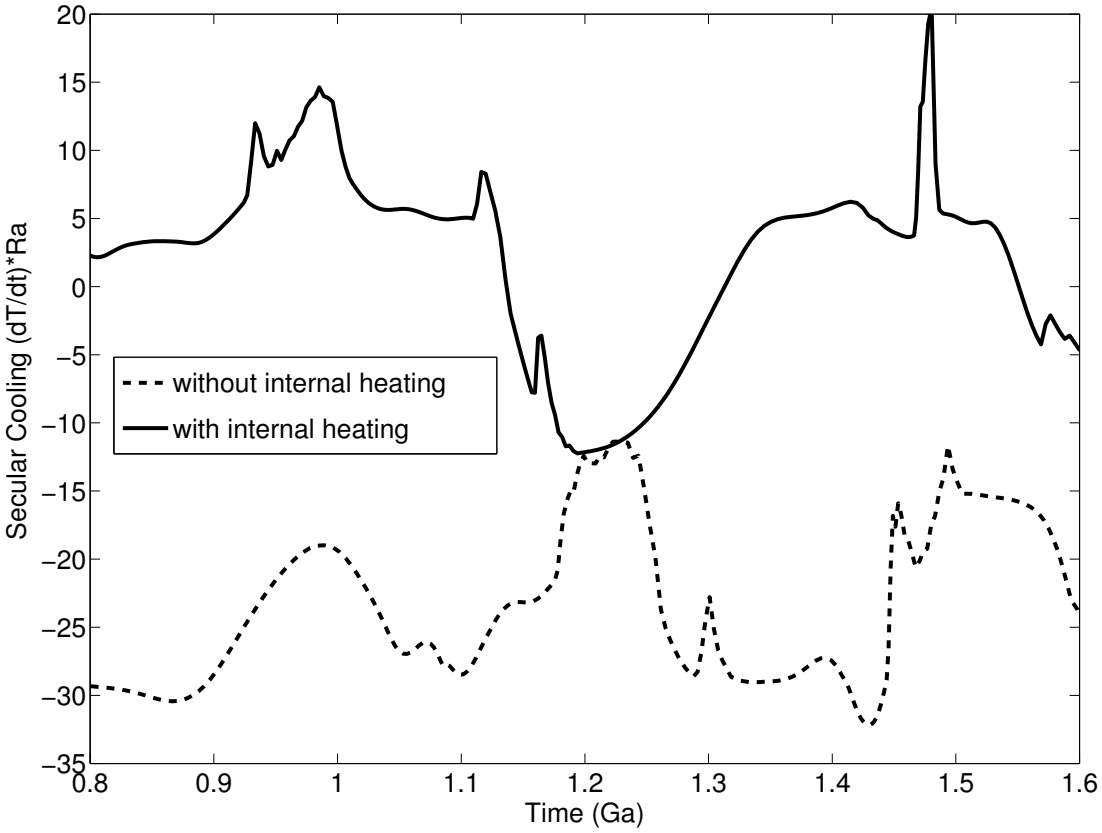

Figure 3.9: Secular cooling as a function of time for calculation with and without internal heating for $Ra = 10^7$.

3.3 Conclusion

It can be said that after visually comparing these results, there is no obvious statistical difference between the calculations with and without internal heating. The spatial evolution of the secular cooling term (not shown here) was not significantly different either. This lead me to stop any further investigation and indicated that for a two-dimensional, unit aspect ratio box with reflecting vertical and horizontal boundaries, the effects from spatially and temporally varying secular cooling and constant internal heating rates are very similar.

Chapter 4

The Combined Effects of Continents and the 660 km-depth Endothermic Phase Boundary on the Thermal Regime in the Mantle

4.1 Introduction

Although both the effects of layering, caused by the spinel to perovskite and magnesiowüstite phase change at 660 km-depth, and continents have been widely studied separately, their combined effects on mantle dynamics have not been investigated previously. Many length scales are involved when modeling thermal convection within the mantle when incorporating continents and the endothermic phase boundary at 660 km-depth. These include the lateral extents (Lenardic and Moresi, 2003) and thicknesses (Lenardic and Moresi, 2001) of the continental lithosphere. In the case of a layered mantle, the depth to the phase boundary can play an important role in the flow dynamics by partially separating the mantle into two different convective regimes and decreasing the surface heat flux. The depth of the mantle is always important and the chosen aspect ratio of the box used for modeling can introduce further length scales.

In a laboratory tank experiment, Guillou and Jaupart (1995) showed that when the surface has variable thermal boundary conditions representing oceanic and continental lithospheric areas, the upwelling tends to be beneath the continent and the convection cells become elongated. Grigné et al. (2007b) investigated how the presence of a region with a lid of finite conductivity affects the wavelength of mantle convection and forces the zone of upwelling under the continent while the cold downwellings form at a distance from the continent. Their study also found that the presence of a partial lid produces longer wavelength convection cells with increasing Rayleigh numbers in contrast with Guillou and Jaupart (1995) who showed no effect of cell size with different values of the Rayleigh numbers. This difference is likely due to the difference in the mechanical boundary conditions.

Being less dense and therefore, more buoyant than the mantle, continents do not participate in mantle overturn. Both numerical and laboratory based models have been created to investigate the

dynamic interaction between the continental lithosphere and the mantle (Gurnis, 1988; Zhong and Gurnis, 1993; Guillou and Jaupart, 1995; Lowman and Jarvis, 1995, 1996, Lenardic and Kaula, 1995, 1996; Lenardic, 1997, 1998; Lenardic et al., 2005; Moresi and Lenardic, 1997; Grigné and Labrosse, 2001; Grigné et al., 2005, 2007a, b).

Lenardic and Moresi (2001,2003) investigated the variation of the surface heat flux as a function of the thickness and the lateral extent of the thermally coupled continents, and derived a parameterized model based on their numerical model results. They also showed that surface heat flux varies only weakly with the thickness of a continent provided it is much less than the depth of the mantle (Lenardic and Moresi, 2001). In their parameterized model, Grigné and Labrosse (2001) showed that the thermal blanketing effect of continents significantly affects the mantle cooling rate (Guillou and Jaupart, 1995; Lenardic and Moresi, 2001). However, Lenardic et al. (2005) showed that, in the presence of temperature-dependent viscosity, cooling could actually be enhanced by continents.

The seismic reflector at 660 km-depth is caused by the endothermic phase transition that converts spinel to magnesiowüstite and perovskite (Akaogi et al., 2007). The reaction has a negative Clapeyron slope and as a result, cold downwellings need higher and hot upwellings need lower pressure to be in equilibrium. There is a resulting buoyancy force caused by the displacement of the phase boundary since the lower phase is denser, which, for the endothermic phase transition, oppose the thermally driven flow (Schubert et. al, 2001). Increasing the magnitude of the Clapeyron slope increases the degree of phase boundary deflection and generally the degree of layering. However, when the Clapeyron slope is sufficiently low, the upwellings become hotter and the downwellings become colder due to the effect of latent heating as they penetrate the 660 km-depth endothermic phase boundary (Schubert et al., 1995). This heat source coupled with the thermal expansivity of mantle materials provides additional buoyancy enhancing mantle flow (Schubert et al., 1975).

Tomographic studies, mainly from the circum Pacific region (van der Hilst et al., 1997; Fukao et al., 2001; Chen and Brudzinski, 2003; Kennett and Gorbatov, 2004; Ritsema et al., 2004; Zhao, 2004), showed that some subducting slabs flatten out and appear to be blocked, while others penetrate the boundary at a depth of 660 km, indicating that the mantle is incompletely layered by the phase boundary.

When comparing models with and without the phase boundary, the percentage decrease in mass flux increases as the Rayleigh number increases (Machetel and Weber, 1991; Peltier and Solheim, 1992; Zhao et al., 1992; Solheim and Peltier, 1993, 1994a, b; Tackley et al., 1993; Weinstein, 1993). This indicates that if the mantle circulation is weakened by the viscous drag and the insulating effects of continents, which decrease the effective Rayleigh number, the degree of layering might be expected to be less than in comparable models without continents.

Tackley (1995) showed that long-wavelength flows and broad upwellings and downwellings are

more likely to penetrate the phase boundary. Butler and Peltier (1997) studied the linear stability of an internal thermal boundary layer and showed that the most unstable mode that penetrates the phase boundary has a long-wavelength. Tackley (1995) showed that the critical phase buoyancy parameter necessary to induce layering increases with the flow wavelength. Since the presence of a partial lid causes longer wavelength convection cells (Grigné et al., 2007b), one might expect layering to be decreased in the presence of partial continental coverage.

Layering, induced by the endothermic phase boundary, affects the mantle flow in a number of different ways. The absolute mass flux across 660 km-depth, M_f, gives an estimate of the mechanical layering and is reduced as the layering increases. The reduced mass flux also reduces the heat advected across 660 km-depth leading to the formation of an internal thermal boundary layer. I parameterize this thermal measure of layering by considering the ratio, β, of the conductive to the total heat flux across the phase boundary (Butler and Peltier, 2000). I also consider the difference in the number of convection rolls in the upper and the lower mantle as a measure of the degree of layering-induced convective decoupling. Finally, the surface heat flux, which is parameterized by the Nusselt number, Nu, is also reduced by layering because of the reduction in heat flux from the lower to the upper mantle. I will demonstrate that the effect of layering on Nu is greatly reduced when using mixed surface boundary conditions, while the effect on M_f is reduced somewhat less.

Previously, numerical simulations of convection scaled to the Earth's mantle have shown that in the presence of internal heating, which models the effects of radioactive decay, the temperature increases with depth more slowly than would be predicted assuming adiabaticity (McKenzie et al., 1974; Sotin and Labrosse, 1999; Matyska and Yuen, 2000; Bunge et al., 2001). In other words, the mantle geotherm becomes subadiabatic. The heat flux at the CMB can be estimated based on the temperature drop at the CMB (Buffett, 2002). A subadiabatic mantle geotherm will result in larger estimates for the temperature drop at the CMB leading to higher estimated heat flux from the core. Sinha and Butler (2007) showed that horizontal advection, which becomes increasingly significant in large aspect ratio convection cells, can also play an important role in producing a subadiabatic geothermal gradient. The models with a partial lid or with very strong layering in a wide box tend to produce long-wavelength convection cells and hence, stronger horizontal advection. As I will demonstrate, this causes the geothermal gradient to be subadiabatic despite the absence of internal heating in these cases.

In the following section I describe my numerical models and subsequently I define the model diagnostics. My calculations and their control parameters and calculated diagnostics have been listed in Table 4.1. I discuss the effects of the endothermic phase boundary in the presence of different surface boundary conditions in section 4.4.1. The effects of different lengths of the continent and internal heating on layering will be presented in section 4.4.2. Finally, in section 4.4.3 I demonstrate that the mantle geotherm is substantially subadiabatic in the presence of mixed surface boundary

conditions. The final section summarizes the results and findings.

4.2 Numerical Model Description

I employed two numerical models, one finite-difference and one finite-element. The finite-element simulations employed the commercial software package COMSOL[1]. The finite-element solver was found to be more stable for calculations with large Rayleigh numbers. A number of repeat calculations indicate that the results of the two methods are very similar. Finite-element models are indicated with † in table 4.1. The infinite-Prandtl number Navier-Stokes equation for a Boussinesq fluid and an energy equation incorporating the buoyancy and the thermal effects of an endothermic phase boundary were solved in two-dimensional 1×1, and 8×1 boxes using 289×289, and 2305×289 grids, respectively, for the finite-difference calculations. The finite-element models were calculated in 8×1 boxes with 37084 Lagrange-Quadratic elements and denser mesh was used along the horizontal and the endothermic phase boundaries. All of my calculations were carried out in an isoviscous fluid. The dimensionless governing equations are

$$T\hat{k} - \Gamma \frac{\Delta\rho}{\rho\alpha\Delta T}\hat{k} - \nabla p + \nabla^2 \mathbf{U} = 0, \tag{4.1}$$

$$\nabla \cdot \mathbf{U} = 0, \tag{4.2}$$

and

$$\left[1 + 2\Gamma(1-\Gamma)\frac{\gamma l h}{\rho c_p g}\right]\left(\frac{\partial T}{\partial t} + \mathbf{U}\cdot\nabla T\right) = \frac{1}{Ra}\nabla^2 T - 2\Gamma(1-\Gamma)\frac{hld}{c_p\,\Delta T}\mathrm{v} + H. \tag{4.3}$$

In the above equations T, $\mathbf{U} = [\mathrm{u}, \mathrm{v}]$, p and t are the temperature, velocity, pressure and time, respectively, while Ra, H, g, ρ, α, ΔT, c_p and d are the Rayleigh number, non-dimensional internal heating rate, acceleration due to gravity, density of the mantle, thermal expansion coefficient, total temperature difference across the mantle, specific heat capacity at constant pressure and the depth of the whole mantle, respectively. Time and length are scaled with $d^2/(\kappa Ra)$ and d, where κ is the thermal diffusivity. The symbols γ, l, $\Delta\rho$ and h are the Clapeyron slope of the endothermic phase boundary, latent heat, density jump across the phase boundary and a thickness parameter, respectively, and

$$\Gamma = \frac{1}{2}(1 + \tanh\theta), \tag{4.4}$$

where

$$\theta = hd\left[z_{660} - \frac{\gamma\,\Delta T}{\rho g d}(T - < T >_{660}) - z\right]. \tag{4.5}$$

Here z is the height and $< T >_{660}$ is the average temperature at 660 km-depth. The height at which $\theta = 0$ gives the height of the phase boundary, which I define as z_p. The second term in equation 4.1 represents the buoyancy created by the deflection of the phase boundary. The first multiplier on

[1] web page: http://www.comsol.com/

the left hand side and the second term on the right hand side of equation 4.3 represent the latent heating effect associated with the temperature and pressure-induced phase change, respectively. In my calculations I use $g = 10\,\mathrm{ms}^{-2}$, $\rho = 4000\,\mathrm{kgm}^{-3}$, $\alpha = 2.5 \times 10^{-5}\,\mathrm{K}^{-1}$, $\Delta T = 3700\,\mathrm{K}$, $c_p = 1200\,\mathrm{JKg}^{-1}\mathrm{K}^{-1}$, $d = 2890\,\mathrm{km}$ (Schubert et al., 2001), $\Delta\rho = 440\,\mathrm{kgm}^{-3}$, $z_{660} = 0.77$ and $h = 3.5 \times 10^{-5}\,\mathrm{m}^{-1}$. I calculate l using the Clausius-Clapeyron relation.

In my finite-difference models, the Navier-Stokes equation was converted to the following stream-function (ψ) vorticity (ω) pair of Poisson's equations, which were solved using MUDPACK (Adams, 1991),

$$\nabla^2\omega = \frac{\partial T}{\partial x}\left[1 + 2\Gamma(1-\Gamma)\frac{\Delta\rho h\gamma}{g\alpha\rho^2}\right], \tag{4.6}$$

$$\nabla^2\psi = \omega. \tag{4.7}$$

In models that include the effects of continental lithosphere, an insulating layer of thickness $h_c = 0.04d$ (approx. 115 km) is placed on the top of the solution domain using the same technique as in chapter 2. It is assumed that the heat flux across the base of the continental lithosphere is the same as the heat flux at the surface and the mechanism of heat transport within the continent is entirely vertical conduction. As such, the temperature profile in the continent is linear. If I take the mantle and the continental thermal conductivities to be equal, the heat flux balance at the base of the continental lithosphere can be written as

$$\frac{T_s - T_b}{h_c} = \frac{\partial T}{\partial z}|_{z=1}, \tag{4.8}$$

where T_s and T_b are the temperatures at the surface and the base of the continental lithosphere and I evaluate $\partial T/\partial z$ at the top of the mantle. I solve for T_b at each time-step and at each horizontal position beneath the continent as it serves as the top boundary temperature for the subcontinental mantle. In this way the heat flux and the temperature are made continuous at the mantle-continental lithosphere boundary. I define L as the length of the continent. Oceanic and continental regions are modeled as free-slip and no-slip.

All boundaries in all models have zero mass flux, while the side walls are reflecting (see fig. 2.4). The bottom boundary (core-mantle boundary) is free-slip and kept isothermal with a constant non-dimensional temperature, $T = 1$, and the isothermal top surface is kept at a non-dimensional temperature of 0 in regions with free-slip.

4.3 Diagnostics

To calculate β, the amount of heat carried across 660 km-depth by conduction and advection are required. If the conductive heat flux is Q_{cond} and the advective heat flux is Q_{adv}, then

$$\beta = \frac{Q_{\mathrm{cond}}}{Q_{\mathrm{cond}} + Q_{\mathrm{adv}}}, \tag{4.9}$$

where

$$Q_{\text{cond}} = -\int_0^l \frac{\frac{\partial T}{\partial z} - \frac{\partial T}{\partial x}\frac{\partial z_p}{\partial x}}{\sqrt{1+\left(\frac{\partial z_p}{\partial x}\right)^2}}\,dx, \tag{4.10}$$

$$Q_{\text{adv}} = -\int_0^l \frac{\mathrm{u}T\frac{\partial z_p}{\partial z} - \mathrm{v}T}{\sqrt{1+\left(\frac{\partial z_p}{\partial x}\right)^2}}\,dx. \tag{4.11}$$

I define M_f as

$$M_f = \int_0^l \frac{|\mathrm{v} - \mathrm{u}\frac{\partial z_p}{\partial x}|}{\sqrt{1+\left(\frac{\partial z_p}{\partial x}\right)^2}}\,dx, \tag{4.12}$$

where $z_p(x)$ is the location of the moving phase boundary and l is the length of the box. All of the above quantities are evaluated at height $z_p(x)$ and are temporally averaged.

The Nusselt number is calculated by averaging the vertical gradient of the temperature along the top boundary, while $< T >$ gives the average temperature of the solution domain. The variables C_{lm} and C_{um} are the number of convection cells calculated by counting the zero-crossings of ψ along the mid-depths of the lower ($z = 0.385$) and the upper mantle ($z = 0.885$). The total mass flux is zero between two adjacent locations where $\psi = 0$ along one upwelling and one downwelling indicating one complete convection cell. All models were run to a statistically steady state and then the above-mentioned quantities were time-averaged. All these diagnostics for aspect ratio 8 models are listed in table 4.1.

I also calculate the critical thermal boundary layer Rayleigh number, Ra_δ, as a measure of the thermal resistance of the boundary layer. From boundary layer theory (Schubert et al., 2001) it can be shown that

$$Nu = \left(\frac{Ra}{Ra_\delta}\right)^{1/3} \delta T^{4/3}. \tag{4.13}$$

From equation (4.13),

$$Ra_\delta = \frac{\delta T^4 Ra}{Nu^3}, \tag{4.14}$$

where Ra and Nu are the Rayleigh number and the Nusselt number and δT is the temperature difference across the thermal boundary layer. When the surface is free-slip, Ra_δ values range between 13.4 and 35.6, which is in agreement with previous studies (Honda, 1996; Sotin and Labrosse, 1999; Butler and Peltier, 2000; Sinha and Butler, 2007).

M	Ra	H	γ	L	h	$< T >$	Nu_c	Nu_o	M_f	β	$C_{\rm lm}$	$C_{\rm um}$
†Ra6H0p0∗	10^6	0	0	0	0	0.50	-	19.0	33.0	0.00	6.0	6.0
Ra6H0p1∗	10^6	0	-1	0	0	0.50	-	19.3	32.2	-0.01	6.4	6.4
Ra6H0p3∗	10^6	0	-3	0	0	0.51	-	18.4	28.3	-0.04	6.6	6.9
Ra6H0p5∗	10^6	0	-5	0	0	0.53	-	15.7	15.3	0.05	3.3	5.1
Ra6H0p7∗	10^6	0	-7	0	0	0.55	-	14.2	8.9	0.16	3.6	8.9
Ra6H0p9∗	10^6	0	-9	0	0	0.56	-	13.1	8.2	0.27	2.2	4.9
Ra6H0p0L8	10^6	0	0	8	0.04	0.72	6.9	-	13.6	-0.02	5.3	8.3
†Ra6H0p0L8	10^6	0	0	8	0.04	0.72	6.6	-	12.1	-0.02	5.1	6.6
Ra6H0p1L8	10^6	0	-1	8	0.04	0.74	7.2	-	13.9	-0.06	7.5	8.9
Ra6H0p3L8	10^6	0	-3	8	0.04	0.75	7.3	-	11.2	-0.08	8.1	11.2
Ra6H0p5L8	10^6	0	-5	8	0.04	0.74	7.1	-	5.2	0.16	6.0	16.0
Ra6H0p7L8	10^6	0	-7	8	0.04	0.74	6.3	-	2.5	0.39	3.0	14.6
Ra6H0p9L8	10^6	0	-9	8	0.04	0.74	5.7	-	1.8	0.56	3.0	17.4
Ra6H0p0L2.4	10^6	0	0	2.4	0.04	0.57	6.3	16.1	20.3	-0.01	2.7	3.1
†Ra6H0p0L2.4	10^6	0	0	2.4	0.04	0.57	6.1	14.7	17.8	-0.02	1.7	2.2
†Ra6H0p0L4	10^6	0	0	4	0.04	0.61	6.1	14.2	15.2	-0.01	1.4	3.1
†Ra6H0p0L5.6	10^6	0	0	5.6	0.04	0.65	6.2	14.6	14.2	-0.01	2.9	4.5
†Ra6H0p0L7.2	10^6	0	0	7.2	0.04	0.67	6.0	18.2	13.4	-0.01	2.1	4.1
Ra6H0p1L2.4	10^6	0	-1	2.4	0.04	0.58	6.3	17.2	21.7	-0.03	3.7	3.9
Ra6H0p3L2.4	10^6	0	-3	2.4	0.04	0.58	6.5	17.2	18.7	-0.03	3.2	3.6
†Ra6H0p3L2.4	10^6	0	-3	2.4	0.04	0.57	6.3	16.7	17.3	-0.01	2.5	2.9
Ra6H20p3L2.4	10^6	20	-3	2.4	0.04	0.93	11.2	29.3	16.6	0.01	2.1	4.8
‡Ra6H0p3L2.4	10^6	0	-3	2.4	0.04	0.59	6.6	16.4	16.6	-0.04	2.2	2.5
‡Ra6H20p3L2.4	10^6	20	-3	2.4	0.04	0.91	10.2	30.2	18.4	0.00	3.2	7.3
Ra6H0p3L4	10^6	0	-3	4	0.04	0.62	6.7	16.5	13.6	-0.02	1.5	2.3
Ra6H0p3L5.6	10^6	0	-3	5.6	0.04	0.67	7.0	17.3	12.4	-0.04	3.3	4.5
Ra6H0p3L7.2	10^6	0	-3	7.2	0.04	0.71	7.1	21.2	11.8	-0.06	5.5	7.8
Ra6H0p5L2.4	10^6	0	-5	2.4	0.04	0.58	6.5	16.4	11.6	0.06	2.1	3.9
Ra6H0p7L2.4	10^6	0	-7	2.4	0.04	0.60	6.6	15.1	9.0	0.14	1.8	4.0
Ra6H0p9L2.4	10^6	0	-9	2.4	0.04	0.61	6.5	14.8	8.0	0.20	1.0	2.4
†Ra7H0p0∗	10^7	0	0	0	0	0.50	-	35.1	13.6	0.00	8.6	9.2
†‡Ra7H0p0L2.4	10^7	0	0	2.4	0.04	0.59	8.6	28.3	6.8	0.00	2.8	2.9
†Ra7H0p0L4	10^7	0	0	4	0.04	0.62	7.8	27.2	5.0	-0.01	1.7	2.7
‡Ra7H40p0L2.4	10^7	40	0	2.4	0.04	0.94	14.4	60.1	9.2	0.00	3.8	11.7

†‡Ra7H40p0L2.4	10^7	40	0	2.4	0.04	0.95	13.7	58.7	8.7	0.00	3.4	10.6
‡Ra7H0p3L2.4	10^7	0	-3	2.4	0.04	0.60	9.1	35.3	5.8	0.01	2.2	2.6
‡Ra7H40p3L2.4	10^7	40	-3	2.4	0.04	0.94	14.5	60.9	6.1	0.03	3.0	8.1
†Ra7H0p3∗	10^7	0	-3	0	0	0.51	-	32.8	8.3	0.01	6.9	8.9
†Ra7H0p3L2.4	10^7	0	-3	2.4	0.04	0.57	8.3	32.3	5.2	0.01	2.6	4.1
†Ra7H0p3L4	10^7	0	-3	4	0.04	0.61	8.1	31.4	4.2	-0.01	1.5	1.9
†Ra7H0p3L5.6	10^7	0	-3	5.6	0.04	0.66	8.6	34.3	3.6	-0.01	1.9	2.4
†Ra7H0p3L7.2	10^7	0	-3	7.2	0.04	0.70	8.8	43.5	3.2	-0.01	2.5	4.3
†Ra7H0p3L8	10^7	0	-3	8	0.04	0.77	10.1	-	3.4	-0.01	9.0	14.1

Table 4.1: models, M; Rayleigh number, Ra; non-dimensional internal heating rate, H; Clapeyron slope, γ ($\times 10^6$ Pa/K); non-dimensional length and thickness of the continental lithosphere, L and h, respectively; average temperature, $< T >$; non-dimensional surface heat flux or the Nusselt number over the continent, Nu_c and over the ocean, Nu_o; mass flux across the phase boundary, M_f ($\times 10^{-5}$); thermal layering parameter, β; number of convection cells in the lower and upper mantle, $C_{\rm lm}$ and $C_{\rm um}$, respectively. Only the results from aspect ratio 8 calculations have been listen here.

† computations were carried out using finite element method

‡ surface contains two separate continents, located at the either end of the box covering 15% each

∗ models with free-slip surface

4.4 Numerical Model Results

4.4.1 Effects of Surface Boundary Conditions and Aspect Ratio on Layering

Fig. 4.1 shows temperature snapshots overlain by the stream function from models with free-slip (4.1a), conducting lid (4.1b) and mixed (4.1c) surface boundary conditions. A Rayleigh number of 10^6 was used and the Clapeyron slope is 0 in these models (Ra6H0p0$*$, Ra6H0p0L8, Ra6H0p0L2.4). The black horizontal line indicates the fixed position of the endothermic phase boundary. When the surface is free-slip, (fig. 4.1a) there are 6 distinct whole-mantle convection cells, while fig. 4.1c shows a very long-wavelength convection cell with an upwelling beneath the continent due to the presence of a partial lid (Grigné et al., 2007b). Fig. 4.1b shows a warmer mantle due to the blanketing effect of the full conducting lid and five rolls. Note, in fig. 4.1c the upwelling plumes are advected laterally by the dominant long-wavelength flow more rapidly at their base than in the interior due to higher horizontal velocity at the lower boundary. The downwellings also show similar behavior in areas with free-slip along the surface.

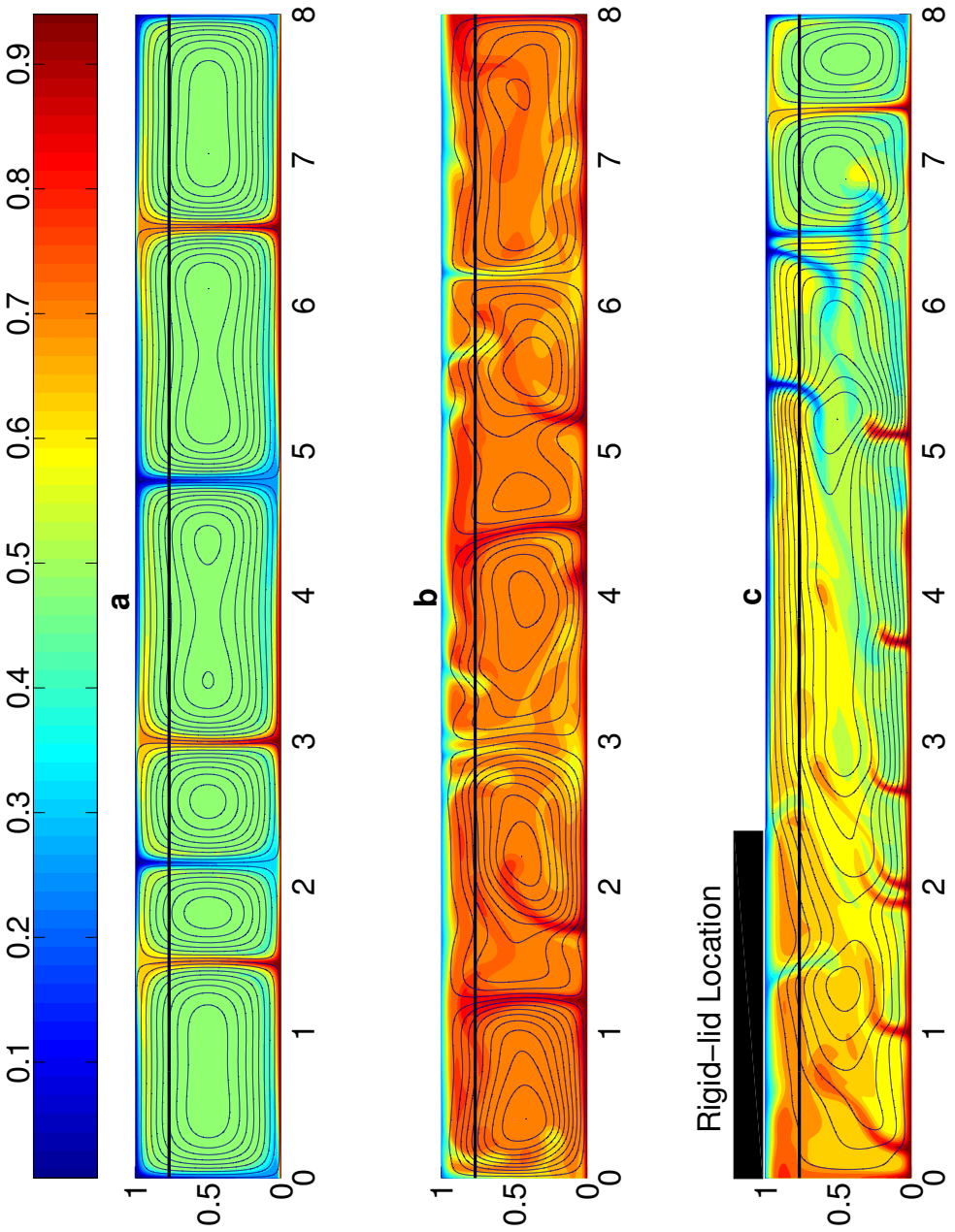

Figure 4.1: Temperature fields overlain by the streamlines for calculations with $Ra = 10^6$ and $\gamma = 0\,\mathrm{MPaK}^{-1}$ for (a) free-slip (Ra6H0p0∗), (b) conducting lid (Ra6H0p0L8) and (c) mixed (Ra6H0p0L2.4) surface boundary conditions. The black horizontal line represents the location of the phase boundary.

The measured value for the Clapeyron slope of the endothermic phase boundary is $-2.6 \pm 0.2\,\mathrm{MPaK}^{-1}$ (Akaogi et al., 2007). However, in order to present an extreme end member model for layering, I show fig. 4.2, where the Clapeyron slope is $-9\,\mathrm{MPaK}^{-1}$. The model with a complete conducting lid (Ra6H0p9L8, fig. 4.2b) shows a very significant decoupling between the upper and the lower mantle with very few streamlines crossing the phase boundary and also a large temperature difference. The strong drag created by the long continental lithosphere in this case significantly penalizes horizontal flow near the upper boundary producing multiple surface boundary layer instabilities from the base of the lid resulting in a significantly larger number of convection cells in the upper mantle. Regardless of the surface boundary condition, all calculations with large magnitudes of the Clapeyron slope have very long convection wavelength in the lower mantle, shown in fig. 4.2a, 4.2b and 4.2c, because the lower boundary is free-slip and there is some degree of mass flux across the phase boundary. Although calculations with mixed (Ra6H0p9L2.4) and complete free (Ra6H0p9$*$) surfaces are very different in planform in the absence of strong layering (fig. 4.1a and 4.1c), they become quite similar when strongly layered as can be seen by comparing fig. 4.2a and 4.2c. Note the multiple weak cold downwellings in the upper mantle for free and mixed cases due to very strongly layered mantle convection. These downwellings are weak because they are unable to penetrate through the phase boundary and also they cause deflections but not zero-crossings of the stream function. Carried by the dominant long-wavelength mantle flow, the weak surface boundary layer instabilities migrate and accumulate together before penetrating through the phase boundary into the lower mantle. The deflection of the phase boundary depends on the temperature anomaly at the boundary only, however, the total thermal density anomaly depends on the temperature above and below the phase boundary as well. As a result, anomalies of significant vertical and horizontal extent are more likely to penetrate the phase boundary and the accumulation of the boundary layer instabilities partially explains the tendency towards long-wavelength flows seen when large magnitudes of the Clapeyron slope are used.

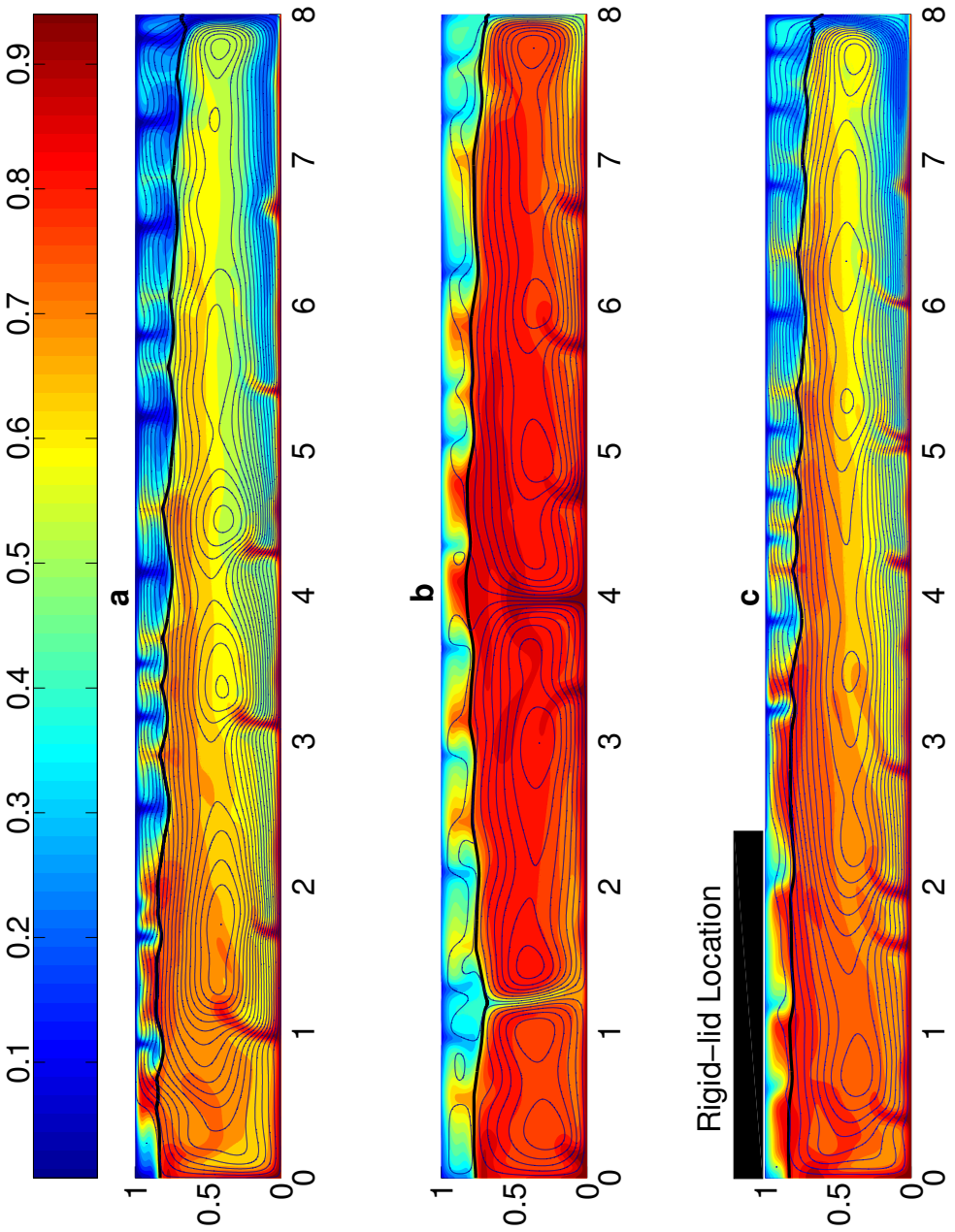

Figure 4.2: Temperature fields overlain by the streamlines for calculations with $Ra = 10^6$ and $\gamma = -9\,\mathrm{MPaK}^{-1}$ for (a) free-slip (Ra6H0p9∗), (b) conducting lid (Ra6H0p9L8) and (c) mixed (Ra6H0p9L2.4) surface boundary conditions. The black horizontal line represents the location of the phase boundary.

In order to examine the thermal degree of layering, I plot β in fig. 4.3 as a function of the Clapeyron slope in the presence of different surface boundary conditions for calculations with $Ra = 10^6$, performed in unit aspect ratio boxes. Mixed surface boundary models have 30% continental coverage on one side of the box. All of the calculations in square boxes show a sudden change from slightly negative β, caused by a positive temperature gradient at 660 km-depth due to latent heating, to almost 1, indicating that almost all of the heat transport across the phase boundary is by conduction when the magnitude of the Clapeyron slope of the endothermic phase boundary is greater than 6MPaK^{-1}. This result is consistent with the free-slip results of Christensen and Yuen (1985). Temperature snapshots in fig. 4.4 from unit aspect ratio models with different surface boundary conditions show the sudden change from whole mantle to almost completely layered convection. A plot of the Nusselt number for the same calculations can be seen in fig. 4.5 where a similar but downward jump is present, which also occurs in the mass flux across 660 km-depth (fig. 4.6). At $Ra = 10^7$, a similar phenomenon was observed (not shown) with the jump occurring between the Clapeyron slopes of $-3\,\mathrm{MPaK}^{-1}$ and $-4\,\mathrm{MPaK}^{-1}$ due to the increased degree of layering with increased Rayleigh number (Christensen and Yuen, 1985).

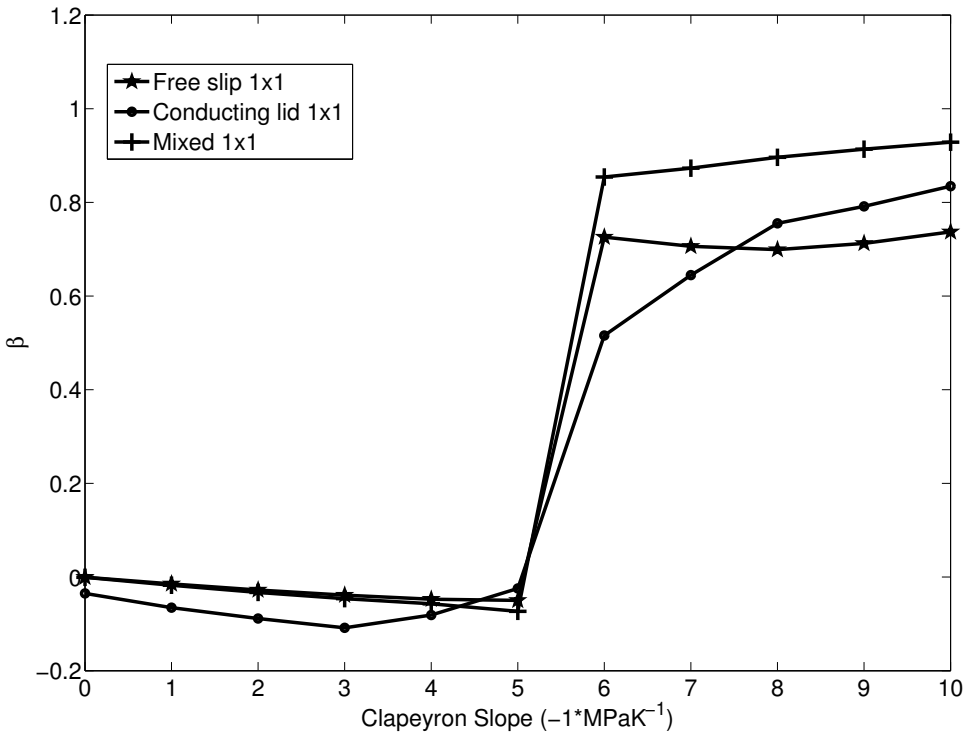

Figure 4.3: Layering parameter, β, as a function of the Clapeyron slope of the endothermic phase boundary for calculations in unit aspect ratio boxes with $Ra = 10^6$.

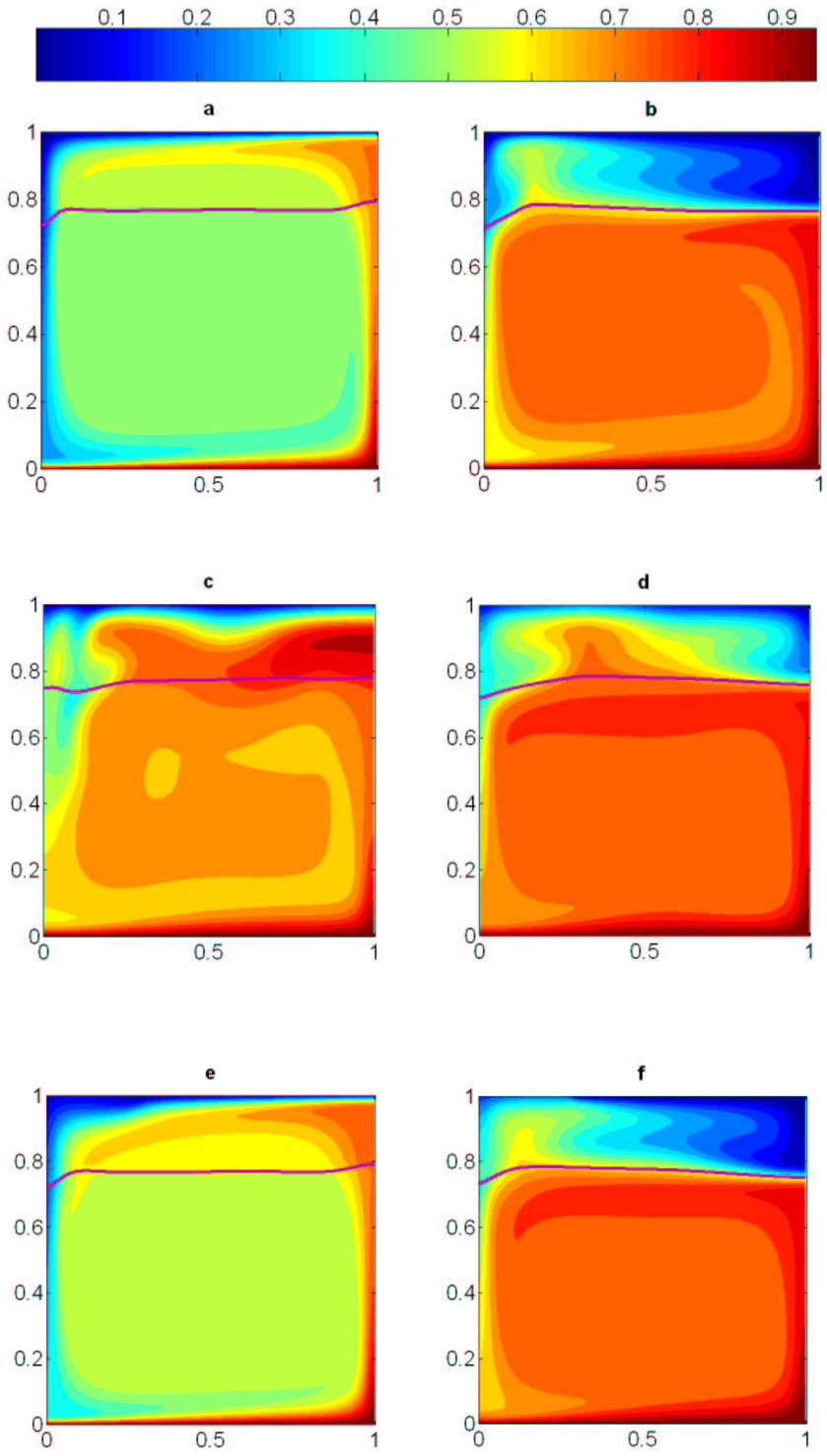

Figure 4.4: Temperature field plots from calculations for $Ra = 10^6$ with different surface boundary conditions and the endothermic phase boundary. Free-slip with (a) $\gamma = -4\,\mathrm{MPaK}^{-1}$ and (b) $\gamma = -6\,\mathrm{MPaK}^{-1}$; conducting lid with (c) $\gamma = -4\,\mathrm{MPaK}^{-1}$ and (d) $\gamma = -6\,\mathrm{MPaK}^{-1}$ and mixed surface boundary conditions with (e) $\gamma = -4\,\mathrm{MPaK}^{-1}$ and (f) $\gamma = -6\,\mathrm{MPaK}^{-1}$. The purple horizontal line represents the location of the phase boundary.

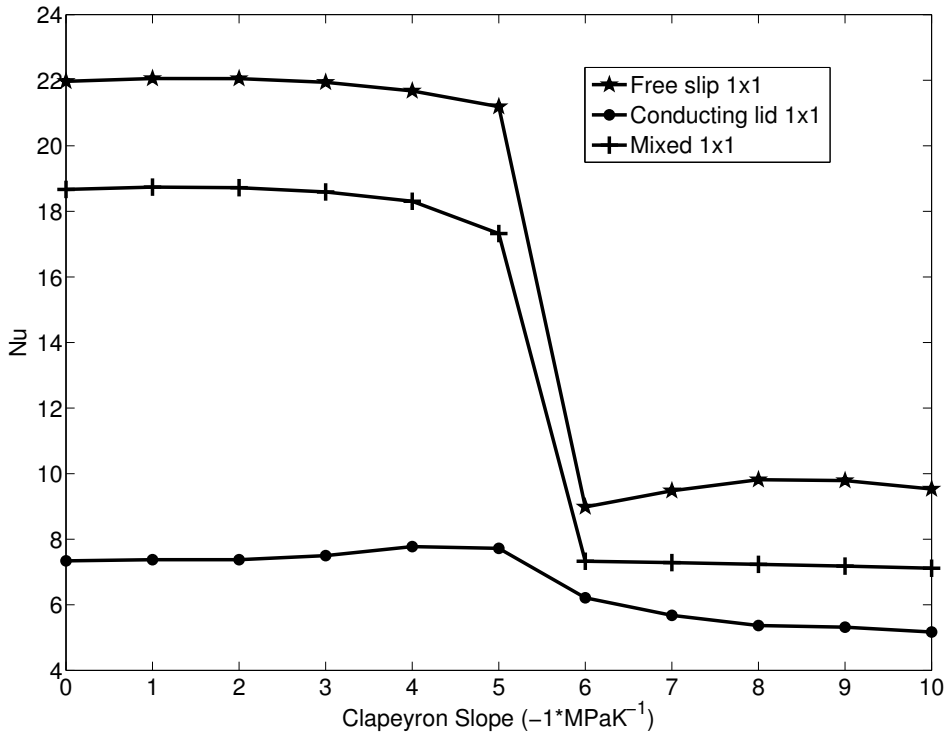

Figure 4.5: Nusselt number, Nu, as a function of the Clapeyron slope of the endothermic phase boundary for calculations in unit aspect ratio boxes with $Ra = 10^6$.

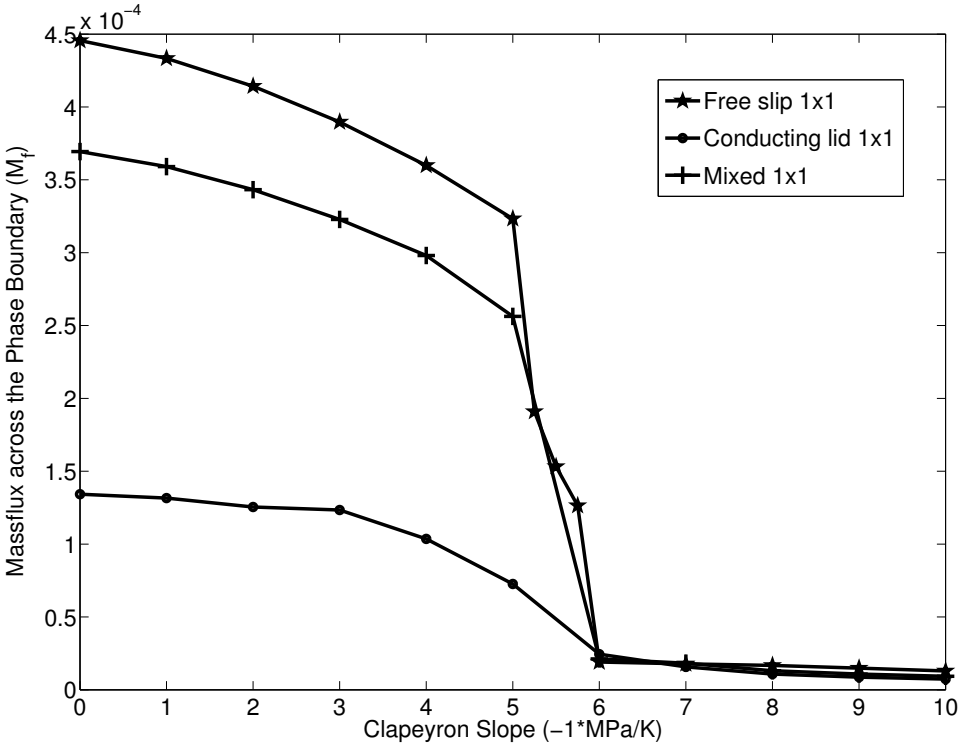

Figure 4.6: Average mass flux, M_f, as a function of the Clapeyron slope of the endothermic phase boundary for calculations in 1×1 boxes with $Ra = 10^6$

The layering diagnostics from calculations in 8×1 boxes are shown in fig. 4.7, 4.8 and 4.9. Here also the mixed surface boundary models have 30% coverage with the continent located on one side of the box (as shown in fig. 4.1c and 4.2c). For the 8×1 models, these plots show that for all of the surface boundary conditions examined, the change in the degree of layering, with increasing magnitude of the Clapeyron slope, is much more gradual than in the 1×1 cases. The thermal layering (β) across 660 km-depth starts to increase when the magnitude of the Clapeyron slope is more than $3\,\mathrm{MPaK}^{-1}$. However, at the largest magnitude of the Clapeyron slope β is less than in the case of square boxes, indicating that most of the heat is still being carried by advection across 660 km-depth and that the models are still only partially layered. This demonstrates that the degree of layering is strongly dependent on the aspect ratio of the box, which, for the case of a 1×1 calculation, strongly influences the wavelength of the convective rolls. This is in agreement with the results of Tackley (1995). In wider boxes the increased freedom allows for larger aspect ratio convection cells, causing a decreased degree of thermal layering.

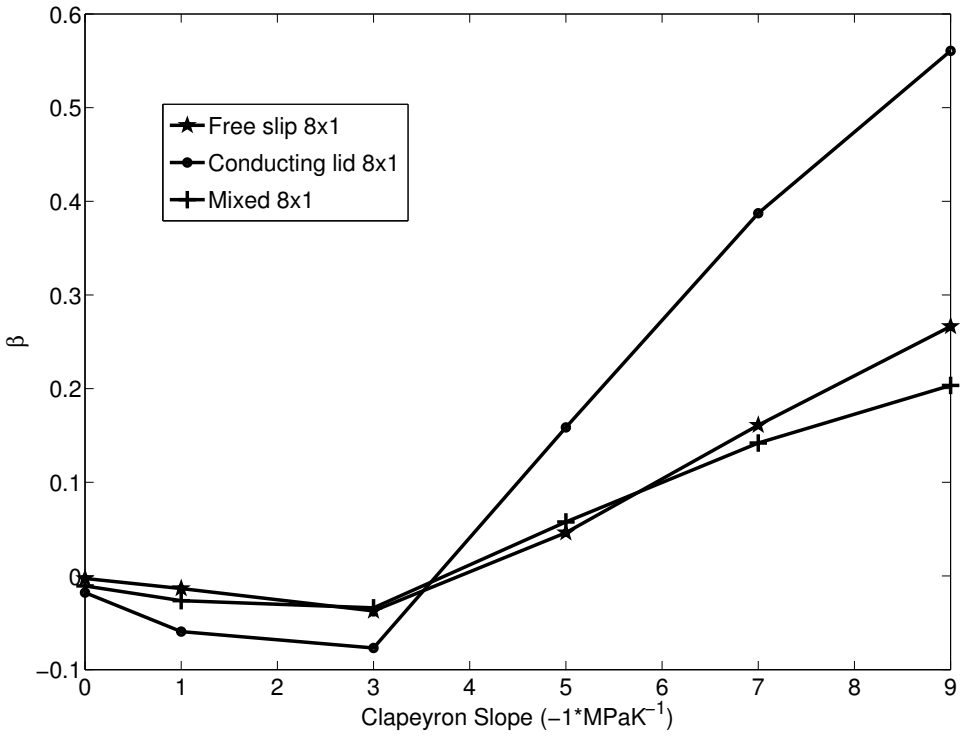

Figure 4.7: Layering parameter, β, as a function of the Clapeyron slope of the endothermic phase boundary for calculations in 8×1 boxes with $Ra = 10^6$.

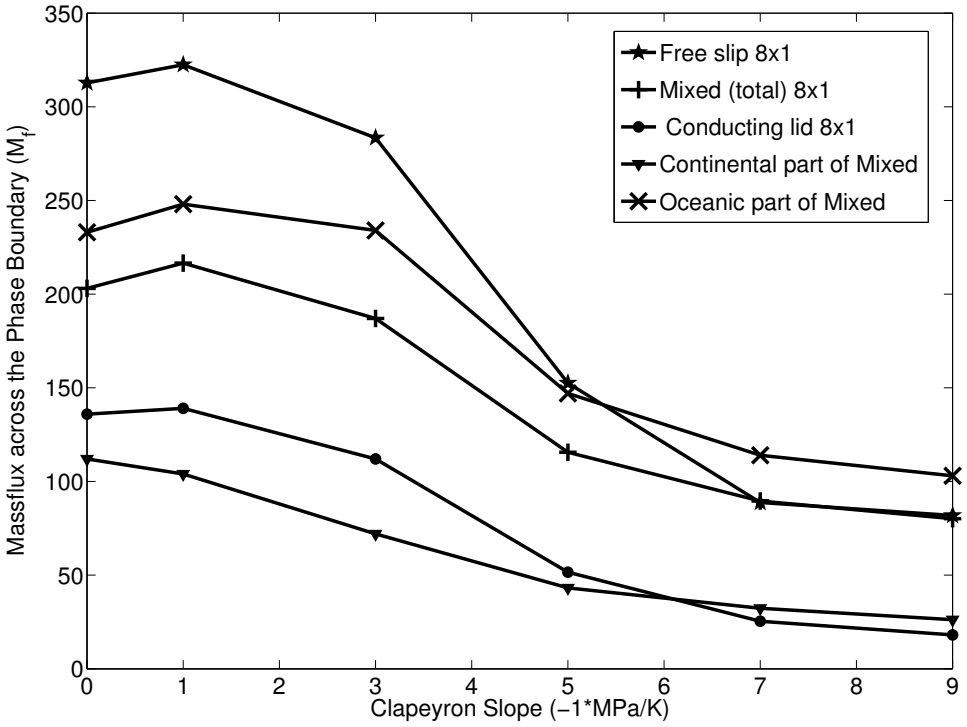

Figure 4.8: Average mass flux, M_f, as a function of the Clapeyron slope of the endothermic phase boundary for calculations in 8×1 boxes with $Ra = 10^6$.

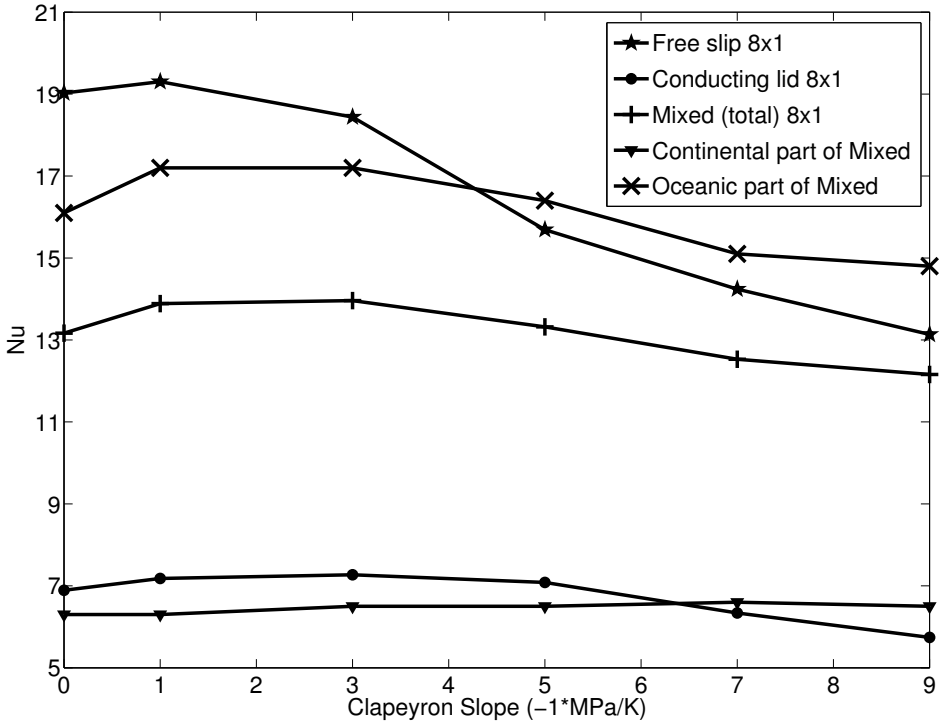

Figure 4.9: Nusselt number, Nu, as a function of the Clapeyron slope of the endothermic phase boundary for calculations in 8×1 boxes with $Ra = 10^6$.

As can be seen in fig. 4.7, rigid-lid calculations have the largest thermal layering due to the short-wavelength mantle flows despite the decreased convective vigor associated with the thermal insulation and viscous drag of the continents. The fraction of heat carried by conduction, as parameterized by β, is very similar for all degrees of layering for the models with free and mixed surface boundaries, except for very large magnitudes of the Clapeyron slope (fig. 4.7). This similarity is partly due to the fact that the total heat flux, as well as the total conduction of heat across 660 km-depth is less in the models with mixed surface boundary conditions. However, the surface heat flux and the mass flux across 660 km-depth are almost identical only for strongly layered models for these two types of calculations (fig. 4.8 and 4.9), despite the significant difference in simulations with lesser Clapeyron slopes. The negative values of β in fig. 4.7 are due to the inverted geotherms caused by the hotter upper mantle due to latent heat release.

Fig. 4.8 shows the variation in the average mass flux across the phase boundary as a function of the Clapeyron slope. Enhancement in convection due to the latent heating effect causes a very small increase in the mass flux for low magnitudes of the Clapeyron slope. At large magnitudes of the Clapeyron slope, models with free-slip surfaces show the most significant drop in mass flux due to layering. Both the continental region of the mixed cases and the models with total rigid lids have similar mass flux values and they are much less than the values under oceanic regions due to the drag at the surface. In the plot, mass flux for the mixed cases are the weighted average of the mass flux under the continental and oceanic regions from the corresponding models.

In fig. 4.9, I plot the surface heat flux with different magnitudes of the Clapeyron slope. Here also, I calculated continental and oceanic heat fluxes separately for models with mixed surface boundary conditions. The initial slight increase in the surface heat flux that is seen in many models for very low magnitudes of the Clapeyron slope is again due to the latent heating effect. Models with free-slip surface boundaries undergo a surface heat flux reduction of more than 30% or an absolute decrease of 5.9 with increased magnitudes of the Clapeyron slope. For total continental coverage it is close to 20% or 1.2 in absolute terms, while for mixed surface boundary calculations the absolute change is only 0.9 or 7%. I interpret this very small absolute change to arise because the mixed surface boundary conditions have a more significant effect on convective planform than the phase transition. As a result, the planform of convection is only weakly affected by the phase transition. In contrast, the models with free-slip surfaces show a significant change in planform with Clapeyron slope resulting in a large change in the surface heat flux. The heat flux over the continental regions for mixed cases show no dependence on Clapeyron slope and over the oceanic region the total decrease in heat flux is also very small. Since these models have no internal heating and are run to a statistical steady state, the surface heat flux is the same as the core-mantle boundary heat flux.

In order to isolate the effects of reduced mass flux on heat flux for different surface boundary conditions, I plot Nusselt number as a function of average mass flux across 660 km-depth boundary in fig. 4.10. Note that the oceanic and the continental parts of the mixed cases plot along similar trends as the free-slip and the rigid-lid cases. However, the total variations in the surface heat flux as well as the mass flux under the oceanic region for mixed cases are much less than that for free-slip cases. Under the oceanic lithosphere the surface heat flux shows significant correlation with the mass flux at 660 km-depth. However, under the continental lithosphere, the average mass flux is much smaller even without layering. In the rigid-lid case the slope of Nu vs. M_f is quite shallow, indicating a large change in the mass flux results in only a moderate change in the heat flux. Because of the dominance of the effects of the boundary condition on flow planform, the mass flux in the oceanic region for the mixed case decreases significantly less than for the free-slip case, resulting in a smaller decrease in surface heat flux.

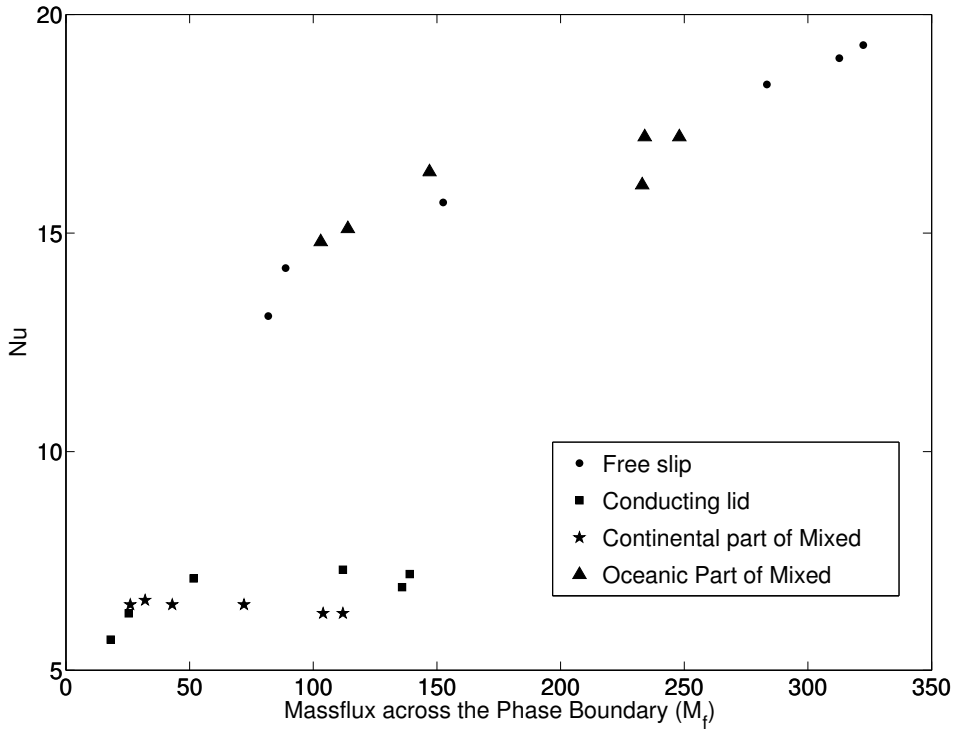

Figure 4.10: Nusselt number, Nu, as a function of the average mass flux across the phase boundary for calculations in 8×1 boxes with $Ra = 10^6$.

The critical upper boundary layer Rayleigh number (Ra_δ) for the same calculations that are shown in fig. 4.10, is plotted against average mass flux in fig. 4.11. The Nusselt number, Nu, is decreased by layering both because of the decrease in δT at the surface due to the temperature drop caused by the internal thermal boundary layer at 660 km-depth and the different convection planform caused by the interruption of flow at that depth. The parameter Ra_δ isolates the effect of planform and can be used as a measure of the thermal resistance across the upper boundary or the decrease in the convective vigor in the upper mantle caused by layering. In the plot, Ra_δ is much less for the oceanic than the continental regions because of the drag induced by the continent. Models with free-slip surfaces show a decrease in Ra_δ with mass flux, indicating lesser heat transport efficiency in the upper mantle for large magnitudes of the Clapeyron slope, which along with the decrease in δT is responsible for the large change in the Nusselt number shown in fig. 4.9. The oceanic part of the mixed surface calculations does not show any significant change in the thermal resistance of the upper mantle flows indicating that there is no significant change in the planform. Under complete lids, the critical upper boundary layer Rayleigh number surprisingly increases with mass flux, which indicates that the upper boundary layer transports heat more efficiently in the presence of stronger layering. When not layered, the convective planform is affected by the free-slip lower boundary and the depth of the mantle, however, when layered, the upper mantle planform is affected by the depth to the phase boundary and hence has a shorter wavelength. This planform transports heat more efficiently under a rigid lid. This increased efficiency in continental regions explains the slight change in the surface heat flux in the calculations with conducting lid surface boundary condition. Models with mixed surface boundary conditions also show an increase in the number of cold downwellings under the continent for large magnitudes of the Clapeyron slope (compare fig. 4.1c and 4.2c) leading to a similar increase in the heat transport efficiency. The Nusselt number for complete lid models increases with mass flux because δT increases as the flow becomes less layered and the temperature drop at 660 km-depth decreases, which, in this case is more significant than the increase in the boundary layer efficiency. However, δT decreases with Clapeyron slope much less for the continental part of the mixed cases due to the weaker thermal layering. This, combined with the increased efficiency in the upper boundary layer, causes Nu to be essentially independent of M_f (e.g. Ra6H0p0L2.4, Ra6H0p1L2.4, Ra6H0p3L2.4, Ra6H0p5L2.4, Ra6H0p7L2.4 and Ra6H0p9L2.4).

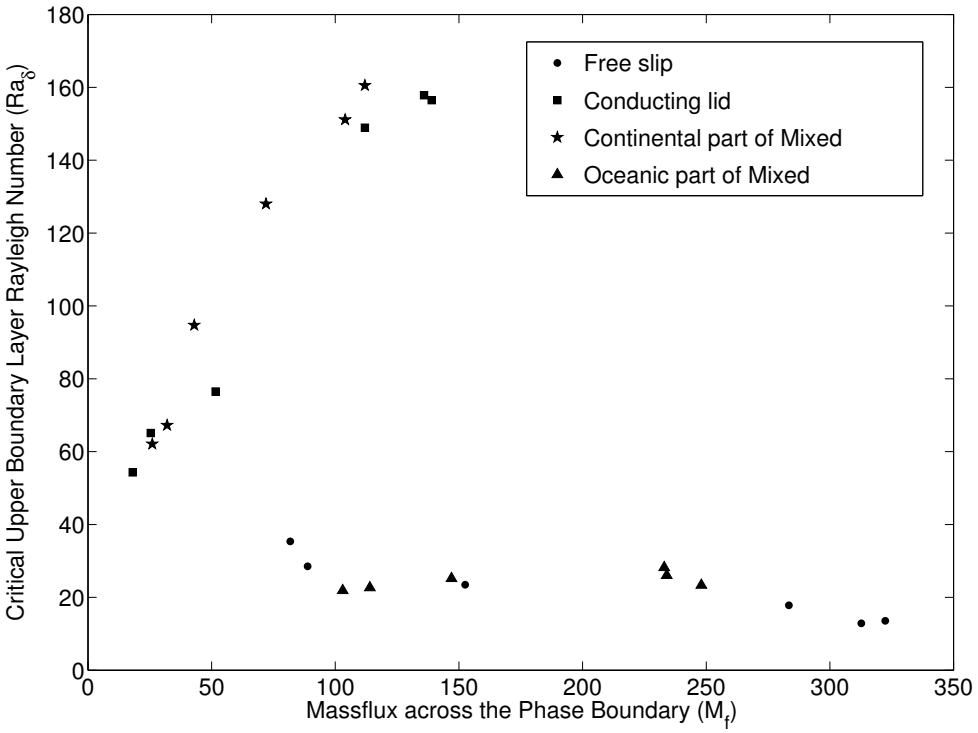

Figure 4.11: Critical upper boundary layer Rayleigh number as a function of the average mass flux across the phase boundary for calculations in 8×1 boxes with $Ra = 10^6$.

In fig. 4.12, the black and the grey bars correspond to the time-averaged number of convection cells in the lower ($C_{\rm lm}$) and the upper mantle ($C_{\rm um}$). Differences in the heights of the black and grey bars at a particular Clapeyron slope indicate separate convective regimes in the upper and the lower mantle, or decoupled mantle convection due to the endothermic phase boundary. I plot the results for all three different boundary conditions. Decoupling is evident in all calculations with large Clapeyron slopes.

In fig. 4.12b, results of calculations where the surface is completely covered by a conducting lid are shown. A significant increase in the number of convection cells can be observed in the upper mantle for strongly layered cases. This indicates the presence of several short-wavelength convection cells driven by the surface boundary layer instabilities above the phase boundary. The short-wavelength flows in the upper mantle are easily blocked by the phase boundary resulting in a strong internal thermal boundary layer along the endothermic phase boundary producing large values of β.

The models with free-slip and mixed surfaces (fig. 4.12a and 4.12c) show a lesser degree of decoupling between the upper and the lower mantle than the rigid-lid models. Although there is an increase in the upper mantle downwellings when strongly layered for the free-slip and the mixed cases, they are not sufficiently strong to cause zero-crossings of the stream function and are laterally swept by the dominant long-wavelength flows. The smallest number of convection cells, indicating long-wavelength flows, are obtained for mixed cases, regardless of the value of the Clapeyron slope. For all of the surface boundary conditions used, the convection wavelength in the lower mantle is longest when large magnitudes of the Clapeyron slope are used because flow is driven by the long-wavelength convection cells that penetrate the phase boundary. Models with mixed surfaces show relatively little change in the number of rolls with Clapeyron slope, again indicating the dominance of the effects of mixed surface boundary conditions.

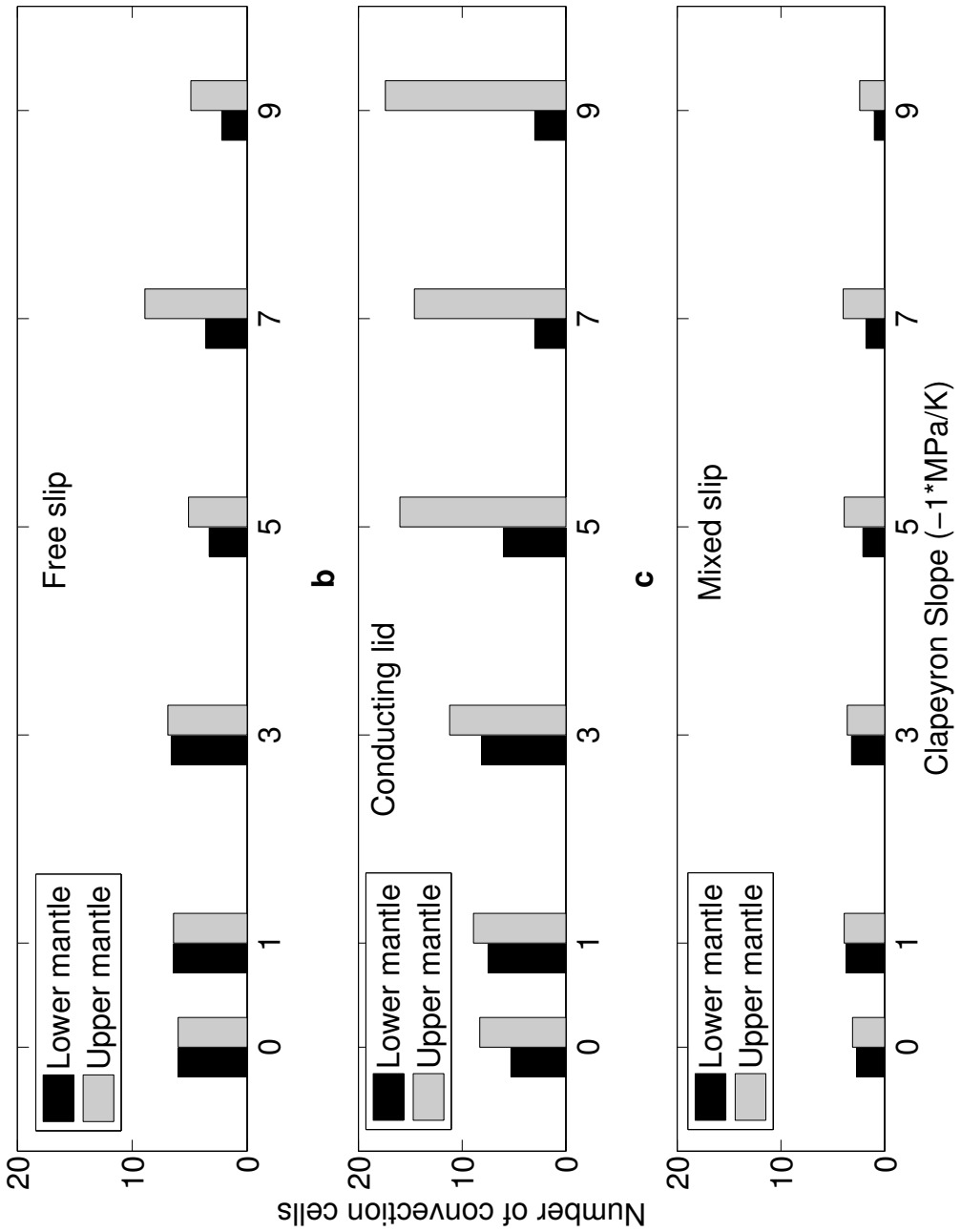

Figure 4.12: Number of convection cells in the upper (grey bars) and the lower (black bars) mantle as a function of the Clapeyron slope of the endothermic phase boundary for calculations with $Ra = 10^6$ and (a) free-slip, (b) conducting lid and (c) mixed surface boundary conditions in 8×1 boxes.

4.4.2 Effects of Different Continental Lengths and Internal Heating

A series of calculations were carried out to investigate the effect of different continental coverage for $Ra = 10^6$ and $Ra = 10^7$ with $\gamma = -3\,\mathrm{MPaK}^{-1}$. I also ran similar simulations for $Ra = 10^6$ with $\gamma = 0\,\mathrm{MPaK}^{-1}$. All of the models demonstrate an increase in Nu under the oceanic region (see Nu_o in table 4.1) when the continent covers 80% of the surface. This is due to the high temperature anomaly under the continent being swept laterally under ocean by the long-wavelength circulation as seen by Lenardic et al. (2005).

I changed the length of the continent starting from no lid to total coverage for every series. My results are shown as grouped bar plots in fig. 4.13 (similar to fig. 4.12). The most noticeable feature in these plots is that the number of rolls decreases dramatically as the continental coverage is increased from 0% to only 30%. As soon as the surface is changed to a total lid, the mantle is dominated by short-wavelength flows resulting in a greater decoupling between the upper and the lower mantle. Note that all models with partial coverage have similar planform, but the models with 50% coverage produce the longest wavelength convection cells.

Comparing fig. 4.13a and 4.13b, it can be seen that the higher Rayleigh number causes a stronger decoupling between the upper and the lower mantle in the absence of any continent and in the case of a total lid, reflecting increased layering with increased Rayleigh number. This occurs because of the narrower convective features seen in the higher Rayleigh number calculations. Guillou and Jaupart (1995), in their tank experiment where all the horizontal and vertical boundaries were rigid, showed no change in the flow wavelength with increasing Rayleigh number, however, when modeled numerically in a box with all free-slip boundaries, Grigné et al. (2007b) observed a correlation between the two variables and they demonstrated that the long convection cell wavelength varies as $Ra^{1/4}$ and produced a scaling theory arguing for this dependence. I also observe that fewer rolls are produced in calculations with $Ra = 10^7$ than $Ra = 10^6$ even though the surface boundary condition is partly rigid.

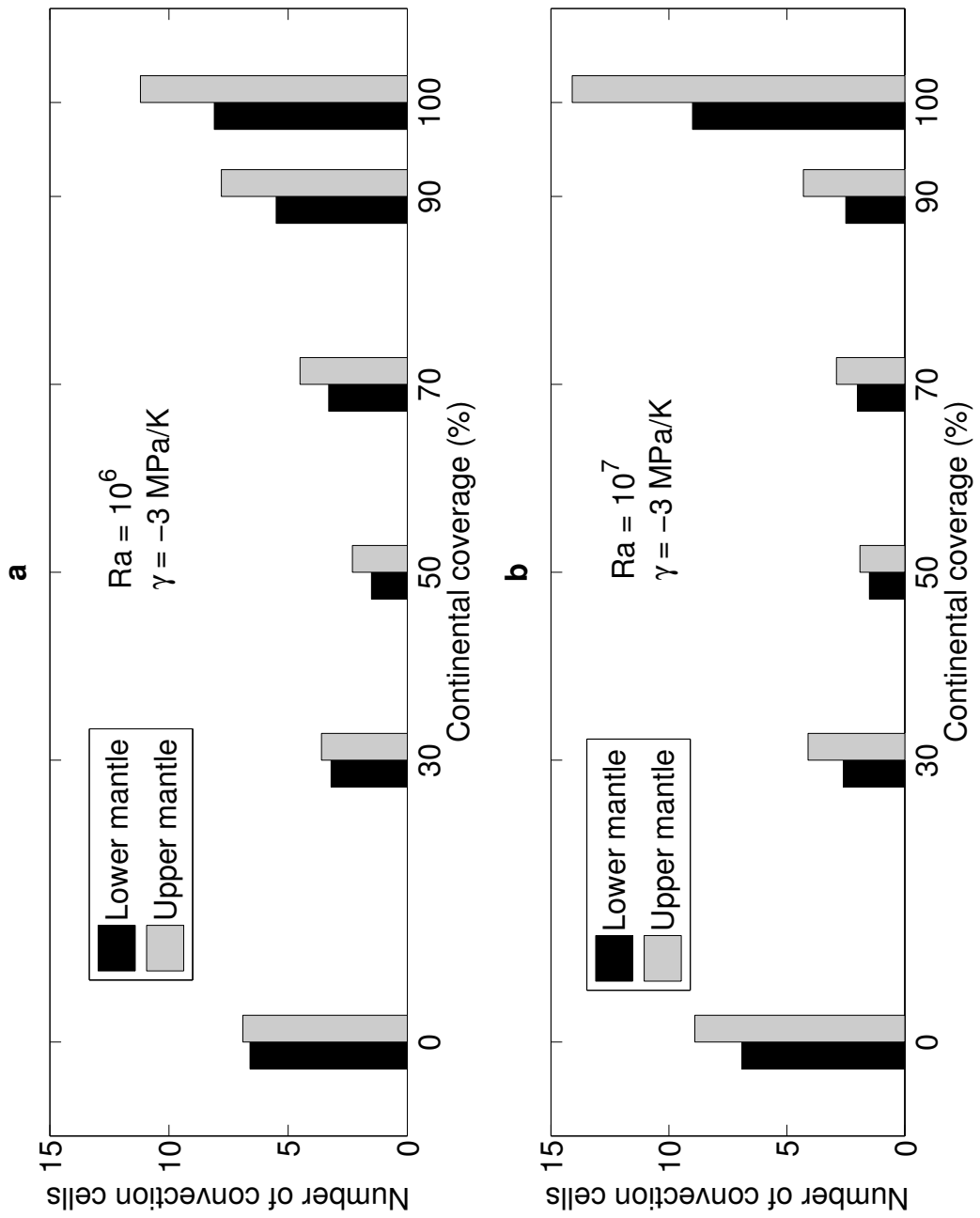

Figure 4.13: Number of convection cells in the upper (grey bars) and the lower (black bars) mantle as a function of the continental coverage for calculations with $\gamma = -3\,\mathrm{MPaK}^{-1}$ and (a) $Ra = 10^6$ and (b) $Ra = 10^7$ in 8×1 boxes.

Some of my models (Ra6H0p3L2.4, Ra6H20p3L2.4, Ra7H0p0L2.4, Ra7H40p0L2.4, †Ra7H40p0L2.4, Ra7H0p3L2.4, Ra7H40p3L2.4) contain two separate continents covering 15% at the extreme left and right sides of the box. My goal was to compare models with a single continent with a surface area of 30% and two continents totalling a surface area of 30%. Two-continent models resulted in two rolls with upwellings at either end of the box, however, as can be seen in Table 4.1, the measured diagnostics are very similar. This is because the wavelengths are still sufficiently long as to be only weakly affected by the phase boundary.

When internal heating was included in my models (Ra6H20p3L2.4, Ra6H20p3L2.4, Ra7H40p0L2.4, †Ra7H40p0L2.4, Ra7H40p3L2.4), the average temperature and the surface heat flux increased as expected. I also see a significant decrease in the flow wavelength mostly in the upper mantle. In these models, much warmer mantle produces stronger cold downwellings from the surface due to a larger thermal buoyancy contrast. These downwellings force the flow in the upper mantle to contain a large number of short-wavelength convection cells. However, β is similar to that of purely basally heated models. This is probably due to a larger total heat flux combined with a higher heat conduction across 660 km-depth in the presence of a stronger internal thermal boundary layer. The average temperature in Cartesian geometry is higher than in spherical geometry (Vangelov and Jarvis, 1994) and consequently, the presence of internal heating in Cartesian geometry results in very high internal temperatures.

4.4.3 Effect of Continents on the Shape of the Geotherm

The presence of a partial lid increases the convection wavelength, increasing the horizontal advection of heat. Sinha and Butler (2007) showed that subadiabaticity can occur in regions where the dominant thermal balance is between the horizontal and the vertical advection of heat. Consequently, the models with mixed surface boundary conditions, which have very large aspect ratio flows and a large amount of horizontal advection of heat, show subadiabatic geotherms (vertical profile of horizontally averaged temperature) even without the presence of internal heating. My models are incompressible and the temperature can be considered to be an approximation of the potential temperature in a compressible model (Jarvis and McKenzie, 1980). As a result, if the geotherm, interior to the surface and the basal thermal boundaries, has a positive slope, the temperature gradient is subadiabatic. In fig. 4.14, I plot the time-averaged geotherms from models with different continental coverage, L, $Ra = 10^7$ and $\gamma = -3\,\mathrm{MPaK}^{-1}$. In the absence of a continent, the geotherm is almost adiabatic inside the top and bottom boundary layers, with small overshoots resulting from the horizontal advection of heat near the boundaries (Jarvis and Peltier, 1982). Introducing a continent of 30% coverage results in a geotherm with positive slope, interior to the boundary layers. Although I show only one set of calculations here, all models with partial coverage show significant subadiabaticity, which can also be seen in fig. 4.1c and 4.2c, where temperature increases with height in the lower mantle above the cold, laterally advecting material near the core-mantle boundary. When I introduce full continental coverage, the interior of the geotherm becomes adiabatic because the long-wavelength convection cells are no longer present. The small bump at 660 km-depth is due to the presence of the phase boundary. I also observed subadiabaticity in the lower mantle geotherm for strongly layered models (not shown) caused by the presence of long-wavelength flows induced by the phase boundary. The temperature drop at the core-mantle boundary decreases with increasing continental coverage because of the increase in the average mantle temperature. However, the models with mixed boundary conditions have larger core-mantle boundary temperature drops than they would if they were adiabatic.

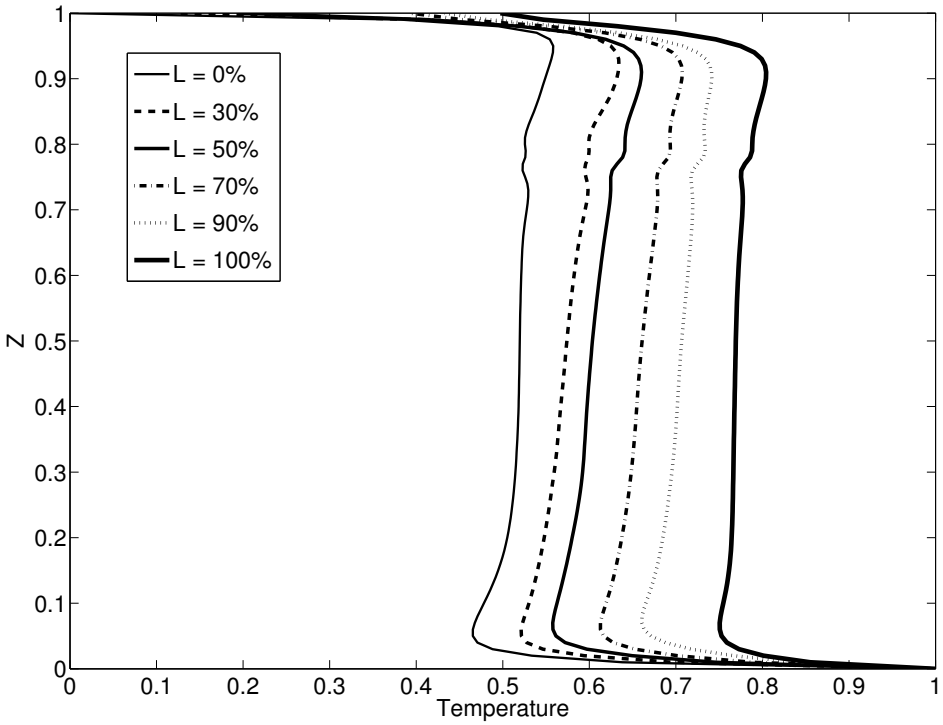

Figure 4.14: Geotherms as a function of the continental coverage, L, for calculations with $Ra = 10^7$ and $\gamma = -3\,\mathrm{MPaK}^{-1}$ in 8×1 boxes.

In fig. 4.15, I plot the temperature drop due to the subadiabaticity in the geotherm as a function of the ratio of the spatially and temporally averaged magnitudes of horizontal to vertical advection for all of my calculations without internal heating. The models with two continents are also not included in this figure. To calculate the temperature drop, I record the maximum and the minimum temperatures along the temporally averaged geotherm in the upper and the lower mantle, respectively, and take the difference. One can clearly see the increasing trend in the subadiabaticity as the ratio increases which is consistent with my previous finding that horizontal advection can cause subadiabaticity. Fig. 4.16 shows how the same ratio varies with the number of convection cells in the lower mantle (C_{lm}). The overall negative slope of the scatter plot indicates that increased horizontal advection is associated with the models with longer wavelength convection cells. This indicates that all calculations with mixed surface boundary conditions and also free-slip calculations with large Clapeyron slopes, which have long-wavelength convection cells, will have stronger horizontal advection and hence, are more likely to have significantly subadiabatic geotherms.

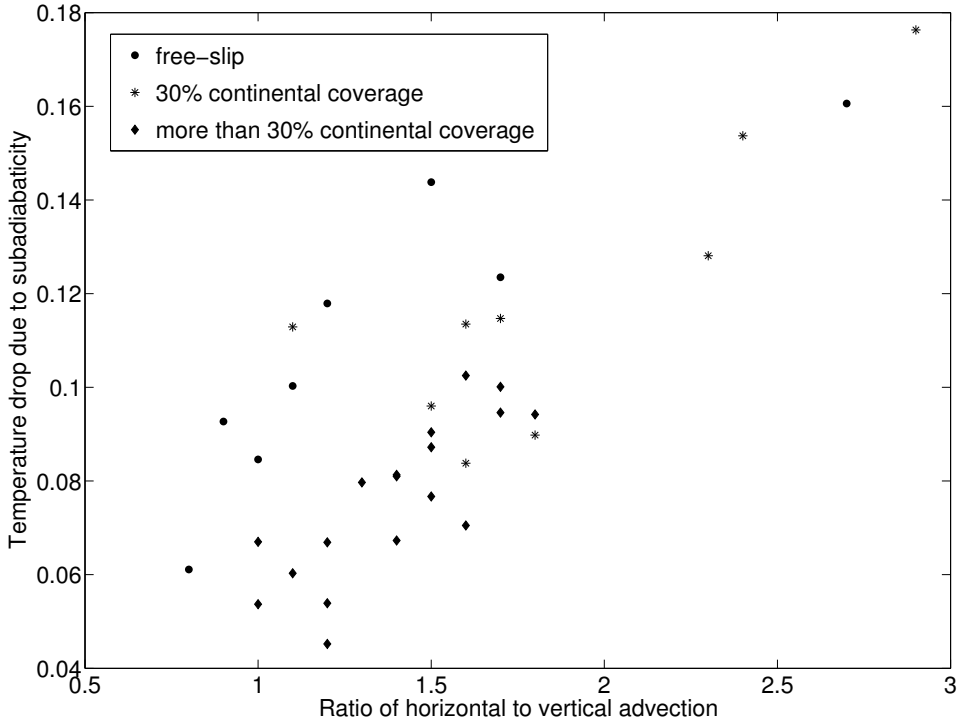

Figure 4.15: Total temperature drop across the mantle due to subadiabaticity in the geotherm as a function of the ratio of the temporally and spatially averaged horizontal to vertical advection. This plot does not include the models with internal heating and two continents.

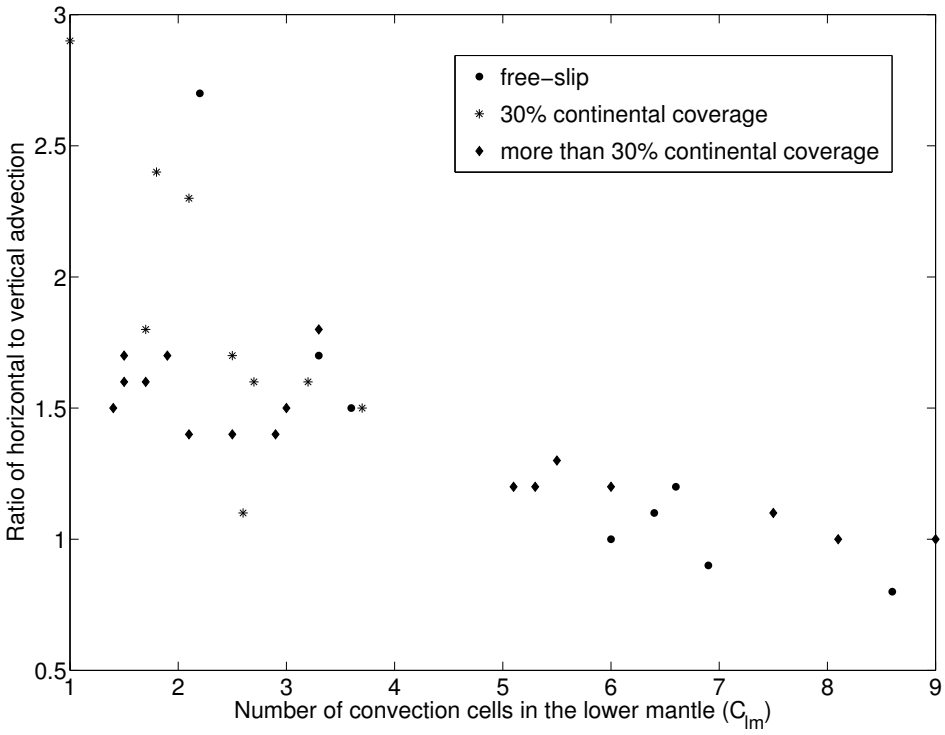

Figure 4.16: The ratio of the temporally and spatially averaged horizontal to vertical advection as a function of the number of convection cells in the lower mantle (C_{lm}). This plot does not include the models with internal heating and two continents.

4.5 Discussion and Conclusions

In this paper, the combined effects of different surface boundary conditions and the endothermic phase boundary were studied in detail. I measure the degree of layering in terms of its effect on the surface heat flux, mass flux, heat transport across 660 km-depth and the difference in the number of convection rolls in the upper and the lower mantle.

My investigation shows a sudden increase in the degree of layering between Clapeyron slopes of $-5\,\mathrm{MPaK}^{-1}$ and $-6\,\mathrm{MPaK}^{-1}$, as measured by the heat transport, mass flux and the surface heat flux in a unit aspect ratio box with $Ra = 10^6$ for all the different surface boundary conditions. However, a gradual increase in all of these measures of layering and a smaller maximum degree of layering is seen in wide aspect ratio boxes, which indicates a strong dependence of layering on the aspect ratio of the convection cell.

I have shown that the models with full continental coverage have the most strongly reduced advection of heat across 660 km-depth and the largest degree of decoupling between the upper and the lower mantle convection. This means that one-plate planets like Venus (Stevenson, 2003) might have stronger thermal layering and significantly decoupled mantle convection compared to Earth. Mixed surface boundary models, which are more Earth-like, show very little effect of change in Clapeyron slope on the surface heat flux. This occurs because in oceanic regions the mass flux is reduced to a lesser degree due to the dominance of the surface boundary condition and the efficiency of the boundary layer does not change significantly with mechanical layering while in continental regions the heat transport efficiency actually increases with layering. However, because of the gradual slope of the Nu-M_f relationship, the mass flux across 660 km-depth can be somewhat impeded and the flow in the upper and the lower mantle can also be weakly decoupled. This indicates that even if mantle convection was more layered in the past due to higher Rayleigh numbers, there may have been relatively little effect on the surface heat flux while mechanical mixing between the upper and the lower mantle may have been reduced. This might affect the mantle composition and could be of significant importance for geochemical studies of mantle mixing (Kellogg et. al., 2008; Peltier, 1996).

Although in the presence of a complete conducting lid the surface heat flux is somewhat affected by a decrease in the mass flux across 660 km-depth, no such effect is observed over the continental regions of the mixed boundary cases. The resistance to transport heat across the upper thermal boundary layer, as measured by Ra_δ, increases with increasing mass flux across 660 km-depth for cases where the surface is covered by rigid lid. This occurs because, in the presence of strong layering the convection planform in the upper mantle is governed by the surface boundary condition and the depth to the phase boundary and a shorter wavelength convective planform is chosen that is more favorable for efficient heat exchange at the surface.

The presence of a total lid results in significantly shorter wavelength mantle flows mostly in the upper mantle because of the drag on the horizontal flows along the surface. Layering usually increases with Ra as the flows have narrower features. However, with a rigid lid, even though the effective Ra is decreased compared with the free-slip cases, the wavelength is also decreased leading to stronger layering. The longest wavelength flows are seen in models with partial lids. Layering also increases the flow wavelength in the lower mantle as these flows are capable of penetrating the phase boundary. I have shown that increasing the width of the continent from 0 to 30% results in longer wavelength convection cells and that the largest rolls form when the width is 50%. This indicates that for approximately 30% continental coverage, we might expect long-wavelength convection in the Earth's mantle.

In my models, continents do not drift. However, in their study in 3D spherical geometry with mobile continents Phillips and Bunge (2005) found that partial continental coverage induces long-wavelength mantle flows. Zhong and Gurnis (1993) also used mobile continents in their cylindrical geometry calculations and demonstrated the presence of long-wavelength thermal structure. Numerical experiment by Lowman and Jarvis (1999) and laboratory tank experiment by Zhong and Zhang (2005) investigated the situations where continents were free to move and demonstrated periodic mantle flow behavior analogous to the Wilson cycle. All of these studies found upwellings beneath continents.

I find that introducing partial continental coverage produces a subadiabatic thermal gradient in the mantle, even without the presence of internal heating. This occurs because of the increased importance of horizontal advection in the resulting long-wavelength flows. This results in a larger temperature drop at the core-mantle boundary than would obtain for a purely adiabatic internal gradient causing an increased estimate of the heat flux from the core into the lower mantle for a given mean temperature (Bunge, 2005). This would affect energy budget calculations for the core and the mantle and would indicate that the inner core is slightly younger than is typically estimated (Costin and Butler, 2006). A subadiabatic geotherm would also require us to revise the estimates of the composition of the mantle (Mattern et al., 2005) and its transport properties (Monnereau and Yuen, 2002).

I have explored a wide range of parameter space and identified the combined effect of layering and continents on mantle convection. I carried out all of my calculations with an isoviscous fluid in two-dimensional Cartesian geometry. In future work, it will be interesting to investigate these effects in spherical geometry. Incorporating temperature and depth-dependent viscosity and more realistic surface plates might also be of interest and this has been discussed in chapter 6.

Chapter 5

Conclusions

The main focus of this thesis was to investigate some of the important aspects related to thermal convection in the Earth's mantle. This study further added to our understandings of our planet's interior. The specific objectives were i) a detailed analysis of the energy balance in areas with a positive vertical temperature gradient in the mantle and ii) the investigation of different convective planforms in the presence of both continental lithosphere and the endothermic phase boundary at 660 km-depth. A large number of numerical calculations were performed in two-dimensional Cartesian coordinates in order to achieve this goal.

In chapter 2, I have investigated the different energy balances that result in a subadiabatic thermal gradient within the mantle and I have defined them as VA-H, VA-HA and SC. This study showed that the balance between vertical advection and internal heating, VA-H, becomes increasingly important in leading to the subadiabatic temperature gradient as the internal heating rate is increased and it is mostly responsible for the bulk subadiabaticity within the geotherm. Previously this balance mechanism was thought to be the only factor leading to a positive temperature gradient in calculations with internal heating. However, I found that the balance between the horizontal and vertical advection, VA-HA, is important when the internal heating rate is less than roughly the surface heat flux value in the absence of internal heating for the same model (table 2.2) and it is responsible for the top and the bottom overshoot along the geotherm. In time-dependent calculations, the balance between the local secular cooling and all the other terms in the energy equation, SC, can also be responsible for the subadiabaticity and plays the role of either VA-H or VA-HA in a temporally averaged geotherm. High Rayleigh number mantle convection models that are representative of the Earth's mantle are always time-dependent and hence, SC is a significant contributor to the resulting positive slope in a time-averaged geotherm.

While studying the effects due to depth-dependent rheology, I found that an increased mobility near the surface because of the less viscous fluid resulted in greater horizontal advection that caused a significant increase in the importance of the VA-HA mechanism indicated by the narrow surface overshoot. This narrow zone of low viscosity and higher temperature may be equivalent to the observed seismic low-velocity zone (Dziewonski and Anderson, 1981) in tomographic studies. Calculations were also carried out using different surface boundary conditions representing continental

and oceanic lithosphere in the presence of internal heating. Due to the shorter wavelength convection cells and warmer mantle temperature, models with complete continental coverage showed an increased VA-H leading to a stronger bulk subadiabaticity and decreased VA-HA. This might imply that the single-continent planets like Venus (Stevenson, 2003) may have significantly subadiabatic interiors. I ran simulations in 2D domains with aspect ratios of 1, 4 and 8 and observed that, for energy balance calculations, square boxes produced slightly different results than wider boxes. However, results from both 4 and 8 aspect ratio boxes were essentially identical indicating that an aspect ratio of 4 is sufficient to analyze the balance mechanisms. The models that had Earth-like surface heat flux showed that the total dimensional mantle subadiabaticity may be as large as 450 K and all of the three balance mechanisms are possibly active in the mantle. In order to study the Earth's heat budget, mantle composition and also to parameterize CMB heat flux, the effects of subadiabatic temperature gradients are very important and must be considered.

In chapter 3, I studied the effects of temporally and spatially varying secular cooling and a constant internal heating amount within the mantle in unit aspect ratio numerical models. The results showed no obvious difference between these two effects.

Chapter 4 demonstrated the thermal effects of the endothermic phase boundary across 660 km depth on mantle convection in the presence of different surface boundary conditions. In order to quantify the degree of layering induced by the endothermic phase boundary, I defined and calculated different parameters. The thermal layering was defined as β, which gives the ratio of the conductive to the total heat flux across 660 km-depth. Average mass flux across that depth was used to measure the mechanical degree of layering. I calculated the number of convection rolls in the upper and lower mantle separately and this was used to observe the flow decoupling due to layering. The change in surface heat flux, defined as the Nusselt number (Nu), was also used to demonstrate the effects of different Clapeyron slopes of the phase boundary. All of the models that were run in unit aspect ratio boxes with $Ra = 10^6$ showed a sudden increase in the thermal and mechanical degree of layering as well as a decrease in the Nusselt number between the Clapeyron slopes of $-5\,\mathrm{MPaK}^{-1}$ and $-6\,\mathrm{MPaK}^{-1}$. When large aspect ratio boxes were used, the degree of thermal layering started gradually increasing for magnitudes of the Clapyron slope higher than $3\,\mathrm{MPaK}^{-1}$. This was also seen in the measure of mechanical layering, however, Nu for cases other than free-slip were not significantly affected by the change in Clapeyron slope. This indicates that the effects due to different Clapeyron slope values for the endothermic phase boundary are strongly dependent on the aspect ratio of the convection cell.

Mixed surface boundary models have Earth-like plate tectonics and they showed little to no response to the change in Clapeyron slope on the surface heat flux. The observations showed that the effects due to the surface boundary condition dominate the effects of different Clapeyron slopes for mixed surface boundary condition cases. Models that resembled single-continent planets like

Venus with complete continental coverage demonstrated the strongest thermal layering and the most significantly decoupled convection in the mantle for large magnitudes of the Clapeyron slope. In the presence of strong layering, the convection planform in the upper mantle is governed by the surface boundary condition and the depth to the phase boundary. The strong drag created by the no-slip surface mimicking continents penalizes horizontal mantle flow near the upper thermal boundary layer and due to this a large number of narrower features form in the upper mantle. These short wavelength convection cells were easily blocked by the phase boundary leading to stronger layering. Unlike the situations where the surface was free-slip, heat transport efficiency in the upper mantle surprisingly increased with the magnitudes of the Clapeyron slope in areas with continental lithosphere. The dominance of the mixed surface boundary condition effects combined with the increased heat transport efficiency under continents resulted in surface heat flux values being almost independent of the Clapeyron slopes. Convection wavelengths were large in the presence of partial continental coverage and as a result, the geotherms from these models showed subadiabaticity even without the presence of internal heating. The dominant energy balance in the regions of positive temperature gradient was between horizontal and vertical advection of heat (VA-HA).

Chapter 6

Future Considerations

The results presented in this thesis were obtained from 2D numerical calculations and were mostly isoviscous with the exception being the depth-dependence in viscosity in a few cases. The next immediate step would be to consider temperature-dependent (even stress-dependent) rheology and investigate the resulting behavior. It might also be interesting to observe the effects of periodic vertical boundaries instead of reflecting. Periodic boundary condition might add some extra freedom to the system, however, in small aspect ratio calculations it forces shorter wavelength flows compared to equivalent reflecting boundary condition models. A more physically realistic model of continents might also be useful. The perfect way to model continental lithosphere is still debatable. One of the better ways to incorporate the physical behavior of a continent would be placing a high viscosity (e.g. Lowman and Gable, 1999) and more buoyant slab on the surface and let it flow with the thermally driven convection in the mantle using the force balance method (e.g. Gable et al., 1991; Monnereau and Quéré, 2001). This added freedom would result in flow reversal (e.g. Lowman and Jarvis, 1993) phenomena and might increase the time-dependence of the model. The temperature-dependence of viscosity would produce more vigorous flow in the hotter upper mantle under the continents due to a higher effective Rayleigh number. A different numerical study (Yoshida and Kageyama, 2006) on single-plate planets like Venus or Mars has shown the presence of long-wavelength convection structures in 3D spherical geometry calculations with a very strong temperature and moderate to strong depth-dependent viscosity. Observing this effect for Earth-like plate tectonics would be useful. In reality, a significant concentration of radioactive materials can be found in continents. This implies that one might consider adding internal heating within the continental lithosphere in the model, which would affect the surface diagnostics and might have an interesting effect on the hot upwellings underneath the continents. Further complications can be added by carrying out the calculations in 3D Cartesian and spherical geometry, which require extensive computation time and power, in the future to investigate a more Earth-like set up.

In chapter 2, I have used a constant internal heating rate within the mantle. The use of an amount that is decreasing with time can also be taken into account. This might show a changing subadiabatic temperature drop across the mantle with time. I have defined the balance between the local secular cooling term and all the other terms in the energy equations as SC and showed this to

be a significant contributor when the calculation is time-dependent. As Earth-like mantle convection models always show strong time-dependence (Phillips and Bunge, 2005), it might be useful to investigate the effects due to SC more closely. Exploring the effects of compressibility, sphericity and the endothermic phase boundary on different energy balances resulting in subadiabaticity can also be considered as a focus of future studies. In a compressible model, viscous dissipation of heat can be significant in the deeper part of the mantle, which might cause a smaller CMB overshoot due to the increased temperature of mantle materials as they sink. In this thesis, I have calculated the dominant energy balances only for models without the 660 km-depth phase boundary. However, it will be useful to carry out similar calculations for layered models. The presence of strong layering produces long wavelength lower mantle convection cells and hence $VA - HA$ might be a significant factor to the lower mantle subadiabaticity.

One might consider incorporating the weaker exothermic phase boundary across 410 km-depth while investigating the various effects due to the stronger endothermic phase boundary across 660 km-depth in the Earth's mantle as presented in chapter 4. The presence of a low viscosity zone underneath the continental lithosphere can have some consequences in governing the convection wavelength in the case of mixed surface boundary calculations. A parameterized model combining the effects of continents and the endothermic phase boundary should be developed in order to further understand the observed effects and to be able to make predictions of the more complete numerical model.

Bibliography

[1] Adams, J. (1991), Recent enhancements in MUDPACK, a multigrid software package for solving partial differential equations, Appl. Math. Comput., 43, 79-93.

[2] Akaogi, M., Takayama, H., Kojitani, H., Kawaji, H. and Atake, T., (2007), Low-temperature heat capacities, entropies and enthalpies of Mg_2SiO_4 polymorphs, and $\alpha - \beta - \gamma$ and post-spinel phase relations at high pressure, Phys. Chem. Min., 34, 169-183.

[3] Ashby, M. F. and Verrall, R. A., (1978), Micromechanisms of flow and fracture and their relevance to the rheology of the upper mantle, Phil. Trans. R. Soc. Lond. A., 288, 59-95.

[4] Baumgardner, J. R., (1985), Three-dimensional treatment of the convective flow in the Earth's mantle, J. Statis. Phys., 39, 501-511.

[5] Baumgardner, J. R., (1988), Application of supercomputers to 3D mantle convection. In The Physics of Planets: Their Origin, Evolution and Structure, S. K. Runcorn. J. Wiley and Sons, Ltd., New York, 199-231,

[6] Bénard, H., (1900), Les tourbillons cellularies dans une nappe liquide, Revue Generale des Sciences Pures et Appliquees, 11, 1261-1271; 1309-1328.

[7] Bénard, H., (1901), Les tourbillons cellularies dans une nappe liquide tranportant de la chaleur par convection en régime permanent, Ann. Chim. Phys., 23, 62-144.

[8] Bercovici, D., Schubert, G. and Glatzmaier, G. A., (1989a), Three-dimensional spherical models of convection in the Earth's mantle, Science, 244, 950-955.

[9] Bercovici, D., Schubert, G. and Glatzmaier, G. A. and Zebib, A., (1989b), Three-dimensional thermal convection in a spherical shell, J. Fluid Mech., 206, 75-104.

[10] Bercovici, D., Schubert, G. and Glatzmaier, G. A., (1989c), Influence of heating mode on three-dimensional mantle convection, Geophys. Res. Lett., 16, 617-620.

[11] Bercovici, D., Schubert, G. and Glatzmaier, G. A., (1991), Modal growth and coupling in three-dimensional spherical convection, Geophys. Astrophys. Fluid Dyn., 61, 149-159.

[12] Bercovici, D., Schubert, G. and Glatzmaier, G. A., (1992), Three-dimensional convection of an infinite-Prandtl-number compressible fluid in a basally heated spherical shell, J. Fluid Mech., 239, 689-719.

[13] Billen, M. I. and Hirth, G, (2005), Newtonian versus non-Newtonian upper mantle viscosity: Implications for subduction initiation, Geophys. Res. Lett., 32, Article No. L19304.

[14] Blankenbach, B., Busse, F., Christensen, U., Cserepes, L., Gunkel, D., Hansen, U., Harder, H., Jarvis, G., Koch, M., Marquart, G., Moore, D., Olson, P., Schmeling, H., Schnaubelt, T. (1989), A benchmark comparison for mantle convection codes, Geophys. J. Int., 98, 23-38.

[15] Bobrov A. M. and Trubitsyn V. P., (1995), Rearrangement times of the mantle flow pattern beneath continents, Fizika Zemli, 7, 5-13.

[16] Boehler, R. (2000), High-pressure experiments and the phase diagram of mantle and core materials, Rev. Geophys., 38, 221-245.

[17] Boyd, F.R., Gurney, J.J., Richardson, S.H., (1985) Evidence for a 150-200 km thick Archean lithosphere from diamond inclusion thermobarometry, Nature, 315, 387-389.

[18] Brown, J. M., (1986), Interpretation of the D" zone at the base of the mantle: dependence on assumed values of thermal conductivity, Geophys. Res. Lett., 13, 1509-1512.

[19] Bunge, H. P., Richards, M. A., Baumgardner, J. R. (1996), Effect of depth-dependent viscosity on the planform of mantle convection, Nature, 379, 436-438.

[20] Bunge, H. P., Richards, M. A. and Baumgardner J. R., (1997), A sensitivity study of three-dimensional spherical mantle convection at 10^8 Rayleigh number: Effects of depth-dependent viscosity, heating mode, and an endothermic phase change, J. Geophys. Res., 102, 11991-12007.

[21] Bunge, H.P., Ricard Y., Matas J. (2001), Non-adiabaticity in mantle convection, Geophys. Res. Lett., 28, 879-882.

[22] Bunge, H.P. (2005), Low plume excess temperature and high core heat flux inferred from non-adiabatic geotherms in internally heated mantle circulation models, Phys. Earth Plan. Int., 153, 3-10.

[23] Butler, S. and Peltier, W. R., (1997), Internal thermal boundary layer stability in phase transition modulated convection, J. Geophys. Res., 102, 2731-2749.

[24] Butler, S.L. and Peltier, W.R. (2000), On scaling relations in time-dependent mantle convection and the heat transfer constraint on layering, J. Geophys. Res., 105, 3175-3208.

[25] Butler, S. L. and Peltier, W. R., (2002), Thermal evolution of Earth: Models with time-dependent layering of mantle convection which satisfy the Urey ratio constraint, J. Geophys. Res., 107, No. B6.

[26] Butler, S. L., Peltier, W. R. and Costin, S. O. (2005), Numerical models of Earth's thermal history: Effects of inner-core solidification and core potassium, Phys. Earth Plan. Int., 152, 22-42.

[27] Castle, J. C. and Creager, K. C., (1997), Seismic evidence against a mantle chemical discontinuity near $660km$ depth beneath Izu-Bonin, Geophys. Res. Lett., 24, 241-244.

[28] Chen, W.P. and Brudzinski, M.R., (2003), Seismic anisotropy in the mantle transition zone beneath Fiji-Tonga, Geophys. Res. Lett., 30, 1682, doi:10.1029/2002GL016330.

[29] Chandrasekhar, S., (1961), Hydrodynamic and hydromagnetic stability, Oxford University Press.

[30] Christensen, U., (1983), A numerical model of coupled subcontinental and oceanic convection, Tectonophysics, 95, 1-23.

[31] Christensen, U. R., (1984), Heat transport by variable viscosity convection and implications for the Earth's thermal evolution, Phys. Earth Plan. Int., 35, 264-282.

[32] Christensen, U. R. and Yuen, D. A., (1985), Layered convection induced by phase transitions, J. Geophys. Res., 90, 291-300.

[33] Christensen, U. R., (1989), The heat transport by convection rolls with free boundaries at high Rayleigh number, Geophys. Astrophys. Fluid. Dyn., 46, 93-103.

[34] Christensen, U. and Harder, H., (1991), 3-D convection with variable viscosity, Geophys. J. Int., 104, 213-226.

[35] Christensen, U., (1995), Effects of phase transitions on mantle convection, Annu. Rev. Earth Planet. Sci., 23, 65-87.

[36] Čížková, H., van Hunen, J. and van den Berg, A., (2007), Stress distribution within subducting slabs and their deformation in the transition zone, Phys. Earth Plan. Int., 161, 202-214.

[37] Costin, S.O. and Butler, S.L., (2006), Modelling the effects of internal heating in the core and lowermost mantle on the Earth's magnetic history, Phys. Earth Plan. Int., 157, 55-71.

[38] Cserepes, L., Rabinowicz, M. and Rosemberg-Borot, C., (1988), Three-dimensional infinite Prandtl number convection in one and two layers with implications for the Earth's gravity field, J. Geophys. Res., 93, 12009-12025.

[39] Cserepes, L. and Christensen, U. R., (1990), Three-dimensional convection under drifting plates, Geophys. Res. Lett., 17, 1497-1500.

[40] Cserepes, L., (1993), Effect of depth-dependent viscosity on the planform of mantle convection, Geophys. Res. Lett., 20, 2091-2094.

[41] Daly, R. A., The changing world of the Ice Age, (1934), Yale University Press.

[42] Davies, G. F., (1984), Lagging mantle convection, the geoid and mantle structure, Earth Plan. Sci. Lett., 69, 187-194.

[43] Davies, G. F., (1988), Role of the lithosphere in mantle convection, J. Geophys. Res., (93), 10451-10466.

[44] Davies, G. F., (2007), Mantle regulation of core cooling: A geodynamo without core radioactivity?, Phys. Earth Plan. Int., 160, 215-229.

[45] DeLandro-Clarke, W. and Jarvis, G.T., (1997), Numerical models of mantle convection with secular cooling, Geophys. J. Int, 129, 183193.

[46] Doin, M.-P., Fleitout, L and Christensen, U., (1997), Mantle convection and stability of depleted and un-depleted continental lithosphere, J. Geophys. Res., 101, 16119-16135.

[47] Dziewonski, A. M. and Anderson, D. L., (1981), Preliminary reference Earth model, Phys. Earth Plan. Int., 25, 297-356.

[48] Forte, A. M. and Peltier, W. R., (1987), Plate tectonics and aspherical Earth structure: the importance of poloidal-toroidal coupling, J. Geophys. Res., 92, 3645-3679.

[49] Forte, A. M. and Mitrovica, J. X., (2000), Deep-mantle high-viscosity flow and thermochemical structure inferred from seismic and geodynamic data, Nature, 410, 1049-1056.

[50] Fukao, Y., Obayashi, M., Inoue, H. and Nenbai, M., (1992), Subducting slabs stagnant in the mantle transition zone, J. Geophys. Res., 97, 4809-4822.

[51] Fukao, Y., Widiyantoro, S. and Obayashi, M., (2001), Stagnant slabs in the upper and lower mantle transition region, Rev. Geophys., 39, 291-323.

[52] Gable, C. W., Óconnell R. J. and Travis B. J., (1991), Convection in three dimensions with surface plates: Generation of toroidal flow, J. Geophys. Res., 96, 8391 8405.

[53] Gait, A. D. and Lowman, J. P., (2007a), Effect of lower mantle viscosity on the time-dependence of plate velocities in three-dimensional mantle convection models, Geophys. Res. Lett., 34, Article No. L21304.

[54] Gait, A. D. and Lowman, J. P., (2007b), Time-dependence in mantle convection models featuring dynamically evolving plates, Geophys. J. Int., 171, 467-477.

[55] Gait, A. D., Lowman, J. P. and Gable, C. W., (2008), Time dependence in 3-D mantle convection models featuring evolving plates: Effect of lower mantle viscosity, J. Geophys. Res., 113, Article No. B08409.

[56] Ghias, S. R. and Jarvis, G. T. (2007), Mantle flow reversals in cylindrical Earth models, Phys. Earth Plan. Int., 165, 194-207.

[57] Glatzmaier, G. A., (1988), Numerical simulations of mantle convection: Time-dependent, three-dimensional, compressible. spherical shell, Geophys. Astrophys. Fluid Dyn., 43, 223-264.

[58] Glatzmaier, G. A., Schubert, G. and Bercovici, D., (1990), Chaotic subduction-like downflows in a spherical model of convection in the Earth's mantle, Nature, 347, 274-277.

[59] Gordon, R. B., (1967), Thermally activated processes in the earth: creep and seismic attention, Geophys. J., 14, 33-43.

[60] Grigné, C. and Labrosse, S., (2001), Effects of continents on Earth cooling: thermal blanketing and depletion in radioactive elements, Geophys. Res. Lett., 28, 2707-2710.

[61] Grigné, C., Labrosse, S. and Tackley, P. J., (2005), Convective heat transfer as a function of wavelength: Implications for the cooling of the Earth, J. Geophys. Res., 110, B03409, doi:10.1029/2004JB003376.

[62] Grigné, C., Labrosse, S. and Tackley, P. J. (2007a), Convection under a lid of finite conductivity: Heat flux scaling and application to continents, J. Geophys. Res., 112, B08402, doi:10.1029/2005JB004192.

[63] Grigné, C., Labrosse, S. and Tackley, P. J., (2007b), Convection under a lid of finite conductivity in wide aspect ratio models: Effect of continents on the wavelength of mantle flow, J. Geophys. Res., 112, B08403, doi:10.1029/2006JB004297.

[64] Guillou, L. and Jaupart, C., (1995), On the effect of continents on mantle convection, J. Geophys. Res., 100, 24217-24238.

[65] Gurnis, M. and Davies, G. F., (1986), The effect of depth-dependent viscosity on convection mixing in the mantle and the possible survival of primitive mantle, Geophys. Res. Lett., 13, 541-544.

[66] Gurnis, M., (1988), Large-scale mantle convection and the aggregation and dispersal of supercontinents, Nature, 332, 695-699.

[67] Gurnis, M., C. Hall, and L. Lavier, (2004), Evolving force balance during incipient subduction, Geochemistry, Geophysics and Geosystems, 5 (7), doi:10.1029/2003GC000,681.

[68] Hager, B. H. and Clayton, R. W., (1989), Constraints on the structure of mantle convection using seismic observations, flow models and the geoid in Mantle Convection, edited by Peltier, W. R., Gordon and Breach, New York, 657-763.

[69] Hager, B. H. and Richards, M. A., (1989), Long-wavelength variations in Earth's geoid: physical models and dynamical implications, Phil. Trans. R. Soc. Lond. A., 328, 309-327.

[70] Hall, C. E., M. Gurnis, M. Sdrolias, L. Lavier, and R. D. Muller, (2003), Catastrophic initiation of subduction following forced convergence across fracture zones, Earth Plan. Sci. Lett., 212, 1530.

[71] Hart, S. R. and Zindler, A., (1986), In search of a bulk-Earth composition, Chem. Geol., 57, 247-267.

[72] Haskell, N. A., (1935), The motion of a viscous fluid under a surface load (I), Physics, 6, 265-269.

[73] Haskell, N. A., (1936), The motion of a viscous fhrid under a surface load (II), Physics, 7, 56-61.

[74] Hewitt, J. M., McKenzie, D. P. and Weiss, N. O., (1980), Dissipative heating in convective flows, J. Fluid Mech., 68, 721-738.

[75] Hirth, G., and D. Kohlstedt, (2003), Rheology of the upper mantle and the mantle wedge: a view from the experimentalists, in Inside the Subduction Factory, edited by J. Eiler, American Geophysical Union, Washington D.C.

[76] Holmes, A., (1931), Radioactivity and Earth movements, XVII., Trans. Geol. Soc. Glasgow, Vol. XVIII-Part III, 18, 559-606.

[77] Holmes, A., (1933), The thermal history of the Earth, J. Wash. Acad. Sci., 23, 169-195.

[78] Honda, S. and Yuen, D. A., (1994), Model for convective cooling of mantle with phase changes: Effects of aspect ratios and initial conditions, J. Phys. Earth, 42, 165-186.

[79] Honda, S., (1995), A simple parameterized model of Earth's thermal history with the transition from layered to whole mantle convection, Phys. Earth Plan. Int., 131, 357-369.

[80] Honda, S., (1996), Local Rayleigh and Nusselt numbers for Cartesian convection with temperature-dependent viscosity, Geophys. Res. Lett., 23, 2445-2448.

[81] Houseman, G., (1983), Large aspect ratio convection cells in the upper mantle, Geophys. J. Roy. Astron. Soc., 75, 309-334.

[82] Houseman, G., (1988), The dependence of convection planform on mode of heating, Nature, 332, 346-349.

[83] Ito, E. and Takahashi, E., (1989), Post-spinel transformations in the system $Mg_2SiO_4 - Fe_2SiO_4$ and some geophysical implications, J. Geophys. Res., 94, 10637-10646.

[84] Jarvis, G. T. and McKenzie, D. P., (1980), Convection in a compressible fluid with infinite Prandtl number, J. Fluid Mech., 96, 515-583.

[85] Jarvis, G.T. and Peltier, W. R., (1981), Effects of lithospheric rigidity on ocean-floor bathymetry and heat-flow, Geophys. Res. Lett., 8, 857-860.

[86] Jarvis, G.T. and Peltier, W. R., (1982), Mantle convection as a boundary layer phenomenon, Geophys. J. Roy. Astron. Soc., 68, 389-427.

[87] Jarvis, G. T., (1984), Time dependent convection in the Earth's mantle, Phys. Earth Plan. Int., 36, 305-327.

[88] Jaupart, C. and Parsons, B., (1985), Convective instabilities in a variable viscosity fluid cooled from above, Phys. Earth Plan. Int., 39, 14-32.

[89] Jeanloz, R., and Morris, S., (1987), Is the mantle geotherm subadiabatic?, Geophys. Res. Lett., 14, 335-338.

[90] Karato, S. L., (1989), Plasticity-crystal structure systematics in dense oxides and its implications for the creep strength of the Earth's deep interior: A preliminary result, Phys. Earth Plan. Int., 55, 234-240.

[91] Katagi, T., Yoshioka, S. and Hashimoto, M., (2008), Influence of temperature- and depth-dependent viscosity structures on postseismic deformation predictions for the large 1946 Nankai subduction zone earthquake, Tectonophysics, 454, 1-13.

[92] Kellogg, L.H., Natarajan, C.S. and Turcotte, D.L., 2008, Mantle mixing and the origin and persistence of geochemical reservoirs, Geochimica Et Cosmochimica Acta, 72, A461-A461.

[93] Kendall, J. M. and Shearer, P. M. (1994), Lateral variation in D" thickness from long-period shear wave data, J. Geophys. Res., 99, 11,575-11,590.

[94] Kennett, B.L.N and Gorbatov, A., (2004), Seismic heterogeneity in the mantle: Strong shear wave signature of slabs from joint tomography, Phys. Earth Plan. Int., 146, 87-100.

[95] King, S. D., Gable, C. W. and Weinstein, S. A., (1992), Models of convectiondriven tectonic plates: A comparison of methods and results, Geophys. J. Int., 109, 481 487.

[96] King, S. D. and Masters, G., (1992), An inversion for radial viscosity structure using seismic tomography, Geophys. Res. Lett., 19, 1551-1554.

[97] Kirby, S. H., (1983), Rheology of the lithosphere, Rev. Geophys. Space Phys., 21, 1458-1487.

[98] Kito, T., Thomas, C., Rietbrock, A., Garnero, E. J., Nippress S. E. J. and Heath, A. E., (2008), Seismic evidence for a sharp lithospheric base persisting to the lowermost mantle beneath the Caribbean, Geophys. J. Int., 174, 1019-1028.

[99] Krishnamurti, R., (1968a), Finite amplitude convection with changing mean temperature. Part 1. Theory, J. Fluid Mech., 33, 445-455.

[100] Krishnamurti, R., (1968b), Finite amplitude convection with changing mean temperature. Part 2. An experimental test of the theory, J. Fluid Mech., 33, 457-463.

[101] Lenardic. A. and Kaula, W. M., (1995), Mantle dynamics and the heat-flow into the Earth's continents, Nature, 378, 709-711.

[102] Lenardic. A. and Kaula, W. M., (1996), Near-surface thermal/chemical boundary layer convection at infinite Prandtl number: Two-dimensional numerical experiments, Geophys. J. Int., 126, 689-711.

[103] Lenardic, A., (1997), On the heat flow variation from Archean cratons to Proterozoic mobile belts, J. Geophys. Res., 102, 709-721.

[104] Lenardic, A., (1998), On the partitioning of mantle heat loss below oceans and continents over time and its relationship to the Archaean paradox, Geophys. J. Int., 134, 706-720.

[105] Lenardic, A. and Moresi, L., (2001), Heat flow scaling for mantle convection below a conducting lid: Resolving seemingly inconsistent modeling results regarding continental heat flow, Geophys. Res. Lett., 28, 1311-1314.

[106] Lenardic, A. and Moresi, L., (2003), Thermal convection below a conducting lid of variable extent: Heat flow scalings and two-dimensional, infinite Prandtl number numerical simulations, Phys. Fluids, 15, 455-466.

[107] Lenardic, A., Moresi, L. N., Jellinek, A. M. and Manga, M. (2005), Continental insulation, mantle cooling, and the surface area of oceans and continents, Earth Plan. Sci. Lett., 234, 317-333.

[108] Lowman, J. P. and Jarvis, G. T., (1993), Mantle convection flow reversals due to continental collisions, Geophys. Res. Lett., 20, 2087-2090.

[109] Lowman, J. P. and Jarvis, G. T., (1995), Mantle convection models of continental collision and breakup incorporating finite thickness plates, Phys. Earth Plan. Int., 88, 53-68.

[110] Lowman, J. P. and Jarvis, G. T., (1996), Continental collisions in wide aspect ratio and high Rayleigh number two-dimensional mantle convection models, J. Geophys. Res., 101, 25485-25497.

[111] Lowman, J. P. and Gable, C. W., (1999), Thermal evolution of the mantle following continental aggregation in 3D convection models, Geophys. Res. Lett., 26, 2649-2652.

[112] Lowman, J. P. and Jarvis, G. T., (1999), Effects of mantle heat source distribution on supercontinent stability, J. Geophys. Res., 104, 12733-12746.

[113] Lowman, J. P., King, S. D. and Gable, C. W., (2003), The role of the heating mode of the mantle in intermittent reorganization of the plate velocity field, Geophys. J. Int., 152, 455-467.

[114] Lowman, J. P., and King, S. D. and Gable, C. W., (2004), Steady plumes in viscously stratified, vigorously convecting, three-dimensional numerical mantle convection models with mobile plates, Geochemistry Geophysics Geosystems, 5, Article No. Q01L01.

[115] Lowman, J. P., Gait, A. D., Gable, C. W. and Kukreja, H., (2008), Plumes anchored by a high viscosity lower mantle in a 3D mantle convection model featuring dynamically evolving plates, Geophys. Res. Lett., 35, Article No. L19309.

[116] Lux, R. A., Davies, G. F. and Thomas, J. H., (1979), Moving lithosphere plates and mantle convection, Geophys. J. Roy. Astron. Soc., 58, 209-228.

[117] Kennett, B. L. N. and Gorbatov, A., (2004), Seismic heterogeneity in the mantle - strong shear wave signature of slabs from joint tomography, Phys. Earth Plan. Int., 146, 87-100.

[118] Lux, R. A., Davies, G. F. and Thomas, J. H., (1979), Moving lithospheric plates and mantle convection, Geophys. J. Roy. Astron. Soc., 58, 209-228.

[119] Machetel, P., Rabinowicz, M. and Bernardet, P., (1986), Three-dimensional convection in spherical shells, Geophys. Astrophys. Fluid Dyn., 37, 57-84.

[120] Machetel, P. and Weber, P., (1991), Intermittent layered convection in a model mantle with an endothermic phase change at 670 km, Nature, 350, 55-57.

[121] Mattern, E., Matas, J., Ricard, Y. and Bass, J. (2005), Lower mantle composition and temperature from mineral physics and thermodynamic modelling, Geophys. Journ. Int., 160, 973-990.

[122] Matyska, C., and Yuen, D.A. (2000), Profiles of the Bullen parameter from mantle convection modelling, Earth Plan. Sci. Lett., 178, 39-46.

[123] Matyska, C., and Yuen, D.A. (2001), Are mantle plumes adiabatic?, Earth Plan. Sci. Lett., 189, 165-176.

[124] Matyska, C., and Yuen, D.A. (2002), Bullen's parameter η: a link between seismology and geodynamical modelling, Earth Plan. Sci. Lett., 198, 471-483.

[125] McKenzie, D. P., Roberts, J. M. and Weiss, N. O., (1973), Numerical models of convection in the earth's mantle, Tectonophysics, 19, 89-103.

[126] McKenzie, D. P., Roberts, J. M. and Weiss, N. O. (1974), Convection in the Earth's mantle: Towards a numerical simulation, Jour. Fluid Mech., 62, 465-538.

[127] McKenzie, D. P. and Richter, F. M., (1981), Parameterized thermal convection in a layered region and the thermal history of the Earth, J. Geophys. Res., 86, 11667-11680.

[128] Mimouni, A. and Rabinowicz, M., (1988), The old continental shield stability related to mantle convection, Geophys. Res. Lett., 15, 68-71.

[129] Mitrovica, J. X. and Peltier, W. R., (1991a), Radial resolution in the inference of mantle viscosity from observations of glacial isosatic adjustment, Glacial Isostasy, Sea-Level and Mantle Rheology, 63-78.

[130] Mitrovica, J. X. and Peltier, A., (1991b), A complete formalism for the inversion of post-glacial rebound data - Resolving power analysis, Geophys. J. Int., 104, 267-288.

[131] Monnereau, M. and Quéré, S., (2001), Spherical shell models of mantle convection with tectonic plates, Earth Plan. Sci. Lett., 184, 575587.

[132] Monnereau, M. and Yuen, D. A. (2002), How flat is the lower-mantle temperature gradient?, Earth Plan. Sci. Lett., 202, 171-183.

[133] Moresi, L. N. and Lenardic, A., (1997), Three-dimensional numerical simulations of crustal deformation and subcontinental mantle convection, Earth Plan. Sci. Lett., 150, 233-243.

[134] Mussett, A. E. and Khan, M. A., (2000), Looking Into the Earth: An Introduction to Geological Geophysics, Cambridge University Press.

[135] Niu, F. and Kawakatsu, H., (1995), Direct evidence for the undulation of $660km$ discontinuity beneath Tonga: Comparison of Japan and California array data, Geophys. Res. Lett., 22, 531-534.

[136] O'Connell, R. J., (1971), Pleistocene glaciation and the viscosity of the lower mantle, Geophys. J. R. Astron. Soc., 23, 299-327.

[137] Ogawa, M., Schubert, G. and Zebib, A., (1991), Numerical simulations of three-dimensional thermal convection in a fluid with strongly temperature-dependent viscosity, J. Fluid Mech., 233, 299-328.

[138] Olson, P., (1987), A comparison of heat transfer laws for mantle convection at very high Rayleigh numbers, Phys. Earth Plan. Int., 48, 153-160.

[139] Parmentier, E.M., Sotin, C. and Travis, B. J., (1994), Turbulent 3-D thermal convection in an infinite Prandtl number, volumetrically heated fluid: implications for mantle dynamics, Geophys. J. Int., 116, 241-251.

[140] Peltier, W. R., (1996), Phase-transition modulated mixing in the mantle of the Earth , Phil. Trans. Roy. Soc. London Series A-Math. Phys. Engg. Sci., 354, 1425-1443.

[141] Peltier, W. R. and Solheim, L. P., (1992), Mantle phase-transitions and layered chaotic convection, Geophys. Res. Lett., 19, 321-324.

[142] Phillips, B. R. and Bunge, H. P., (2005), Heterogeneity and time dependence in 3D spherical mantle convection models with continental drift, Earth Plan. Sci. Lett., 233, 121-135.

[143] Poirier, J. P., (1993), Plastic rheology of crystals, in AGU Handbook of Physical Constants.

[144] Pollack, H., Hunter, S. J. and Johnson, J.R., (1993), Heat flow from the Earth's interior: Analysis of the global data set, Rev. Geophys., 31, 267-280.

[145] Prout, W., (1834), Bridgewater Treatises, volume 8, W. Pickering, London, Page 65.

[146] Rabinowicz, M., Lago, B. and Froidevaux, C., (1980), Thermal transfer between the continental asthenosphere and the oceanic subducting lithosphere: Its effect on subcontinental convection, J. Geophys. Res., 85, 1839-1853.

[147] Ranalli, G., (1991), The microphysical approach to mantle rheology in Glacial Isostacy, Sea-Level and Mantle Rheology, edited by Sabadini, R., Lambeck, K. and Boschi, E., Kluwer Academic Publications, London, 343-378.

[148] Reese, C. C., Solomatov, V. S. and Moresi, L. N. (1998), Heat transport efficiency for stagnant lid convection with dislocation viscosity: Application to Mars and Venus, J. Geophys. Res., 103, 13,643-13,657.

[149] Ricard, Y., Fleiotout, L. and Froidevaux, C., (1984), Geoid heights and lithospheric stresses for a dynamic Earth, Ann. Geophys., 2, 267-286.

[150] Ricard, Y., Vigny, C. and Froidevaux, C., (1989), Mantle heterogeneities, geoid and plate motion: A Monte Carlo inversion, J. Geophys. Res., 94, 13739-13754.

[151] Ricard, Y. and Wuming, B., (1991), Inferring the viscosity and 3D density structure of the mantle from geoid, topography and plate velocities, Geophys. J. Int., 105, 561-571.

[152] Richards, M. A. and Wicks, C. W., (1990), S-P conversion from the transition zone beneath Tonga and the nature of the $670km$ discontinuity, Geophys. J. Int., 101, 1-35.

[153] Ritsema, J., van Heijst, H.J. and Woodhouse, J.H., (2004), Global transition zone tomography, J. Geophys. Res., 109, B02302, doi:10.1029/2003JB002610.

[154] Rose C. and J. Temperton, (1994), The visual dictionary of the earth, Dorling Kindersley.

[155] Schubert, G., Yuen, D. A. and Turcotte, D. L., (1975), Role of Phase Transitions in a Dynamic Mantle, Geophys. J. R. Astr. Soc., 42, 705-735.

[156] Schubert, G. and Anderson, C. A., (1985), Finite element calculations of very high Rayleigh number thermal convection, Geophys. J. Roy. Astron. Soc., 80, 575-601.

[157] Schubert, G., Bercovici, D. and Glatzmaier, G. A., (1990), Mantle dynamics in Mars and Venus: Influence of an immobile lithosphere on three-dimensional mantle convection, J. Geophys. Res., 95, 14105-14129.

[158] Schubert, G., Anderson, C. and Goldman P., (1995), Mantle plume interaction with an endothermic phase change, J. Geophys. Res., 100, 8245-8256.

[159] Schubert, G., Turcotte, D. L. and Olson, P. (2001), Mantle Convection in the Earth and Planets, Cambridge University Press.

[160] Sleep, N.H. (2003), Simple features of mantle-wide convection and the interpretation of lower-mantle tomograms, C. R. Geosci., 335, 9-22.

[161] Sinha, G. and Butler, S.L., (2007), On the origin and significance of subadiabatic temperature gradients in the mantle, J. Geophys. Res., 112, B10406, doi:10.1029/2006JB004850.

[162] Sinha, G. and Butler, S.L., (2009), The combined effects of continents and the 660 km-depth endothermic phase boundary on the thermal regime in the mantle, article in press, Phys. Earth Plan. Int., doi:10.1016/j.pepi.2009.02.003.

[163] Solheim, L. P. and Peltier, W. R., (1993), Mantle phase-transitions and layered convection, Canad. J. Earth Sc., 30, 881-892.

[164] Solheim, L. P. and Peltier, W. R., (1994a), Avalanche effects in-phase transition modulated thermal convection: A model of Earth's mantle, J. Geophys. Res., 99, 6997-7018.

[165] Solheim, L. P. and Peltier, W. R., (1994b), phase boundary deflections at 660-km depth and episodically layered isochemical convection in the mantle , J. Geophys. Res., 99, 15861-15875.

[166] Solomatov, V. S. and Moresi, L. N. (1996), L. N., Stagnant lid convection on Venus, J. Geophys. Res., 101, 4755-4763.

[167] Sotin, C. and Labrosse, S. (1999), Three-dimensional thermal convection in an iso-viscous, infinite Prandtl number fluid heated from within and from below: applications to the transfer of heat through planetary mantles, Phys. Earth Plan. Int., 112, 171-190.

[168] Stevenson, D. J. (2003), Styles of mantle convection and their influence on planetary evolution, Comp. Rend. Geosc., 335, 99-111.

[169] Stocker, R. L. and Ashby, M. F., (1973), On the rheology of the upper mantle, Rev. Geophys. Space Phys., 11, 391-426.

[170] Tackley, P. J., Stevenson, D. J., Glatzmaier, G. A. and Schubert, G., (1993), Effects of an endothermic phase transition at 670 km depth in a spherical model of convection in the Earth's mantle, Nature, 361, 699-704.

[171] Tackley, P. J., (1995), On the penetration of an endothermic phase transition by upwellings and downwellings, J. Geophys. Res., 100, 15477-15488.

[172] Travis, B., Olson, P. and Schubert, G., (1990a), The transition from two-dimensional to three-dimensional planform in infinite-Prandtl number thermal convection, J. Fluid Mech., 216, 71-91.

[173] Travis, B., Weinstein, S. and Olson, P., (1990b), Three-dimensional convection planforms with internal heat generation, Geophys. Res. Lett., 17, 243-246.

[174] Trubitsyn, V. P. and Fradkov, A. S., (1985), Convection beneath the continents and oceans, Izvestiya Akademii Nauk Sssr Fizika Zemli, 7, 3-13.

[175] Trubitsyn, V. P., Bobrov, A. M. and Kubyshkin, V. V., (1991), Thermal-convection in the mantle due to horizontal and vertical temperature-gradients, Izvestiya Akademii Nauk Sssr Fizika Zemli, 5, 12-23.

[176] Trubitsyn V. P. and Rykov V. V., (1995), A 3-d numerical-model of the Wilson cycle, J. Geodyn., 20, 63-75.

[177] Trubitsyn, V. P., Shapiro, M. N. and Rykov, V. V., (1998), Numerical modeling of the pre-pliocene mantle flow in the junction zone of the Kurile-Kamchatka and Aleutian island arcs, Fizika Zemli, 4, 10-19.

[178] van der Hilst, R., Engdahl, R., Spakman, W. and Nolet, G., (1991), Tomographic imaging of subducted lithosphere below northwest Pacific island arcs, Nature, 353, 37-43.

[179] van der Hilst, R., (1995), Complex morphology of subducted lithosphere in the mantle beneath Tonga trench, Nature, 374, 154-157.

[180] van der Hilst, R.D., Widiyantoro, S. and Engdahl, E.R., (1997), Evidence for deep mantle circulation from global tomography, Nature, 386, 578-584.

[181] Vangelov, V. I. and Jarvis, G. T., (1994), Geometrical effects of curvature in axisymmetrical spherical models of mantle convection, J. Geophys. Res., 99, 9345-9358.

[182] Verhoogen, J., (1965), Phase changes and convection in the Earth's mantle, Phil. Trans. Roy. Soc., London, A258, 276-283.

[183] Vidale, J. E. and Benz, H. M., (1992), Upper mantle seismic discontinuities and the thermal structure of subduction zones, Nature, 356, 678-683.

[184] Walzer, U. and Hendel, R., (1997), Time-dependent thermal convection, mantle differentiation and continental-crust growth, Geophys. J. Int., 130, 303-325.

[185] Weertman, J., (1970), The creep strength of the Earth's mantle, Rev. Geophys. Space Phys., 8, 145-168.

[186] Weinstein, S. A., (1993), Catastrophic overturn of the Earth's mantle driven by multiple phase changes and internal heat generation, Geophys. Res. Lett., 20, 101-104.

[187] Yoshida, M. and Kageyama, A., (2006), Low-degree mantle convection with strongly temperature- and depth-dependent viscosity in a three-dimensional spherical shell, J. Geophys. Res., 111, Art. No. B03412.

[188] Yuen, D. A., Reuteler, D. M., Balachandar, S., Steinbach, V., Malevsky, A. V. and Smedsmo, J. J., (1994), Various influences on 3-dimensional mantle convection with phase-transitions, Phys. Earth Plan. Int., 86, 185-203.

[189] Zhao, D. P., (2004), Global tomographic images of mantle plumes and subducting slabs: insight into deep Earth dynamics, Phys. Earth Plan. Int., 146, 3-34.

[190] Zhao, W. L., Yuen, D. A. and Honda, S., (1992), Multiple phase-transitions and the style of mantle convection, Phys. Earth Plan. Int., 72, 185-210.

[191] Zhong, J. Q. and Zhang, J., 2005. Thermal convection with a freely moving top boundary, Phys. Fluid, 115105, DOI:10.1063/1.2131924.

[192] Zhong, S. J. and Gurnis, M., (1993), Dynamic feedback between a continent-like raft and thermal-convection, J. Geophys. Res., 98, 12219-12232.

[193] Zhong, S. (2006), Constraints on thermochemical convection of the mantle from plume heat flux, plume excess temperature, and upper mantle temperature, J. Geophys. Res., 111, Art. No. B04409.

Appendix A

Derivations of Poisson's Equations for mantle flow in 3D

Two dimensional mantle convection modeling only involves the poloidal motion, which includes mostly the upwellings and the downwellings within the mantle. However, in three dimensional geometry one needs to also consider the strike-slip motion, which is known as the toroidal motion. Mathematically, the poloidal and toroidal components of the velocity field can be written as

$$\mathbf{u}_p = \nabla \times \nabla \times (\Phi \hat{k}) \tag{A.1}$$

$$\mathbf{u}_t = \nabla \times (\Psi \hat{k}) \tag{A.2}$$

(Chandrasekhar, 1961) where Ψ and Φ are different potentials, and velocity

$$\mathbf{u} = \hat{i}u_x + \hat{j}u_y + \hat{k}u_z = \mathbf{u}_p + \mathbf{u}_t \tag{A.3}$$

where $\mathbf{u}_p$ and $\mathbf{u}_t$ are the poloidal and toroidal components of the motion.

If I take $\nabla\times$ of equation (2.14) and use (2.15), the x, y and z components, respectively, can be written as

$$0 = \frac{\partial T}{\partial y} + \nabla^2 \omega_x, \tag{A.4}$$

$$0 = -\frac{\partial T}{\partial x} + \nabla^2 \omega_y \tag{A.5}$$

and

$$0 = \nabla^2 \omega_z. \tag{A.6}$$

So

$$\nabla^2 \omega_x = -\frac{\partial T}{\partial y}, \tag{A.7}$$

$$\nabla^2 \omega_y = \frac{\partial T}{\partial x} \tag{A.8}$$

and

$$\nabla^2 \omega_z = 0. \tag{A.9}$$

Note that equation (A.9) implies $\omega_z = 0$, if $\omega_z = 0$ on all boundaries (free-slip models), which I will assume from now on.

The toroidal and the poloidal parts of the motion in terms of stream functions can also be written as

$$\mathbf{u}_t = \hat{i}\frac{\partial \Psi}{\partial y} - \hat{j}\frac{\partial \Psi}{\partial x} \tag{A.10}$$

and

$$\mathbf{u}_p = \hat{i}\frac{\partial^2 \Phi}{\partial x \partial z} + \hat{j}\frac{\partial^2 \Phi}{\partial y \partial z} + \hat{k}\left[-\left(\frac{\partial^2 \Phi}{\partial x^2} + \frac{\partial^2 \Phi}{\partial y^2}\right)\right]. \tag{A.11}$$

and the vorticity terms can also be written as

$$\omega_x = \hat{i} \cdot \nabla \times \mathbf{u} = \frac{\partial u_z}{\partial y} - \frac{\partial u_y}{\partial z}, \tag{A.12}$$

$$\omega_y = \hat{j} \cdot \nabla \times \mathbf{u} = \frac{\partial u_x}{\partial z} - \frac{\partial u_z}{\partial x} \tag{A.13}$$

and

$$\omega_z = \hat{k} \cdot \nabla \times \mathbf{u} = \frac{\partial u_y}{\partial x} - \frac{\partial u_x}{\partial y}. \tag{A.14}$$

As I already have shown that $\omega_z = 0$; using (A.10),(A.11) and (A.14), it can also be shown that Ψ=0, which implies $\mathbf{u}_t = 0$ if the boundary condition is free-slip without any lateral variation in viscosity. So, from here on all the velocity terms will only be related to the poloidal component.

Now if

$$\phi_x = \frac{\partial \Phi}{\partial y},\ \phi_y = \frac{\partial \Phi}{\partial x} \tag{A.15}$$

using (A.11) and (A.12), ω_x can be written as

$$\omega_x = -\nabla^2 \phi_x \tag{A.16}$$

and using (A.11) and (A.13), ω_y can be written as

$$\omega_y = \nabla^2 \phi_y. \tag{A.17}$$

Substituting (A.15) into (A.11),

$$\mathbf{u}_p = \hat{i}\frac{\partial \phi_y}{\partial z} + \hat{j}\frac{\partial \phi_x}{\partial z} + \hat{k}\left[-\left(\frac{\partial \phi_y}{\partial x} + \frac{\partial \phi_x}{\partial y}\right)\right]. \tag{A.18}$$

Now comparing (A.3) and (A.18)

$$u_x = \frac{\partial \phi_y}{\partial z},\ u_y = \frac{\partial \phi_x}{\partial z},\ u_z = -\left(\frac{\partial \phi_y}{\partial x} + \frac{\partial \phi_x}{\partial y}\right). \tag{A.19}$$

Finally, the governing four Poisson's Equations for isoviscous 3D mantle convection calculations are

$$\nabla^2 \phi_x = -\omega_x, \tag{A.20}$$

$$\nabla^2 \phi_y = \omega_y, \tag{A.21}$$

$$\nabla^2 \omega_x = -\frac{\partial T}{\partial y} \tag{A.22}$$

and

$$\nabla^2 \omega_y = \frac{\partial T}{\partial x}. \tag{A.23}$$

As an example I show a temperature snapshot from a 3D Cartesian coordinate model in fig. A.1. Here red indicates warmer temperatures. This model was run in a cube with $Ra = 10^6$ and the surface is fully free-slip.

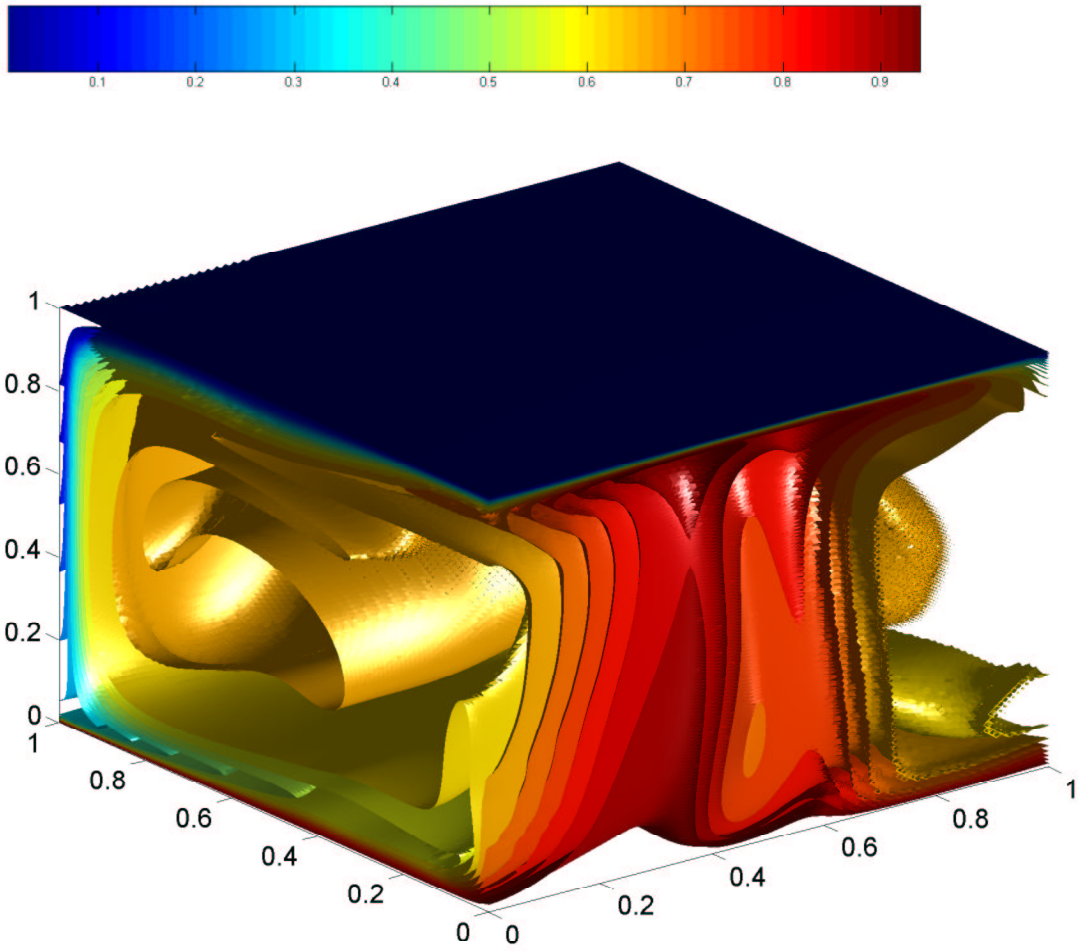

Figure A.1: Isosurface plot of the temperature from a calculation that was run in a $1 \times 1 \times 1$ box for $Ra = 10^6$ with a free-slip surface boundary condition. Colorbar is shown at the top.

Appendix B

Derivations of the Dynamic Topography in 2D for Isoviscous and Variable Viscosity Calculations

Dynamic topography can be defined as the topography generated by the dynamic forces in the upper part of the mantle. This section provides the required mathematical derivations to calculate dynamic topography numerically. In order to quantify this, I start with equation (2.22), which can also be written as

$$-\frac{\partial p}{\partial x} + \eta \nabla^2 u_x = 0. \tag{B.1}$$

Now non-dimensionalizing and substituting (2.13) into (B.1),

$$-\frac{\partial p}{\partial x} + \alpha \Delta T \nabla^2 u_x = 0. \tag{B.2}$$

Similarly the vertical normal stress term in its non-dimensional form can also be written as

$$\tau_{zz} = -p + 2\alpha \Delta T \frac{\partial u_z}{\partial z}. \tag{B.3}$$

Integrating (B.1) over the length of the box

$$p = \alpha \Delta T \left[\frac{\partial^2 \psi}{\partial x \partial z}(x) - \frac{\partial^2 \psi}{\partial x \partial z}(0) + \int_0^x \frac{\partial^3 \psi}{\partial z^3} dx + p_0 \right]. \tag{B.4}$$

Substituting (B.4) into (B.3)

$$\tau_{zz} = \alpha \Delta T \left[-\frac{\partial^2 \psi}{\partial x \partial z}(x) + \frac{\partial^2 \psi}{\partial x \partial z}(0) - \int_0^x \frac{\partial^3 \psi}{\partial z^3} dx - p_0 - 2\frac{\partial^2 \psi}{\partial x \partial z} \right]. \tag{B.5}$$

Using the expression for vorticity, I can write

$$\int_0^x \frac{\partial \omega}{\partial z} dx = \frac{\partial^2 \psi}{\partial x \partial z}(x) - \frac{\partial^2 \psi}{\partial x \partial z}(0) + \int_0^x \frac{\partial^3 \psi}{\partial z^3} dx. \tag{B.6}$$

Substituting this into (B.5) and assuming $p_0 = 0$

$$\tau_{zz} = -\alpha \Delta T \left(\int_0^x \frac{\partial \omega}{\partial z} dx + 2\frac{\partial^2 \psi}{\partial x \partial z} \right). \tag{B.7}$$

To express the non-dimensional vertical stress in a similar form for variable viscosity calculations, I consider the **x**-component of the momentum equation (2.22). Substituting the stress terms and non-dimensionalizing it I get,

$$\frac{\partial p}{\partial x} = \alpha \Delta T \left[2\frac{\partial \eta}{\partial x}\frac{\partial u_x}{\partial x} + \eta \frac{\partial \omega}{\partial z} + \frac{\partial \eta}{\partial z}\left(2\frac{\partial u_z}{\partial x} + \omega \right) \right]. \tag{B.8}$$

Here I use equation (2.26) to substitute for the tangential stress term.

Again integrating (B.8) along the length of the box, substituting the expression for pressure into (B.3) and assuming $p_0 = 0$,

$$\tau_{zz} = -\alpha\Delta T \left[2\int_0^x \frac{\partial\eta}{\partial x}\frac{\partial u_x}{\partial x}dx + \int_0^x \eta\frac{\partial\omega}{\partial z}dx + 2\int_0^x \frac{\partial\eta}{\partial z}\frac{\partial u_x}{\partial z}dx - \int_0^x \omega\frac{\partial\eta}{\partial z}dx \right] + 2\alpha\Delta T\frac{\partial u_z}{\partial z}. \quad \text{(B.9)}$$

So, the final form of the non-dimensional vertical stress equation in terms for ψ-ω is

$$\tau_{zz} = -\alpha\Delta T \left[2\int_0^x \frac{\partial\eta}{\partial x}\frac{\partial^2\psi}{\partial x\partial z}dx + \int_0^x \eta\frac{\partial\omega}{\partial z}dx + 2\int_0^x \frac{\partial\eta}{\partial z}\frac{\partial^2\psi}{\partial z^2}dx - \int_0^x \omega\frac{\partial\eta}{\partial z}dx + 2\frac{\partial^2\psi}{\partial x\partial z} \right]. \quad \text{(B.10)}$$

Note that the direct integration of B.10 often leads to large numerical errors and may be better carried out in the spectral domain (J. Lowman personal communication).

If the density of the mantle and the overlying water column are defined as ρ_m and ρ_w and the dimensional topography is denoted as H, I can write

$$\rho_w g H = \rho_m g H + \rho_m g d\tau_{zz}. \quad \text{(B.11)}$$

I multiply the non-dimensional vertical stress term with $\rho_m g d$ to convert it into the dimensional form. At the end the dimensional dynamic topography is expressed as

$$H = -\frac{\rho_m \tau_{zz} d}{(\rho_m - \rho_w)}. \quad \text{(B.12)}$$

The gravity anomaly created due to the dynamic topography can be calculated using the expression given by McKenzie et. al. (1973), which is

$$g_z = \left[\int_0^\lambda \epsilon_s(x)G(x_0, z_0, x, 1)dx + \int_0^\lambda \epsilon_{cmb}(x)G(x_0, z_0, x, 0)dx - \int_0^1 dz \int_0^\lambda T(x, z)G(x_0, z_0, x, z)dx \right] \quad \text{(B.13)}$$

where

$$G(x_0, z_0, x, z) = \frac{sinh\frac{\pi(z-z_0)}{\lambda}\left[cos\frac{\pi(z-z_0)}{\lambda} - cos\frac{\pi x}{\lambda}cos\frac{\pi x_0}{\lambda}\right]}{cosh^2\frac{\pi(z-z_0)}{\lambda} - 2cosh\frac{\pi(z-z_0)}{\lambda}cos\frac{\pi x}{\lambda}cos\frac{\pi x_0}{\lambda} + \frac{1}{2}\left(cos\frac{2\pi x}{\lambda} + cos\frac{2\pi x_0}{\lambda}\right)}. \quad \text{(B.14)}$$

The non-dimensional dynamic topography at the surface and at the CMB are ϵ_s and ϵ_{cmb} and λ is the normalized width of the box.

Appendix C

Parameterized Model For Different Continental Coverage and Thicknesses with a Phase-Change at 660 km-depth

In this case the whole system is divided into two: the lower and the upper mantle with an endothermic phase boundary between them. The governing equation for the heat-budget in the lower convecting mantle is

$$c_{p_l}\frac{\partial T_{m_l}}{\partial t} = Q_{cmb} - Q_{ph} + Q_{m_l} \tag{C.1}$$

where c_{p_l} and T_{m_l} are the total specific heat and the average temperature in the lower mantle, t is time, Q_{cmb} and Q_{ph} are the heat fluxes across the CMB and the phase boundary at 660 km-depth and Q_{m_l} is the internal heating rate per unit mass in the lower mantle.

As Q_{ph} includes both the conductive ($Q_{cond_{ph}}$) and advective ($Q_{adv_{ph}}$) heat fluxes across the phase boundary, I can write

$$Q_{ph} = Q_{adv_{ph}} + Q_{cond_{ph}} = Q_{cond_{ph}}/\beta \tag{C.2}$$

where,

$$\beta = \frac{Q_{cond_{ph}}}{Q_{adv_{ph}} + Q_{cond_{ph}}}. \tag{C.3}$$

Substituting

$$Q_{cmb} = \frac{k_{cmb}A_{cmb}(T_{cmb} - T_{m_l})}{\delta_{cmb}} \tag{C.4}$$

and

$$Q_{ph} = \frac{k_{ph}A_{ph}(T_{m_l} - T_{m_u})}{\beta\delta_{ph}} \tag{C.5}$$

into (C.1) I get

$$\frac{k_{cmb}A_{cmb}(T_{cmb} - T_{m_l})}{\delta_{cmb}} - \frac{k_{ph}A_{ph}(T_{m_l} - T_{m_u})}{\beta\delta_{ph}} + Q_{m_l} = c_{p_l}\frac{\partial T_{m_l}}{\partial t}. \tag{C.6}$$

Here k_{cmb} and k_{ph} are the thermal conductivities, δ_{cmb} and δ_{ph} are the boundary layer thicknesses and A_{cmb} and A_{ph} are the total areas along the CMB and the phase boundary, and T_{m_l} and T_{m_u} are the average temperatures in the lower and the upper mantle.

If the boundary layer Rayleigh numbers at the CMB and at the phase boundary are $Ra_{\delta_{cmb}}$ and $Ra_{\delta_{ph}}$, then

$$Ra_{\delta_{ph}} = \frac{g\alpha(T_{m_l} - T_{m_u})\delta_{ph}^3}{\nu\kappa} => \delta_{ph} = a_1(T_{m_l} - T_{m_u})^{-1/3} \tag{C.7}$$

and

$$Ra_{\delta_{cmb}} = \frac{g\alpha(T_{cmb} - T_{m_l})\delta_{cmb}^3}{\nu\kappa} => \delta_{cmb} = a_2(T_{cmb} - T_{m_l})^{-1/3}. \tag{C.8}$$

Here α is the thermal expansion coefficient, ν is the kinematic viscosity and κ is the thermal diffusivity, $a_1 = \left(\frac{Ra_{\delta_{cmb}}\nu\kappa}{g\alpha}\right)^{1/3}$ and $a_2 = \left(\frac{Ra_{\delta_{ph}}\nu\kappa}{g\alpha}\right)^{1/3}$.

I assume that $Ra_{\delta_{ph}} = \zeta Ra_{\delta_{cmb}}$, which gives

$$\delta_{ph}^3(T_{m_l} - T_{m_u}) = \zeta\delta_{cmb}^3(T_{cmb} - T_{m_l}) => \delta_{ph} = \phi\,\delta_{cmb}(T_{cmb} - T_{m_l})^{1/3}(T_{m_l} - T_{m_u})^{-1/3} \quad \text{(C.9)}$$

where $\phi = \zeta^{1/3}$. Substituting (C.9) into (C.6)

$$\phi\beta(T_{cmb} - T_{m_l})^{4/3} - (T_{m_l} - T_{m_u})^{4/3} + \varepsilon_1 Q_{m_l} = \varepsilon_1\, c_{p_l}\frac{\partial T_{m_l}}{\partial t} \quad \text{(C.10)}$$

where, $a_1 = \phi\, a_2 = a$, $k_{cmb} = k_{ph} = k_\delta$, $A_{cmb} = A_{ph} = 1$ and $\varepsilon_1 = \phi\beta\, a/k_\delta$.

Next I consider the upper mantle and derive a similar equation. The governing equation for the heat-budget in the upper convecting mantle is

$$c_{p_u}\frac{\partial T_{m_u}}{\partial t} = Q_{ph} - Q_l - Q_o + Q_{m_u} \quad \text{(C.11)}$$

where c_{p_u} is the specific heat and Q_{m_u} is the internal heating rate per unit mass within the upper mantle.

Again Substituting

$$Q_{ph} = \frac{k_{ph}A_{ph}(T_{m_l} - T_{m_u})}{\beta\delta_{ph}}, \quad \text{(C.12)}$$

$$Q_l = \frac{k_l A_l(T_{m_u} - T_l)}{\delta_l} \quad \text{(C.13)}$$

and

$$Q_o = \frac{k_o A_o(T_{m_u} - T_s)}{\delta_o} \quad \text{(C.14)}$$

into (C.11), I get

$$\frac{k_{ph}A_{ph}(T_{m_l} - T_{m_u})}{\beta\delta_{ph}} - \frac{k_l A_l(T_{m_u} - T_l)}{\delta_l} - \frac{k_o A_o(T_{m_u} - T_s)}{\delta_o} + Q_{m_u} = c_{p_u}\frac{\partial T_{m_u}}{\partial t}. \quad \text{(C.15)}$$

Here T_s is the surface temperature and in all cases $T_s = 0$, k_l and k_o are the thermal conductivities, δ_l and δ_o are the boundary layer thicknesses and A_l and A_o are the total areas at the base of the conducting lid and the lid-free region, and T_l is the average temperature along the top of the box under the continent.

If the boundary layer Rayleigh numbers at the base of the continent and in the lid-free region are Ra_{δ_l} and Ra_{δ_o}, then

$$Ra_{\delta_l} = \frac{g\alpha(T_{m_u} - T_l)\delta_l^3}{\nu\kappa} => \delta_l = a_3(T_{m_u} - T_l)^{-1/3} \quad \text{(C.16)}$$

and

$$Ra_{\delta_o} = \frac{g\alpha(T_{m_u} - T_s)\delta_o^3}{\nu\kappa} => \delta_o = a_4(T_{m_u} - T_s)^{-1/3} \quad \text{(C.17)}$$

where, $a_3 = \left(\frac{Ra_{\delta_l}\nu\kappa}{g\alpha}\right)^{1/3}$ and $a_4 = \left(\frac{Ra_{\delta_o}\nu\kappa}{g\alpha}\right)^{1/3}$.

I already know

$$Ra_{\delta_{ph}} = \frac{g\alpha(T_{m_l} - T_{m_u})\delta_{ph}^3}{\nu\kappa} => \delta_{ph} = a_2(T_{m_l} - T_{m_u})^{-1/3}. \quad \text{(C.18)}$$

Assuming $Ra_{\delta_l} = \Psi Ra_{\delta_o}$ and $Ra_{\delta_{ph}} = \zeta\, Ra_{\delta_o}$, (considering $Ra_{\delta_{cmb}} = Ra_{\delta_o}$) where ζ is a constant

$$\delta_l = \psi\,\delta_o(T_{m_u} - T_s)^{1/3}(T_{m_u} - T_l)^{-1/3} \quad \text{(C.19)}$$

and

$$\delta_{ph} = \phi\,\delta_o(T_{m_u} - T_s)^{1/3}(T_{m_l} - T_{m_u})^{-1/3} \tag{C.20}$$

where, $\psi = \Psi^{1/3}$. Substituting these two equations into (C.15)

$$\psi(T_{m_l} - T_{m_u})^{4/3} - \phi\beta L(T_{m_u} - T_l)^{4/3} - \psi\phi\beta(1-L)(T_{m_u} - T_s)^{4/3} + \varepsilon_2 Q_{m_u} = \varepsilon_2\, c_{p_u}\frac{\partial T_{m_u}}{\partial t} \tag{C.21}$$

where, L is the length of the continent, $k_{ph} = k_l = k_o = k_\delta$, $A_{ph} = 1$ (for unit aspect ratio box), $A_l = L$, $A_o = 1 - L$ (for unit aspect ratio box) and $\varepsilon_2 = a_4\phi\psi\beta/k_\delta$.

If the internal heating rate per unit mass within the continent is Q_c, the heat fluxes out of the continent (Q_s) and at the base of the continent (Q_l) are related as

$$Q_s = Q_l + Q_c \tag{C.22}$$

which gives,

$$k_c\frac{T_l - T_s}{d_c} = k_l\frac{T_{m_u} - T_l}{\delta_l} + Q_c \Rightarrow k_c\frac{T_l - T_s}{d_c} = \frac{k_l}{a_3}(T_{m_u} - T_l)^{4/3} + Q_c \tag{C.23}$$

where k_c is the thermal conductivity of the continent, $T_s(=0)$ is the temperature along the surface and d_c is the thickness of the continent.

Solving (C.23) for T_{m_u}, I get

$$T_{m_u} = T_l + \left[\frac{a_3\,k_c(T_l - T_s)}{k_l d_c} - \frac{a_3\,Q_c}{k_l}\right]^{3/4}. \tag{C.24}$$

Now substituting this in (C.21) and considering $\left[\frac{a\,k_c(T_l - T_s)}{k_l d_c} - \frac{a\,Q_c}{k_l}\right] = \Delta$ where $a_3 = a$

$$\psi(T_{m_l} - T_l\Delta^{3/4})^{4/3} - \phi\beta L\Delta - \beta\psi\phi(1-L)(T_l + \Delta^{3/4} - T_s)^{4/3} + \varepsilon_2 Q_{m_u} = \varepsilon_2\, c_{p_u}\frac{\partial T_{m_u}}{\partial t} \tag{C.25}$$

or in terms of T_{m_l} it can be written as

$$T_{m_l} = T_l\Delta^{3/4} + \left[\frac{\phi\beta L}{\psi}\Delta + \beta\phi(1-L)(T_l + \Delta^{3/4} - T_s)^{4/3} - \frac{\varepsilon_2}{\psi}Q_{m_u} + \frac{\varepsilon_2\, c_{p_u}}{\psi}\frac{\partial T_{m_u}}{\partial t}\right]^{3/4}. \tag{C.26}$$

Now substituting (C.24) and (C.26) in (C.10)

$$\begin{aligned}
&\varepsilon_1\, c_{p_l}\frac{\partial T_{m_l}}{\partial t} \\
&\quad= \phi\,\beta\left[T_{cmb} - T_l\Delta^{3/4} - \left(\frac{\phi\beta L}{\psi}\Delta + \beta\phi(1-L)\left(T_l + \Delta^{3/4} - T_s\right)^{4/3} - \frac{\varepsilon_2}{\psi}Q_{m_u} + \frac{\varepsilon_2\, c_{p_u}}{\psi}\frac{\partial T_{m_u}}{\partial t}\right)^{3/4}\right]^{4/3} \\
&\quad- \left[\frac{\phi\beta L}{\psi}\Delta + \beta\phi(1-L)\left(T_l + \Delta^{3/4} - T_s\right)^{4/3} - \frac{\varepsilon_2}{\psi}Q_{m_u} + \frac{\varepsilon_2\, c_{p_u}}{\psi}\frac{\partial T_{m_u}}{\partial t}\right] + \varepsilon_1 Q_{m_l}
\end{aligned} \tag{C.27}$$

In order to compare the parameterized model results with the numerical model results, it is assumed that the system is in equilibrium or $\frac{\partial T_{m_l}}{\partial t} = \frac{\partial T_{m_u}}{\partial t} = 0$. With this assumption, equation (C.27) can be solved for T_l. Consequently using the calculated value of T_l, equation (C.26) and (C.24) can be used to solve for T_{m_l} and T_{m_u}.

As examples I have plotted two different figures here showing results from both the numerical and the parameterized models. The numerical calculations were run in unit aspect ratio boxes.

Fig. C.1 shows the non-dimensional average temperature values from numerical calculations with full continental coverage for $Ra = 10^6$ and $Ra = 10^7$ as a function of different non-dimensional continental thicknesses together with the parameterized model results for comparison. In order to get the dimensional thickness they need to be multiplied by 2890 km, which is the depth of the whole mantle.

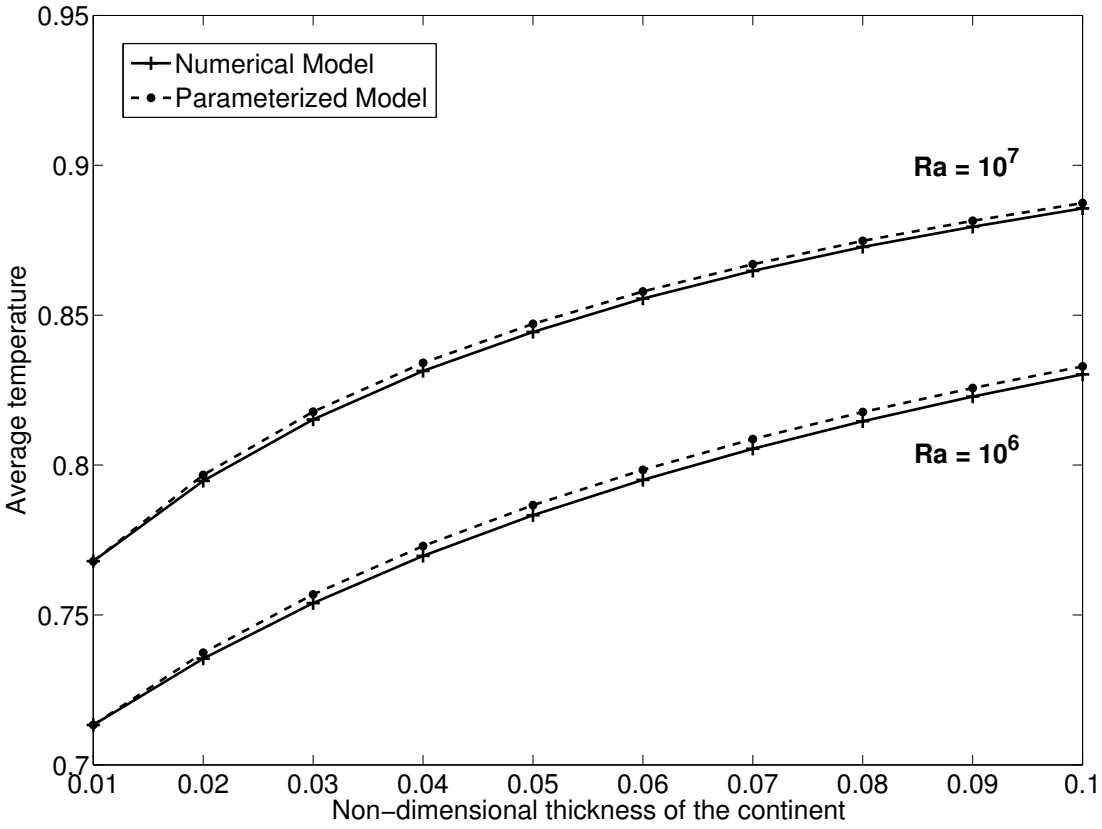

Figure C.1: Average temperature from numerical and parameterized models as a function of different continental lithospheric thicknesses for Rayleigh numbers of 10^6 and 10^7 with total continental coverage and no internal heating. Numerical models were run in 1×1 boxes.

Another set of calculations with different magnitudes of the Clapeyron slope in unit aspect ratio boxes for $Ra = 10^6$ with different surface boundary conditions (previously shown in fig. 4.5) is also demonstrated here in fig. C.2, where I plot the Nusselt number as a function of the Clapeyron slope from both numerical and parameterized models. Both of these plots show that the parameterized model works well in predicting results for numerical models that are run in 1×1 boxes.

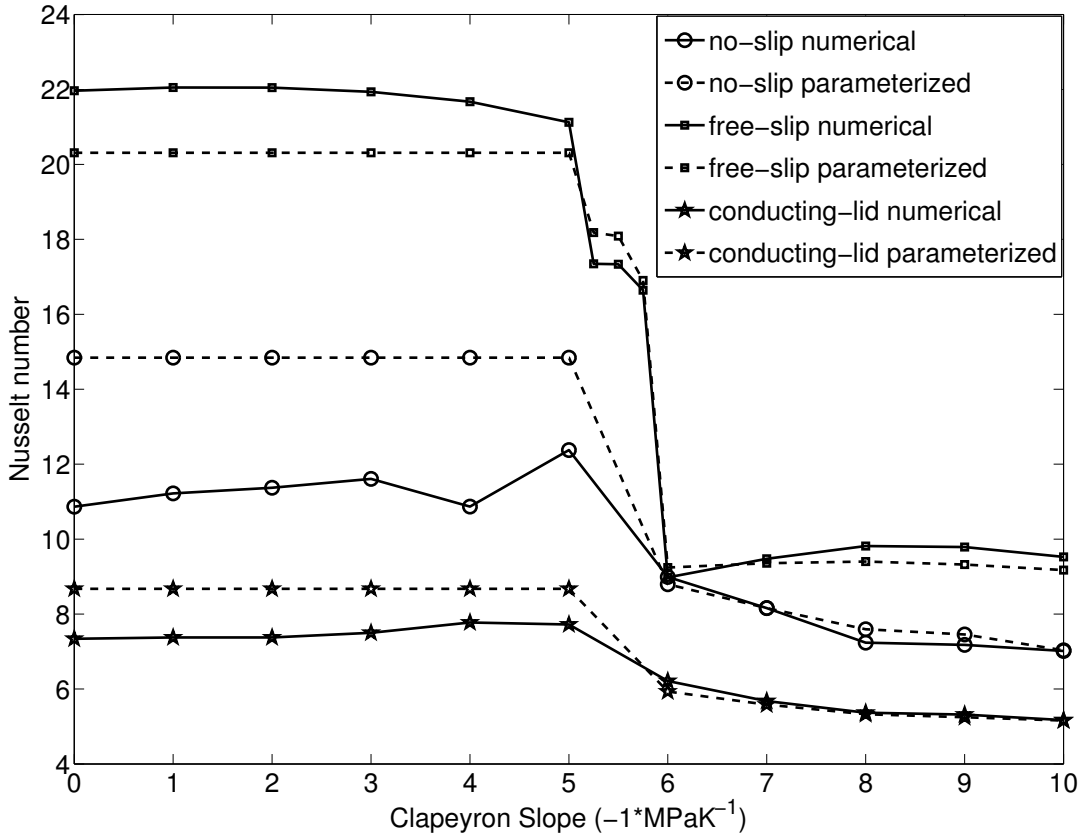

Figure C.2: Nusselt number from numerical and parameterized models as a function of different Clapeyron slopes with a Rayleigh number of 10^6 and no internal heating.

The three governing equations that can be used to create a thermal history of the Earth are

$$\varepsilon_1 \, c_{p_l} \frac{\partial T_{m_l}}{\partial t} = \phi\beta(T_{cmb} - T_{m_l})^{4/3} - (T_{m_l} - T_{m_u})^{4/3} + \varepsilon_1 Q_{m_l} \tag{C.28}$$

$$\varepsilon_2 \, c_{p_u} \frac{\partial T_{m_u}}{\partial t} = \psi(T_{m_l} - T_{m_u})^{4/3} - \phi\beta L(T_{m_u} - T_l)^{4/3} - \psi\phi\beta(1-L)(T_{m_u} - T_s)^{4/3} + \varepsilon_2 Q_{m_u} \tag{C.29}$$

$$c_{p_{core}} \frac{\partial T_{core}}{\partial t} = -Q_{core} + Q_{h_c} \tag{C.30}$$

where $c_{p_{core}}$, T_{core} and Q_{h_c} are the specific heat, temperature and internal heating rate per unit mass in the core, respectively, Q_{core} is the heat flux across the CMB and all the other variables have already been defined previously.